DFT Calculations of Silver Atomic Quantum Cluster on TiO_2 and CeO_2 Catalysts for Green Hydrogen Production

Moteb Alotaibi (Postgraduate Researcher)

This dissertation is submitted for the degree of Doctor of Philosophy

2023

Department of Physics, Lancaster University, UK

“WHERE THERE’S A WILL, THERE’S A WAY”

Declaration

This thesis has not been submitted in support of an application for another degree at this or any other university. It is the result of my own work and includes nothing that is the outcome of work done in collaboration except where specifically indicated. Many of the ideas in this thesis were the product of discussion with my supervisor Prof. Colin Lambert and my co-supervisor, Dr. Qingqing Wu.

Moteb Alotaibi

2023

Abstract

An important issue with photocatalysts in producing renewable energy such as hydrogen is the low efficiency in harvesting solar energy. Fortunately, the deposition of small metal clusters such as silver (Ag_5) could enhance the photocatalysts' absorption range to match visible light. In this thesis, I simulated different photocatalysts formed from Ag_5 atomic quantum clusters (AQCs) on anatase TiO_2 (101), rutile TiO_2 (110), and CeO_2 (111). Using the Vienna *ab initio* simulation package (VASP), I employed the generalised gradient approximation (GGA) and a hybrid functional combined with Hartree Fock (HF) theory to systematically study their geometric and electronic structures. The Hubbard term (U) is considered for all the calculations to account for the strongly interacted and localised *d* and *f* electrons.

The first focus of this thesis is to elucidate the photocatalytic activities of rutile and anatase TiO_2 surfaces. An in-depth investigation of stoichiometric and reduced rutile TiO_2 (110) and anatase TiO_2 (101) decorated with bipyramidal and trapezoidal Ag_5 atomic quantum clusters (AQCs) is carried out. It is found that the silver AQCs donate electrons to both stoichiometric and reduced TiO_2 surfaces resulting in the formation of a single polaron at either a five-fold coordinated (Ti_{5c}) atom or a six-fold coordinated (Ti_{6c}) atom, indicating improved surface activity. Furthermore, depositing Ag_5 AQCs on both TiO_2 surfaces can produce mid-gap states within the band gap of the bulk, thereby improving the optical response of the composite in the visible and infrared. As expected, the number of mid-gap energy states increases further when a single oxygen vacancy is introduced into

the studied surfaces, which reveals that Ag_5 AQCs and oxygen vacancies can reinforce each other, leading to higher efficiency photocatalytic activity. We also find that upon adsorption of Ag_5 AQCs on an anatase TiO_2 (101) surface, the energy required to form an oxygen vacancy is lower than that of rutile TiO_2 (110). Moreover, the adsorption of both bipyramidal and trapezoidal Ag_5 AQCs on both TiO_2 surfaces generally leads to significant distortion of the clusters, which accounts for the significant reduction in the total energy compared to the pristine TiO_2 and gas phase AQCs. This detailed investigation provides insight into new mechanisms for enhancing the photocatalytic efficiency of both rutile TiO_2 (110) and anatase TiO_2 (101) surfaces.

The second focus of this thesis is to examine the influence of trapezoidal and bipyramidal Ag_5 AQCs on the photocatalytic activity of stoichiometric and defective CeO_2 (111). In addition, the interaction of silicate (SiO_3^{2-}) with AQCs is considered, which is introduced experimentally when purifying the AQCs, and its effect on the electronic structures of ceria is investigated. It is demonstrated that there exist small gap states in the mid-gap after adsorbing these AQCs, which are attributed to charge transfer from these AQCs to the ceria. Furthermore, more gap states are observed when an oxygen vacancy is created, leading to improved photocatalytic activity. Importantly, the energy needed to form this oxygen vacancy is significantly lowered by the presence of AQCs. Finally, we noted that the silicate does not only contribute to purifying the AQCs, but also could play a crucial role in further increasing the photocatalytic activity.

Acknowledgements

I would like to express my deepest gratitude to **Prof. Colin J. Lambert**, who is always energetic and supportive. Colin, thanks for your endless help, guidance, and patience. This thesis would have never been completed without your generous and continued support, advice, and ideas. Thanks for being my supervisor and giving me this excellent opportunity to be one of your Ph.D. students. I would also like to express my grateful admiration to **Dr. Qingqing Wu**; none of this work would have been accomplished without her insightful comments, dedicated time, and suggestions.

To my kind father, **Alotaibi Qahess**, I greatly appreciate your endless support and advice. I am very proud to be your son. To my beloved mother, **Alotaibi Shaba**, you are everything to me. I am very grateful for your honest prayers that positively reflect my life. To my brothers and sisters, especially to my elder brother, **Khalid**, who passed away a couple of years ago. You always called me 'Doctor.' Special thanks to my lovely wife, **Alosaimi Rehab**, who stands beside me and has always encouraged me during my academic journey. To my sweet children, **Abdulrahman**, **Fazza**, and **Dorer,** you are the light of my life. To **Prof. Alosaimi Mshari**, The Vice-President of Educational and Academic Affairs at Prince Sattam bin Abdulaziz University, thank you very much for your advice and support during the early stages of my studies. Finally, to my best friend, **Alotaibi Abdulrahman**, you are not just a friend but my brother!

Above all, I thank God Almighty for giving me the strength, patience, ability, and blessing to complete this thesis work at Lancaster University successfully.

List of Publications

1- **M. Alotaibi**, Q. Wu, and C. Lambert, “Computational studies of Ag5 atomic quantum clusters deposited on anatase and rutile TiO2 surfaces,” *Appl. Surf. Sci.*, vol. 613, no. December 2022, p. 156054, 2023.

Contents

List of Tables

List of Figures

1 Introduction

1.1 Photocatalysis

Titanium dioxide (TiO_2, titania) has attracted considerable attention from scientists and engineers due to its high chemical and thermal stability, non-toxicity, and relatively low cost [1][2][3]. These facts make it usable in applications, such as solar cells [4], catalyst support [5], waste-water treatment [6], water splitting [7][8][9][10], biomedication [11], micro-organism inactivation (such as viruses and bacteria) [12], reduction of carbon dioxide [13] and batteries [14]. TiO_2 has various polymorphs that naturally crystallise and some that could be synthetically produced [15]. Rutile, anatase, and brookite (see Fig. 1-1) are the three most abundant natural polymorphs. Out of those phases, only rutile and anatase are the used for photochemical applications [16][17]. However, the

following drawbacks hinder the utilisation of TiO_2 in photocatalytic applications, [17]: (i) the band gap energy (E_g) of TiO_2 is approximately 3.2 eV, which only allows it to absorb ultraviolet light (UV) (~4% of the solar radiation energy) and severely limits its ability to use visible light (~50% of the solar radiation energy) for hydrogen generation; (ii) TiO_2 has a high rate of charge recombination of photogenerated electrons in the conduction band (CB) with photogenerated holes in the valance band (VB).

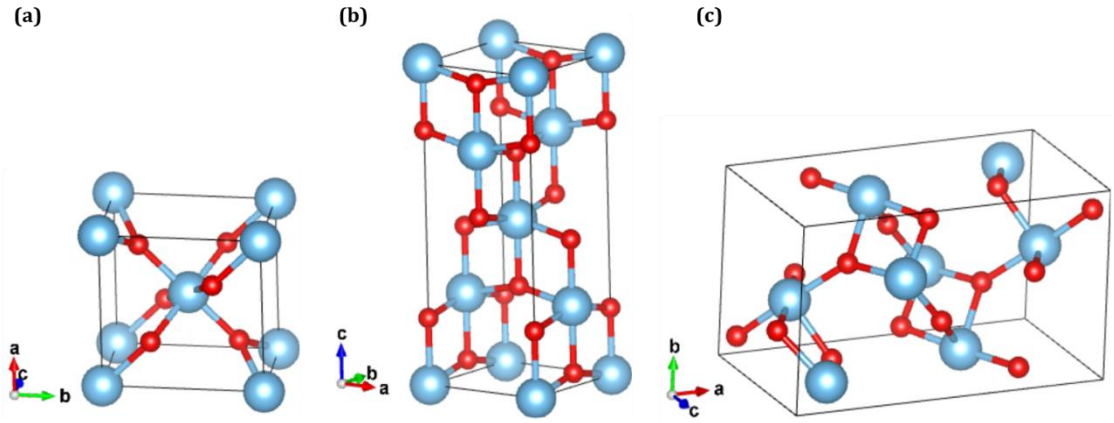

Fig. 1-1 Three different phases of titania. (a) rutile, (b) anatase and (c) brookite. The blue spheres denote Ti atoms, and the red spheres denote O atoms.

To overcome the disadvantages mentioned above and improve the photocatalytic activities by extending the visible light response of TiO_2 for solar photocatalysis of hydrogen generation, numerous techniques have been implemented, such as combining other semiconductor materials with TiO_2 [18][19], dye sensitisation

[20], doping with metal [21] and non-metallic ions [22], and the deposition of noble metals [23]. Noble metals have Fermi energy levels lower than titania; thus, they are frequently utilised as cocatalysts. Furthermore, it has been proved that adsorbing micro- and nanoparticles noble metals, such as palladium (Pd), platinum (Pt), gold (Au), and silver (Ag) on TiO_2 surfaces can considerably enhance photocatalytic activities [24][25][26][27][28][29][30][31].

Rutile TiO_2 has been the focus of most surface science studies as it is the most abundant and readily available phase. Faces have a crucial role in determining nanomaterials properties and are also important for understanding the reactivity of materials. It has been reported by DFT and ab initio calculations that among periodic TiO_2 slabs of the (001), (100), (110), and (011) face, the (110) surface of rutile possesses the lowest surface energy, indicating that it is the most stable surface [32][33]. Therefore, rutile TiO_2 (110) is one of the slab models investigated in this thesis. In addition anatase is very frequent and stable in nanoparticles [34][35],yields high photocatalytic activity and thus is used in photocatalytic and photovoltaic cells [36]. There have been intensive theoretical studies on the reactivity and structure of anatase faces, concentrating on the faces (001), (100), and (101). These are the crystal surfaces that are most commonly exposed in anatase nanomaterials. It was found that among these faces, the (101) is the most stable face that dominates the material surface [37]. For this reason, the TiO_2 (101) anatase surface is chosen and modelled in this thesis.

Cerium dioxide (ceria) has been extensively studied due to its several applications related to its unique catalytic properties. It can be used for chemical-mechanical surface polishing, such as eye-glass lenses, electronic displays, and other optical applications [38][39]. In addition, most of the research focus on ceria in many catalytic applications such as oxygen storage in three-way catalysts [40][41][42], low temperature water gas shift (WGS) reaction [43][44], CO oxidation [45][46], and generation of hydrogen [47][48] due to its ability for the redox cycle between Ce^{4+} and Ce^{3+} states [49][50][51]. More recently, ceria has been promising for the electrocatalytic water splitting reaction (WSR) in solid oxide electrolysis cells (SOECs) owing to the fast mobility of oxygen ions and the highly enhanced efficiency for sustainable hydrogen generation [51].

In many of the above applications, different morphologies of ceria have been utilised, because the attributes are morphology-dependent. As a single crystal, ceria has three primary morphologies, e.g., rod, cube, and octahedron. Each morphology has certain surfaces, which are represented as follows: rod morphology with (100) and (110) faces, cube morphology with (100) faces, and truncated octahedra morphology with (100) and (111) faces. The differences in the exposed faces result in different functions in corresponding applications, due to the different physio-chemical attributes of each face. The stability of ceria has been examined by ab initio and DFT studies, and it was found that the (111) surface is the most thermodynamically stable among other surfaces, i.e., (100) and (110) [52][53]. Ceria, in its bulk state, has a large band gap (O (2*p*)- Ce (5*d*)

orbitals) that is roughly 6 eV [54]. Yet, the existance of empty 4*f* states related to Ce^{4+} leads to a narrower band gap of approximately 3.2 eV [55][56]. A single unit cell of CeO_2 is illustrated in Fig. 1-2. The CeO_2 (111) surface is chosen and studied in this thesis.

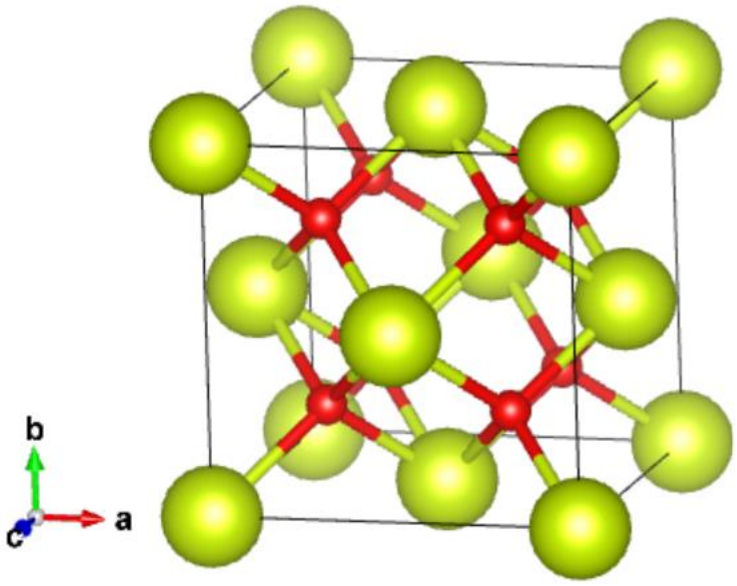

Fig. 1-2 Unit cell of ceria. The green spheres denote Ce atoms, and the red spheres denote O atoms.

The conversion of water (H_2O) into hydrogen and oxygen using sunlight addresses the earth's climate-change challenges: production of renewable hydrogen energy and reduction of the atmospheric carbon dioxide (CO_2) levels. The CO_2 levels in the atmosphere have significantly increased, mainly due to energy consumption (over

80% of energy usage), which is mainly generated by fossil fuels [57]. Consequently, producing sustainable fuels by harvesting abundant solar energy reduces the dependence on fossil fuels and contributes to decarbonising the transport sector. Furthermore, hydrogen produced by water splitting with sunlight is a promising candidate for an environmentally friendly energy carrier owing to (i) its cost, which is expected to be less expensive compared to the current cost of conventional energy, (ii) its use of a raw material (i.e., water), which is a safe resource, and (iii) the ready access across the globe to sunlight.

There are three main steps involved in the photocatalytic process of water splitting, namely: (i) the absorption of an incident photon energy, which must be equal to or greater than the oxide band gap to generate an electron (in the conduction band) and hole (in the valence band), (ii) separation of the photogenerated charges, and (iii) the reduction/oxidation (redox) reaction of water, which ultimately leads to water splitting. Various oxides have been used in the photocatalytic reduction of H_2O [58]; however, one challenge is the absorption of the photon energy in the visible light spectrum due to the oxide's large band gap. Another challenge is the rapid recombination rate of the photogenerated charges. Therefore, the deposition of Ag_5 AQCs on the oxide surface is one approach, which promotes the absorption of sunlight photons and lowers the recombination rate of the photogenerated electrons and holes.

Silver AQCs consisting of five atoms (~0.5 nm in size) are promising candidates for novel catalysts due to their unique and size-specific properties, which do not appear on the corresponding nanoparticles and bulk Ag [59]. For instance, Ag_5 AQCs exhibit new chemical, electrical and optical attributes, which differ drastically from the nanoparticles and bulk materials. Furthermore, Ag_5 AQCs possess discrete electronic energy levels and show ''molecule-like'' optical characteristics, producing a bridge between the single atoms and the large metal nanoparticles [60]. Therefore, doping semiconductor materials with these Ag_5 AQCs as co-catalysts can enhance their optical response in the visible light spectrum. These desirable properties have driven this Ph.D. thesis to conduct investigations on the Ag_5 AQCs-based photocatalysts towards renewable hydrogen energy production.

1.2 **Thesis Outline**

The main title of this thesis is the study of critical metal oxide catalysts utilised in various clean energy applications. By investigating the electronic structures of the catalysis surfaces, we can better understand the processes that can take place, which in turn can lead to the development of efficient catalytic processes.

This thesis consists of six chapters.

The present chapter summarised the choice of DFT for the study of electronic structure calculations. This was followed by a brief introduction to titania and ceria catalysts and their different types and applications. Chapter 2 provides an insight into the history of theories that underpin the computational calculations used in this thesis especially the development of DFT.

Chapter 3 details the theoretical considerations of the methodology used in work presented here. An overview of the use of VASP software using a plane wave basis set is provided. Finally, the geometries optimisation procedure is briefly described, and some calculated quantities are explained to understand better the work presented in the following chapters.

Chapter 4 focuses on the effect of the deposition of small trapezoidal and bipyramidal silver AQCs on the photocatalytic activity of perfect and defective anatase (101) and rutile (110) TiO_2 surfaces. It is found that these silver AQCs are oxidised, donating their electrons to the substrates resulting in the formation of a surface polaron within the band gap of the bulk. In addition, further gap states are observed by introducing a single-point defect, i.e., an oxygen vacancy. These gap states are critical in improving the photocatalytic activity of the metal oxides. In Chapter 4, it is also shown that upon adsorption of these tiny silver AQCs on anatase (101) TiO_2, the amount of energy required to form an oxygen vacancy is lower compared to the rutile (110) TiO_2 surface.

Chapter 5 presents the deposition effect of trapezoidal and bipyramidal Ag_5 AQCs on electronic structures of a perfect and reduced CeO_2 (111) surface and the adsorption effect of Ag_2SiO_3 on electronic structures of $Ag_5@CeO_2$ (111) systems. Both Ag_5 AQCs are found to donate their unpaired charges to the support, forming polaronic states within the band gap of the semiconductor. Interestingly, a dramatic reduction in the formation energy of an oxygen vacancy is observed upon the deposition of these AQCs compared to the pristine substrate. Furthermore, the deposit of Ag_2SiO_3 increases the number of gap states, forms more polarons on the surface of the support, decreases the oxygen vacancy formation energy further, and improves the overall photocatalytic efficiency of both the perfect and defective CeO_2 (111) surface.

2 Theoretical Background

This chapter provides insight into the fundamental theory underlying all modelling techniques utilised in this thesis. Density functional theory (DFT) has been an indispensable theoretical tool for studying electronic structures in solid-state physics. The activity of chemical reactions on a catalyst could be predicted by the electronic structures of the catalyst acquired by implementing DFT. Therefore, DFT has recently been applied in catalysis-related investigations to provide insight into the mechanism of chemical reactions on catalysts [61][62][63][64]. The DFT technique is implemented in all calculations in this thesis to understand the chemical reactions of silver atomic quantum clusters (AQCs) and purification processes using a silicate on multiple hydrogen-producing metal oxide catalysts i.e., titanium dioxide (TiO_2) and cerium dioxide (CeO_2).

2.1 Bra-Ket Notation

In this chapter, the bra-ket notation is utilised to express the quantum states using the following forms,

$$< f| = f^*(x) \ \text{('bra')} \tag{2.1}$$

$$|f >= f(x) \ \text{('ket')} \tag{2.2}$$

where $f^*(x)$ is the complex conjugate ('bra') of $f(x)$ ('ket'). The combination of ('bra') and ('ket') expresses the superposition of states; for instance,

$$\langle \Psi|\Psi\rangle \ = \ \int \Psi^*(x)\Psi(x)\, dx \tag{2.3}$$

2.2 The Schrödinger Equation

The time-independent Schrödinger equation must be solved in order to obtain information on the wave function of a given system. The Hamiltonian operator, $\widehat{H}$, determines the system, which corresponds to the total energy of the system and is given in the following equation,

$$\widehat{H}\Psi = E\Psi = (\hat{T} + \hat{V})\Psi \tag{2.4}$$

where Ψ and E are the wave function and energy of the system, respectively and $\hat{T}$ and $\hat{V}$ are the kinetic and potential energies of the system, respectively.

The Schrödinger equation can be solved to calculate the electronic structure of a simple system consisting of a single electron, i.e., a hydrogen atom [65]. However, for many body systems, such as a condensed matter or a large organic molecule, it becomes impossible to analytically solve the Schrödinger equation due to the rapidly increasing complexity of electron-electron interactions and the increase in computational cost. Thus, it is essential to use approximations to solve the Schrödinger equation to determine the system's electronic wave function. The Hartree-Fock and DFT techniques are two examples that can be used to approximate the solution to the Schrödinger equation. The Hartree-Fock and DFT methods will be presented and discussed in detail in the following sections.

2.3 **The Hamiltonian**

In 1 dimension, the Hamiltonian operator of a system is given as,

$$\hat{H} = \hat{T} + \hat{V} = -\frac{\hbar^2}{2m}\left(\frac{\partial^2}{\partial x^2}\right) + V(x) \qquad 2.5$$

where $\hbar$ is Planck's constant over 2π and m is the mass of an electron. In a 3-dimensional system, the formula can be written as,

$$\hat{H} = -\frac{\hbar^2}{2m}\nabla_r^2 + V(r) \qquad 2.6$$

where the Laplacian operator is given as,

$$\nabla_r^2 = \frac{\partial^2}{\partial x^2} + \frac{\partial^2}{\partial y^2} + \frac{\partial^2}{\partial z^2} \tag{2.7}$$

and the potential energy of a charged system is given as,

$$V\,(r) = \sum_{i>j} \frac{Z_i Z_j e^2}{4\pi\,\epsilon_0}\left(\frac{1}{|r_i - r_j|}\right) \tag{2.8}$$

where i denotes the operator only acts on ith electron, ϵ_0 is the permittivity of free space, and e is the elementary charge.

The Hamiltonian of a many-body system that contains nuclei and electrons can be written as,

$$\widehat{H} = \sum_A \frac{1}{2m_A}\nabla_A^2 + \sum_A \frac{1}{2}\nabla_i^2 + \sum_{A>B} \frac{Z_A Z_B}{|r_A - r_B|} - \sum_{A>B} \frac{Z_A}{|r_A - r_i|} + \sum_{i>j} \frac{1}{|r_i - r_j|} \tag{2.9}$$

where m_A is the nucleus mass, Z_A and Z_B are the charges on the nucleus A and B, r_A and r_i are the distances from nucleus A and electron i

2.4 The Born-Oppenheimer Approximation

Born and Oppenheimer [66] in 1927 assumed that the electron mass is insignificant compared to the nucleus mass; therefore, the kinetic energy $\left(\frac{\hbar^2}{2m}\ \nabla_r^2\right)$ of the electron is significantly greater than that of the nucleus. Thus, the basic premise of the Born-Oppenheimer approximation is that in the Hamiltonian of Equation 2.9, the nuclei kinetic energy can be considered a negligible parameter. This allows the motion of the electrons and nuclei in a system to be separated due to the massive mass difference. The Born-Oppenheimer approximation states that the system's wave function can be broken down into nuclear and electronic parts. The nuclear contributions involve in the equation only as constant terms, and the Hamiltonian of Equation 2.9 is solved with zero nuclear kinetic energy. Thus, Equation 2.9 leads to the Schrödinger equation for the many-body system and is given as

$$\left\{-\frac{\hbar^2}{2m_i}\sum_i \nabla_i^2 - \sum_{i,l} V_{ext}(r_i) + \frac{1}{2}\sum_{i>j}\frac{e^2}{|r_i - r_j|}\right\}\Psi_n = E_n\Psi_n \qquad 2.10$$

where $V_{ext}(r_i)$ involves the impact of the external magnetic/electric field and the nuclei on electrons.

2.5 The Variational Theorem

The variational theorem indicates that the energy of Ψ' has to be higher than or equal to the exact wave function, Ψ_o. This theorem leads to approximations of a

system's ground state or lowest energy. It chooses a trial wave function that includes variational terms. These terms are slightly altered until the energy is minimised. The expectation of the wave function can determine the energy of the trial wave function, and it is given as,

$$E_{\Psi'} = \frac{\langle \Psi' | \hat{H} | \Psi' \rangle}{\langle \Psi' | \Psi' \rangle} \qquad 2.11$$

The exact energy, E_o, of a system by the trial wave function based on the variational theorem is given as,

$$E_o \leq \frac{\langle \Psi' | \hat{H} | \Psi' \rangle}{\langle \Psi' | \Psi' \rangle} \qquad 2.12$$

This formula forms the basis for convergence in optimisation procedures.

2.6 The Hartree Approach

Although the Born-Oppenheimer approximation helps to simplify the Schrödinger equation, it still fails to account successfully for more complicated systems that are common in real life. Hartree [67], in 1928, for example, successfully proposed a wave function technique for a single electron to solve the time-independent Schrödinger equation for the many-body problem. As a result, the wave function

of the many-body system can be approximated by the Hartree or orbital technique utilising the product of *n* one-electron orbitals, and it is called the Hartree product, which is given as [68],

$$\Psi = \Psi_{1\alpha}(1)\Psi_{1\beta}(2) \dots \Psi_{n\beta}(N) \qquad 2.13$$

where N is the spatial coordinates and spin of one electron in spin orbitals $\Psi_{n\beta}$, the first electron occupies the molecular orbital Ψ_{α} with spin up (α), and the second electron occupies the molecular orbital Ψ_{α} with spin down (β) etc. The limitation of this approach is that the electron-electron interactions are neglected, and the electrons are not treated as fermions, i.e., two electrons cannot be found in the same quantum state shown by Pauli's antisymmetric principle. Therefore, in this Pauli's principle, the system's wave function has to be antisymmetric regarding the exchange of whichever two of the fermions.

2.7 The Hartree-Fock Approach

The limitations of the Hartree product were overcome by Slater [69], Pauli [70], and Fock [71]. For example, in 1930, the Hartree-Fock (HF) approach was released after considering Pauli's antisymmetric principle. This approach is composed of a method to obtain iteratively the lowest energy of a ground state, in which the wave function of *N*-electron can be approximated using a single Slater determinant that consists of occupied spin orbitals as,

$$\Psi = \frac{1}{\sqrt{N!}} \begin{vmatrix} \Psi_{1\alpha}(1) & \Psi_{1\beta}(1) & \cdots & \Psi_{n\beta}(1) \\ \Psi_{1\alpha}(2) & \Psi_{1\beta}(2) & \cdots & \Psi_{n\beta}(2) \\ \vdots & \vdots & \ddots & \vdots \\ \Psi_{1\alpha}(N) & \Psi_{1\beta}(N) & \cdots & \Psi_{n\beta}(N) \end{vmatrix} \qquad 2.14$$

The iterative method, which is also referred to as '*Self-Consistent Field*' (SCF), is applied to solve the system and is considered for the convergence, where there is no change between the field produced by the electronic states and that utilised to predict the electronic states. The HF approach completely neglects the electron correlations and can produce inconsistent results with experimental measurements. The HF approach overestimates the band gap of insulators and semiconductors due to the strong correlation in solid materials. To overcome this issue, the electron correlations were introduced in the Fock operator, which can enhance the accuracy of electronic calculations. Yet, the increase in computational cost makes it challenging, especially in simulating large systems. The HF can account for approximately 99% of the system's total energy, while the remaining 1% is fundamental for the exact description of the chemical attributes of molecules [72]. The correlation energy (E_{HF}^{C}), is defined as the difference between the HF energy (E_{HF}), and the exact energy (E_o) of the system, which is always greater, and is given as,

$$E_{HF}^{C} = E_o - E_{HF} \qquad 2.15$$

2.8 **Density Functional Theory**

An alternative technique to the HF approach that is widely implemented to solve the many-body problem is density functional theory (DFT), which is a quantum mechanical theory applied to introduce the effects of correlation to investigate the ground states of large many-body systems. DFT is a popular and versatile approach compared to post-HF approaches, and the main reason for its popularity is that it is computationally much less expensive. The fundamental parameter in DFT is that it chooses the single particle electron density, $\rho(r)$, instead of the many-body wavefunctions, which is given as,

$$\rho(r) = N \int d^3r_2 \int d^3r_3 \dots \int d^3r_N \Psi^*(r, r_2 \dots r_N)\Psi(r, r_2 \dots r_N) \qquad 2.16$$

The HF approach is used to calculate a molecular wave function. Yet, the wave function is not a measurable parameter of an atom or a molecule. In contrast, DFT focusses on the the electron density, $\rho(r)$, commonly referred to as the electron probability density, rather than being based on the wave function.

2.8.1 Early Approximations

The roots of DFT are based on the approach developed by Thomas-Fermi [73][74] in 1927, which is the first attempt to implement the electron density rather than the wave function. The total electronic energy in the Thomas-Fermi formula is given as,

$$E_{\alpha}[\rho] = \int \rho(r)\varepsilon_{\alpha}[\rho(r)]dr \qquad 2.17$$

where ε_{α} is the contribution of kinetic and correlation/exchange energies. This approach was only based on considering the kinetic energy as a quantum statistical model of a non-interacting, uniform, spin-unpolarised N-electron density, $\rho(r)$, while the contributions of electron-electron and nuclear-electron were treated purely in a classical way. Although the Thomas-Fermi approach roughly provides correct energies with errors of approximately 10% for many systems [75], it does not account for most attributes of interest, such as the binding of molecules [76]. Yet, mapping the electron density to the energy is provided for the first time without any other information needed.

2.8.2 The Hoenberg-Kohn Theorems

The origin of modern DFT relies on the two lemmas developed by Hoenberg-Kohn (HK) in 1964 [77]. The first HK lemma reveals that the ground-state electronic attributes of a many-body system are determined uniquely by the ground-state electron density, $\rho_o(r)$. Alternatively stated, the ground-state wave function, Ψ_0, is a unique functional of $\rho_o(r)$ and is given as,

$$\Psi_0 = \Psi_0[\rho_o] \tag{2.18}$$

The second HK lemma demonstrates that when the variational approach is employed to any trial electron density, ρ', of a system, it will result in molecular energy that is higher than or equal to the exact ground-state energy. The second HK lemma is provided as [68],

$$E[\rho'] \geq E_o[\rho_o] \tag{2.19}$$

The HK theorems demonstrate that there is a one-to-one correspondence between any external potential, $V_{ext}(r)$, and the electronic density, $\rho(r)$, consequently, the total energy functional of the electron density of the ground-state corresponding to the external potential is given as,

$$E_o[\rho_o] = F_{HK}[\rho_o] + \int \rho_o(r) V_{ext}(r) dr \qquad 2.20$$

where $F_{HK}[\rho_o] = T[\rho_o] + E_{int}[\rho_o]$ is known as the HK universal functional and involves all internal energies, potential and kinetic of the interacting electron system. The fundamental issue of the HK approach is that there is no exact expression for the functional $F_{HK}[\rho_o]$ and hence, approximations must be applied.

2.8.3 The Kohn-Sham Theory

At this stage, it has been recognised that for all practical aims, the wave function term does not appear in DFT. That is to say, although the exact ground state energy or electron density can be determined, there is no way to go back to the exact wave function in practice. However, this section will present a strategy for the possibility of building fictitious orbitals. Therefore, a fictitious wave function can be calculated without interaction between particles. Furthermore, this strategy will assist in approximating the ground state energy of the system.

Shortly after the HK approaches, in 1965, Kohn and Sham (KS) [78] proposed independent-particle formulations for a non-interacting electrons system for the solution of the original many-body system, leading to more precise DFT calculations as the kinetic energy of non-interacting electrons is expressed in terms of orbitals. The KS DFT total energy, E_{KS}, can now be expressed as,

$$E_{KS}[\rho(r)] = T_{NI}[\rho(r)] + V_{ne}[\rho(r)] + J[\rho(r)] + E_{XC}[\rho(r)] \qquad 2.21$$

where $V_{ne}[\rho(r)]$ is the interaction functional between nuclei and electrons.

The kinetic energy functional for the non-interacting system, $T_{NI}[\rho(r)]$, and the classical Coulomb interaction energy, $J[\rho(r)]$, of the electron density interacting with itself are expressed as,

$$T_{NI}[\rho(r)] = -\frac{1}{2}\sum_{i=1}^{N}\left\langle \Psi_i^{KS}\middle|\nabla_i^2\middle|\Psi_i^{KS}\right\rangle \qquad 2.22$$

$$\hat{J}[\rho(r)] = \frac{1}{2}\int \frac{\rho(r)\,\rho(r')}{|r-r'|}\,dr\,dr' \qquad 2.23$$

where N is the total number of electrons in the system, r and r' denote the coordinates of two electrons.

The exchange-correlation energy, $E_{XC}[\rho(r)]$, consists of two portions: the exchange-correlation interactions between electrons and the remaining kinetic energy resulting from the particles' interaction. This term can be written as,

$$E_{XC}[\rho(r)] = T[\rho(r)] - T_{NI}[\rho(r)] + V_{ee}[\rho(r)] - J[\rho(r)] \qquad 2.24$$

By solving the single-particle Schrödinger equation, the single electron orbitals can be calculated as,

$$\left(-\frac{1}{2}\nabla^2 + V_{KS}(r)\right)\Psi_i(r) = \varepsilon_i\Psi_i(r) \qquad 2.25$$

There is a direct relationship between KS and HF approaches in which self-consistent formulae must be solved for a number of independent electrons in a number of orbitals. In contrast, the primary difference in the DFT technique is that the external potential, V_{KS}, is defined using the electron density, $\rho(r)$. This resulted from the total of the moduli of the squared of KS electron molecular orbitals, Ψ_i^{KS}, which equals to the total electron density, $\rho(r)$, and is given as,

$$\rho(r) = \sum_{i=1}^{N}\left|\Psi_i^{KS}(r)\right|^2 \qquad 2.26$$

Yet, the analytical form of E_{XC} is unknown except for a free electron gas. Therefore, approximate functionals that are associated with the electron spin density ρ_α and

ρ_β, must be included to describe this term. The approximate functionals implemented by modern DFT techniques are on the basis of these KS self-consistent formulae.

2.8.4 Exchange-correlation Functionals

So far, it has been demonstrated that the exchange-correlation functionals $E_{XC}[\rho(r)]$ play a key role in DFT approximations, where accurate results can be obtained. $E_{XC}[\rho(r)]$ is the only remaining term that is required to be approximated, in order to increase the chemical accuracy of molecules, atoms and solids in their ground states [79]. Over the years, many various exchange-correlation functionals have been proposed and developed. They are categorised into three main types: local density approximation (LDA), generalised gradient approximation (GGA), and/or hybrid functionals.

2.8.4.1 The Local Density Approximation

DFT is a powerful tool that enables us to utilise the exchange-correlation energy functional to evaluate the total energy of a system. The simplest approximation exchange-correlation functional in DFT is the LDA that also provides good results in most attributes such as bond length, shape, and reaction heat. In this

approximation, the electron density, $\rho(r)$, is locally treated as a uniform electron gas, and the approximation exchange-correlation functional is given as,

$$E_{XC}^{LDA}[\rho(r)] = \int \rho(r)\varepsilon_{XC}[\rho(r)]dr \qquad 2.27$$

where ε_{XC} is the exchange-correlation energy per electron.

Although the LDA is a simple approximation and has been commonly employed to save computing resources, it still has some limitations. For example, the binding energies of molecules are often overestimated, and the total energy of the system is underestimated [72]. Furthermore, the band gap of semiconductor materials can also be underestimated.

2.8.4.2 The Generalised Gradient Approximation

In order to overcome the limitations of LDA, a more accurate generalised gradient approximation (GGA) was developed. In this approximation, the exchange-correlation functional depends on both the electron density, $\rho(r)$, and the gradient of electron density, $\nabla\rho$, given at the same point r, which can be written as,

$$E_{XC}^{GGA}[\rho(r)] = \int \rho(r)\varepsilon_{XC}[\rho(r)\nabla\rho(r)]dr \qquad 2.28$$

Based on this idea, various GGA functionals have been incorporated and widely used, such as the Perdew-Burke-Ernzerhof (PBE) [80][81] and the PW91 form [82]. Generally, the GGA provides enhanced bond energies, angles, and lengths. For example, the hydrogen bond strengths between closed systems are significantly superior compared to the LDA results. Nevertheless, the GGA itself insufficiently describes various electronic properties of systems of interest, such as the band gaps and charge transfer between species [83].

2.8.4.3 Hybrid HF/DFT Functionals

As mentioned above, the band gap of semiconductor and insulator materials is underestimated in LDA and GGA techniques, and electronic states are delocalised. In contrast, the band gap is overestimated in the HF technique and makes over localisation of electronic states. Thus, in order to obtain the correct band gap value and localisation of electronic states, a careful mixing between HF and LDA/GGA is needed. This procedure is known as the hybrid functional method that is based on the adiabatic connection approach [84]. The well-known hybrid functional is the PBE0, which was proposed by Adamo and Barone [85], and it can be written as,

$$E_{XC}^{PBE0} = aE_X^{HF} + (1-a)E_X^{PBE} + E_C^{PBE} \quad 2.29$$

where a is the mixing fraction of HF exchange.

Even though hybrid functionals provide improved quality of DFT calculations, they work with an increase in computational cost compared to other techniques where the exchange is completely treated non-locally. Therefore, Heyd, Scuseria, and Ernzerhof (HSE) [86] developed a technique to accelerate the exact exchange computation. In this technique, a screened Coulomb potential is employed in the exchange interaction in order to screen the HF long-range part as,

$$E_{XC}^{HSE} = aE_X^{HF,sr} + (1-a)E_X^{PBE,sr} + E_X^{PBE,lr} + E_C^{PBE} \quad 2.30$$

where $E_X^{HF,sr}$ is the short-range HF functional, $E_X^{PBE,sr}$ and $E_X^{PBE,lr}$ are the short-range and long-range terms of the PBE exchange, and $a = 0.25$ is the mixing fraction of HF exchange.

2.8.5 The Hubbard-U Correction

One of the limitations of the standard LDA and GGA in DFT is that they fail to describe the strongly correlated materials with strongly interacting and localised *d* and *f* electrons. A technique that includes the effective Coulomb correction, i.e.,

LDA+U/GGA+U, derived from the Hubbard model, can solve this issue [87]. In the LDA and GGA, the electrons are split into two types: delocalised electrons located in the *s* and *p* orbitals and localised electrons located in the *d* and *f* orbitals. The exchange-correlation functional in the GGA+U framework is written as [88],

$$E_{GGA+U} = E_{GGA} + \frac{U_{eff}}{2}\sum_{\sigma}\left[\left(\sum_{i}\rho_{ii}^{\sigma}\right) - \left(\sum_{i,j}\rho_{ij}^{\sigma}\,\rho_{ji}^{\sigma}\right)\right] \qquad 2.31$$

and the effective Coulomb correction is given as,

$$U_{eff} = U - J \qquad 2.32$$

where U and J represent the strength of the interactions of the Coulomb and exchange terms, respectively, and ρ_{ii}^{σ} is the on-site density matrix of the *d* and *f* orbitals.

Introducing the effective Coulomb correction parameter forces the orbital occupancy of delocalised electrons to become localised electrons. This technique has been widely implemented to successfully study strongly correlated materials such as transition metal oxides and rare earth elements. However, the determination of U and J is generally obtained empirically [89].

2.8.6 Dispersion Forces

One of the underlying issues with the standard LDA-/GGA-type DFT is that the dispersion forces or van der Waals forces, which describe the charge density response to density fluctuations in other positions of space, are not considered within its basic formula [90]. DFT or HF itself insufficiently describes materials with significant dispersion interactions. Therefore, Grimme [91] formalised an empirical approach to calculate the weak attractive intermolecular forces that are caused by the dispersion (pairwise) interaction. The total energy of the dispersion corrected, E_{DFT-D}, can be written as,

$$E_{DFT-D} = E_{DFT} + E_{Disp} \qquad 2.33$$

where E_{FDT} is the total energy of the chosen density function and E_{Disp} is the dispersion interaction energy.

The coefficients in a D2 dispersion are obtained empirically, and an attractive semi-empirical pair potential produces the D2 dispersion correction as,

$$E_{D2} = -S_6 \sum_{i=1}^{N-1} \sum_{j>i}^{N} \frac{C_{6,ij}}{R_{ij}^6} f_{dmp}(R_{ij}) \qquad 2.34$$

where N is the number of atoms, i and j are the number of interacting atoms, S_6 is a scaling factor, $C_{6,ij}$ and (R_{ij}) are the dispersion coefficient and interatomic distance of atom pair i and j, respectively. $f_{dmp}(R_{ij})$ is a damping function and is written as,

$$f_{dmp}(R_{ij}) = \frac{1}{1 + e^{-d\left(R_{ij}/R_r - 1\right)}} \quad 2.35$$

where R_r is the summation of van der Waals radii.

Later, the initial dispersion correction, including DFT-D3, was developed by Grimme *et al.* [92] where, E_{Disp}, is just the summation of two and three body-term which is given as,

$$E_{D3} = E_2 + E_3 \quad 2.36$$

where $E_2 = E_{D2}$ that is given in Eq. 2.33 and E_3 is written as $\bar{r}ABC$

$$E_3 = \sum_{ABC} f_{d,(3)}(\bar{r}_{ABC}) E^{ABC} \quad 2.37$$

where the sum is over all atom triples ABC, $\bar{r}_{ABC}$ is used as a damping factor.

To summarise the DFT technique used in this thesis, the spin-polarised PBE combined with the Becke-Johnson (BJ) damping function in Grimme's technique is carried out in order in include van der Waals (vdW) corrections due its ability to predict accurate adsorption and binding energies of metal oxides materials. It is found that the inclusion of vdW interactions can modify the order of stability of various isomers and lead to significant corrections to the adsorption energies. Furthermore, the adsorption properties will impact the diffusion and reaction properties of the adsorbates on AQC/oxide surfaces. Due to the self-interaction error resulting in artificial electron delocalization in the standard DFT methodologies, the generalised-gradient approximation (GGA) plus Hubbard term (U-term) is employed, in order to predict the accurate polaronic states and band gap values of TiO_2. The U value implemented to titanium (3d) orbital is 4.2 eV and to cerium (4f) orbital is 6.3 eV.

3 Computational Methodology

In this chapter, I will discuss *ab initio* techniques or first-principle simulation, which is the most common simulation technique based on quantum mechanics. The *ab initio* technique is purely based on the information of the atomic type and position in the system without any fitting or empirical parameters. This chapter provides further details of the modelling parameters used in this thesis. The techniques described in this chapter are implemented via the computational package VASP code, which is used for all the calculations described in the following chapters.

3.1 Implementation of Density Functional Theory in VASP

Several computational software packages apply theoretical physics and chemistry techniques to evaluate the properties and structures of molecules, atoms, and solids. In particular, Kresse *et al*. [93][94][95][96] developed computer software called the Vienna *ab initio* Simulation Package (VASP) for atomic scale materials modelling, such as electronic structure calculations and quantum-mechanical

molecular dynamics. VASP is also used to study interactions in and on metal oxide materials. It uses plane waves in a periodic system with projector-augmented wave pseudopotentials (PAW-PP) [97][98]. VASP is the principal DFT code used throughout the work described in this thesis.

PAW-PP includes the valence electron's wave function and the wave function nodes for the core electrons, where the core electrons remain fixed during the optimisation process. This method limits the number of plane waves needed to simulate the system. The cut-off energy for the plane waves is set to 500 eV for all modelled systems in this thesis. VASP applies efficient matrix diagonalization and a Broyden [99] mixing technique to solve the KS ground-states equations self-consistently. This mixing is employed to obtain convergence in DFT calculations. The GGA-type DFT is implemented with the PBE functional. The self-consistency procedure is a three-stage procedure. The Hamiltonian is set up in the first stage by using the charge density. In the second stage, the wavefunctions are iteratively calculated until a closer value of the exact wavefunctions of the Hamiltonian is obtained. A new charge density is obtained in the third stage from the optimized wavefunctions. Using the Broyden mixing technique, the new charge density is combined with the input-charge density. The self-consistent procedure used in this thesis is presented in Fig. 3-1.

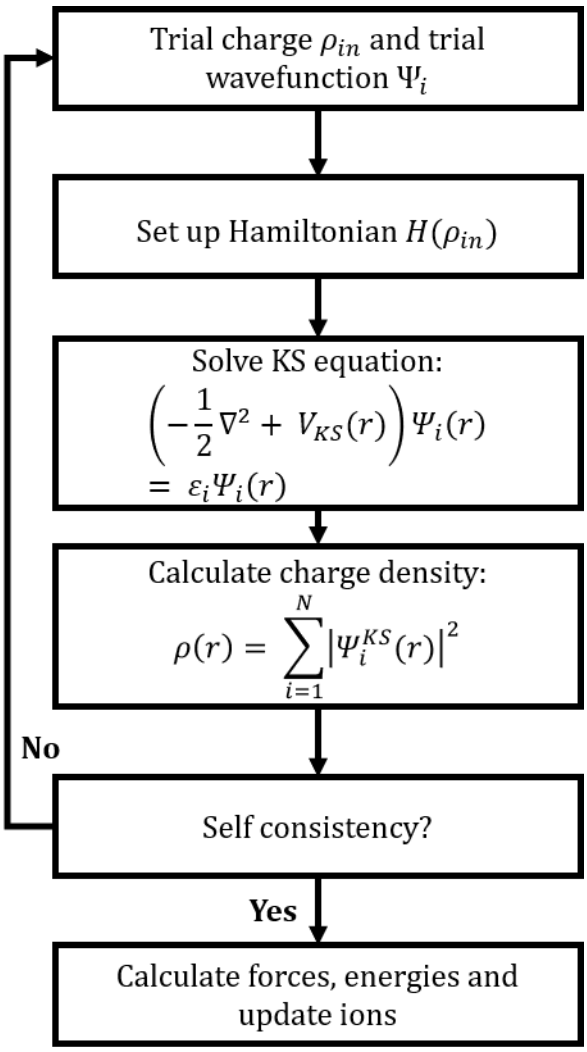

Fig. 3-1 Self-consistent procedure used in this thesis.

3.2 **Geometry Optimisation**

Geometry optimisation is defined as the process in which the local energy minimum on the potential energy surface is found as the energy of the system is minimised; following this, the most stable configuration of a given system is

obtained. Some material properties such as, defect thermodynamics or electronic structures can significantly be altered if geometry optimisation is not conducted. In order to optimise modelled systems and to check the ions movement and update, a conjugate-gradient algorithm (CGA) [100][101] is implemented by specifying the tag (IBRION=2) in the input file for VASP in this thesis. The CGA is done by evaluating the steepest descent in a three-stage procedure (Initial, trial, and corrector stages). In the first stage, the steepest descent is assessed from the calculated energies and forces, and the positions of ions are altered accordingly. The process is repeated in the second and third stages until a minimum energy configuration is obtained or within the specified cut-off. A new gradient is evaluated after the first stage and subsequent stages.

A Gaussian spreading value is used by setting (ISMEAR=0) tag for band occupation due to the large supercell used in the tetrahedron technique along with a small value of smearing width by specifying the (SIGMA=0.05 eV) tag. For the self-consistent minimisation, a convergence threshold value is fixed by using (EDIFF=10^{-4} eV) tag, and all modelled structures are allowed to relax with a threshold force value of (EDIFFG=0.02 eV/Å) tag. A *k*-point mesh was sampled based on the Monkhorst-Pack scheme [102][103] in which all the simulations are made using a single value of *k*-point (i.e., a Γ-centred mesh). This is because all the simulated systems presented in this thesis are large enough leading to a small reciprocal space. Therefore, a small *k*-point mesh is enough to evaluate the change across the Brillouin zone accurately. The use of a single value of *k*-point describes acceptable electronic structures of insulators/semiconductors.

TiO_2 and CeO_2 behave like most transition metal oxides in which they have errors in DFT calculations, which are triggered by being strongly correlated systems. As previously described in section 2.8.5, it is necessary to include the U-term in the calculations in order to yield accurate electronic structure results. For the case of TiO_2, the U value implemented to Ti 3*d* orbital in this thesis is 4.2 eV, which was reported initially by the work done by Morgan and Watson [104][105][106]. At this value, the band gap values are closely comparable to the experimentally measured values for both rutile and anatase TiO_2 [107]. For the case of CeO_2, the U value implemented to Ce 4*f* orbital must be large enough in order to accurately describe the localisation of the 4*f* electron of Ce^{3+}. Therefore, I performed GGA+U calculations using the PBE functional on the CeO_2 bulk structure with a U value of 6.3 eV [108][109][110]. At this value, a band gap value of 3 eV is obtained, which is in excellent agreement with the experiment [111][112].

3.3 **Pseudopotentials and Projected Augmented Wave Techniques**

One of the primary drawbacks of employing plane-waves in DFT is the increased number of the plane-waves (more than 10000 planewaves) required to describe the rapid fluctuations of the wave functions in the core region, thus significantly increasing the computational cost. It is worth mentioning that most

physical/chemical properties of molecules and solids merely depend on their valence electrons, while the contribution of the core electrons can be negligible.

Consequently, to make a significant acceleration in the calculations, the all-electron problem can be treated as a valence-electron problem, including weaker nuclear potentials known as pseudopotentials (PSPs). This is the advantage of the pseudopotential technique [113][114][115][116], where a pseudopotential replaces the strong core potential. In other words, actual complicated wave functions can be replaced by more straightforward wave functions using pseudopotentials, while retaining the crucial properties of the system with a reduction in computational cost [117]. It should be noted that the Ti (3*s*, 4*s*, 3*p*, 3*d*), Ce (4*f*, 5*d*), O (2*s*, 2*p*), Si (3*s,* 3*p*), and Ag (4*d*, 5*s*) atomic orbitals are explicitly treated as valence electrons. A comparison between the core-wavefunction and pseudo-wavefunction is displayed in Fig. 3-2.

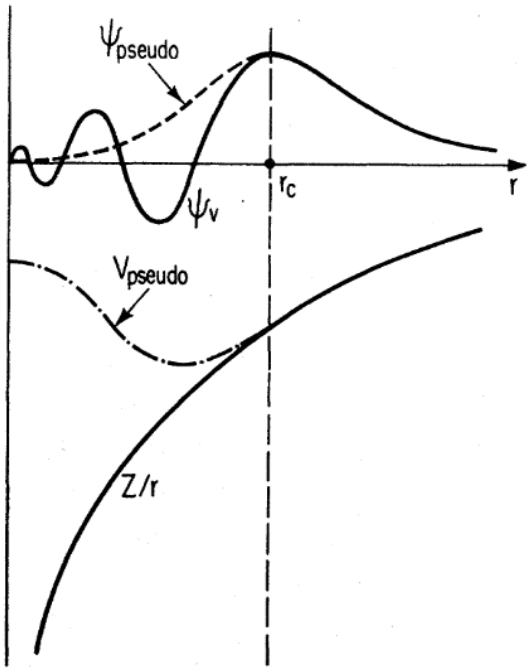

Fig. 3-2 Schematic illustrations of the real wavefunction (Ψ_v), pseudo-wavefunction (Ψ_{pseudo}), and their corresponding potential and pseudopotential [115]. r_c is the radius where the core-wavefunction and pseudo-wavefunction meet.

An alternative method to PSPs is the projector augmented wave (PAW) developed by Blöchl [98], which produces even smoother wave functions near atomic centres. The PAW method involves auxiliary localised functions like the 'ultrasoft' pseudopotential technique, meaning that many parts of the calculations are identical to pseudopotential calculations. The transformation of the rapidly fluctuating valence wave functions Ψ of single-particle near the nucleus, with $\widetilde{\Psi}$ being a number of smooth auxiliary functions, is the central characteristic of PAW formalism,

$$\Psi = T\widetilde{\Psi}, \qquad T = I + T_0 \tag{3.1}$$

where T_0 in Eq. 2.37 takes the form,

$$T_0 = I + \sum_R S_R \tag{3.2}$$

where R is non-overlapping spheres positioned around the atoms. To obtain the real wave function formula, the real and auxiliary wave functions are expanded as linear combinations of plane waves within the spheres R as [98],

$$|\Psi\rangle = |\widetilde{\Psi}\rangle + \sum_m C_m\{\langle\Psi_m| - |\widetilde{\Psi}_m\rangle\} \tag{3.3}$$

The combination of the real all-electron valence wave functions appeared in Eq. 2.39, and the transformation that appeared in Eq. 2.37 can be written by inserting projector functions $|p_m\rangle$, as [98],

$$|\Psi\rangle = |\widetilde{\Psi}\rangle + \sum_m \left(\langle\Psi_m| - |\widetilde{\Psi}_m\rangle\right) \langle p_m|\widetilde{\Psi}\rangle \tag{3.4}$$

$$T = I + \sum_m \left(\langle\Psi_m| - |\widetilde{\Psi}_m\rangle\right) \langle p_m| \tag{3.5}$$

Then, expectation values of operators are calculated as,

$$\langle A \rangle = \sum_m C_m \langle \Psi_m | A | \Psi_m \rangle = \sum_m \left(\langle \widetilde{\Psi}_m | T^\dagger A T | \widetilde{\Psi}_m \rangle \right) \quad 3.6$$

Finally, the expression for the energy can be given as,

$$E = \tilde{E} + \sum_R \left(E_R^1 - \tilde{E}_R^1 \right) \quad 3.7$$

To conclude this section, it can be stated that the PAW method improves upon the PSPs technique, with respect to the transferability of the PSPs, and yields more accurate results for evaluating electronic structures of systems. Therefore, this thesis has routinely utilized the PAW method to study the surface interactions of the modelled metal oxides and their electronic structures.

3.4 Periodic Supercell and Implementing Plane Waves Basis Set

In order to model a solid-state system, it is unavoidable to handle a perfect crystal that includes infinite electrons. Moreover, an infinite number of wave functions and an infinite basis set are needed to describe the electronic behaviour of such a system. Consequently, a supercell, a finite unit cell that can be periodically repeated throughout 3-dimensional spaces, is built, as presented in Fig. 3-3 [118].

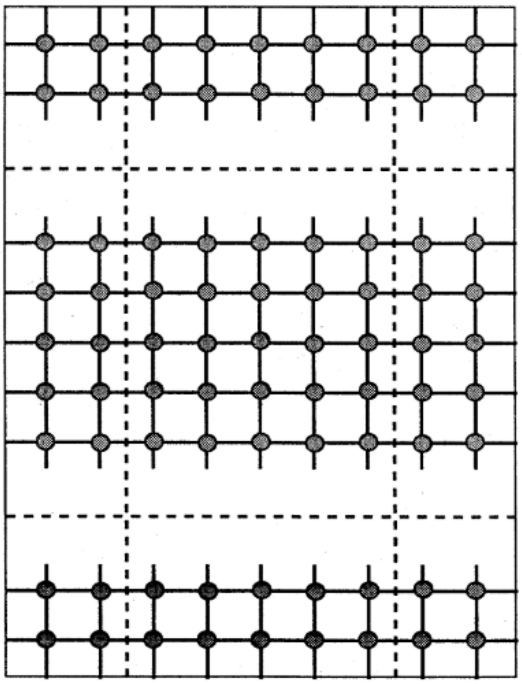

Fig. 3-3 Schematic illustrations of a periodic supercell of the slab model [118].

It has been argued that the most appropriate basis sets implemented are plane waves of the form e^{ikr} due to their efficient translation into a periodic formalism [119]. The periodic wave function also referred to as the Bloch wave, can be obtained from Bloch's theorem, which states that the wave function of an electron in a periodic system can be extended as the product of a wave and periodic part as,

$$\Psi(r) = e^{(ikr)}u_{ik}(r) \qquad 3.8$$

where $u_{ik}(r)$ function corresponds to the periodic part and $e^{(ikr)}$ corresponds to the wave part, k is the crystal wave vector describing the reciprocal lattice in the first Brillouin zone.

u_{ik} can be expanded to the periodic function applying a plane wave basis set as,

$$u_{ik}(r) = \sum_{G} C_{i,G} e^{iGr} \qquad 3.9$$

where C_i is the expansion coefficient and G is the reciprocal lattice vector. Therefore, the wave function can now be written as a linear combination of plane waves as,

$$\Psi(r) = \sum_{G} C_{i,G} e^{[i(G+k).r]} \qquad 3.10$$

Eq. 3.10 includes an infinite, but discrete number of plane waves, which thus makes it feasible to select an appropriate set of waves to be involved in the expansion by opting for a pre-defined cut-off energy $\frac{1}{2}|k+G|^2$. This choice may cause errors in the calculations; however, these errors can be removed by increasing the value of the cut-off energy in a step-by-step process until the total energy is converged. Following this, the cut-off energy value remains fixed for the

following part of the calculations. In other words, the precision of the basis set is controlled by the cut-off energy, which is unknown in advance; therefore, the total energy must be converged to obtain a successful calculation.

3.5 Calculated Parameters

3.5.1 Density of States

The electronic density of states (DOS) is an essential quantity used to analyse a simulated system's electronic structures in VASP. The DOS is defined in terms of the number of available states with energies below the Fermi energy level, known as the highest occupied molecular orbitals (HOMO), and with energies above the Fermi energy level, known as the lowest unoccupied molecular orbitals (LUMO). For bulk systems, the DOS per unit volume at energy can be written as,

$$D = \frac{1}{V}.\frac{N(E, E + \Delta E) - N(E)}{\Delta E} = \frac{1}{V}.\frac{dN}{dE} \qquad 3.11$$

For a free electron gas, this becomes

$$D = \frac{1}{V}.\frac{dN_s}{dE} = \frac{1}{2\pi^2}\left(\frac{2me}{\hbar^2}\right).E^{\frac{1}{2}} \qquad 3.12$$

where V is the volume of the cell, E is the energy of the system, N_s denotes the number of states, m is the electron mass and $\hbar^2 = \frac{h}{2\pi}$ where h is Planck's constant. The total DOS can be defined as the sum of the band contributions at a certain eigenvalue. The DOS is disintegrated into the projected DOS (pDOS) based on the individual contributions of atoms included in the system. As an illustrative example, the pDOS for the pristine surface of rutile TiO_2 (110) is shown in Fig. 3-4. It is worth mentioning that the Femi energy level is automatically shifted to zero eV when the calculations performed by Vaspkit software for all presented DOS figures.

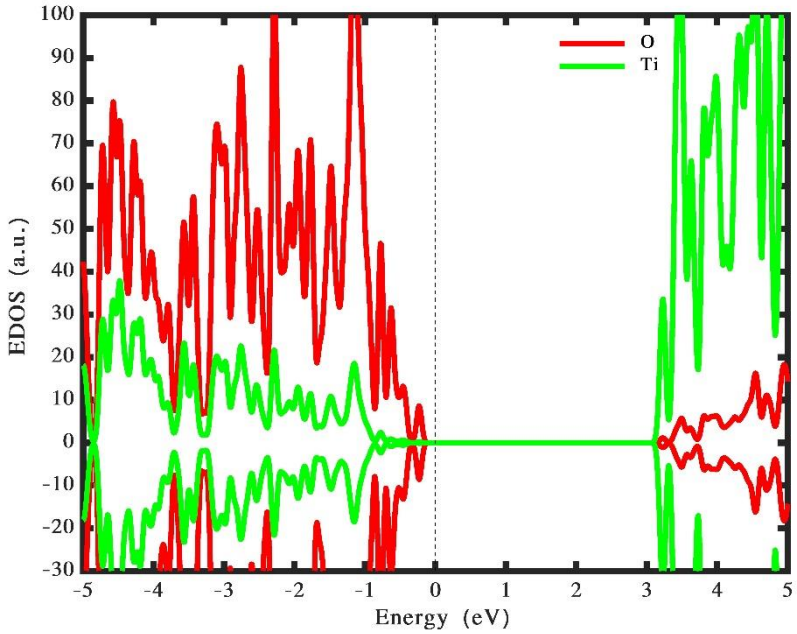

Fig. 3-4 Projected DOS of pristine rutile TiO_2 (110) surface calculated by VASP using the spin polarised GGA+U/HSE06 technique. The vertical dashed line represents the Fermi energy level which is set at 0 eV. The Green and red

curves represent the contribution of the atom and oxygen orbitals, respectively.

Generally, a comparison can be made between the DOS and experimental methods such as Hard X-ray Photoelectron Spectroscopy (HAXPES) or Valence-Band X-ray Photoelectron Spectroscopy (VB-XPS). ***"While I am writing this paragraph, my first baby girl is born (April, 2022)"***. This comparison can be fulfilled by implementing both Lorentzian and Gaussian broadenings and by weighting the DOS with atomic orbital photo-ionisation cross sections reported by Scofield [120] or Yeh and Lindau [121]. This approach has been successfully used in various works to accurately describe the electronic states that are generated by the XPS measurements [122][123][124][125][126][127].

3.5.2 Energy Calculations

The stability of the catalysts during chemical reactions is one of the most critical problems for practical uses. Therefore, the adsorption energy, E_{ads}, is usually computed to evaluate the adsorption stability based on the following formula,

$$E_{ads} = E_{total} - E_{slab} - E_m \qquad 3.13$$

where E_{total} is the total energy of slab/catalyst and adsorbate in the same cell, E_{slab} is the total energy of the slab/catalyst and E_m is the total energy of the isolated adsorbate. By the definition of adsorption energy, a negative value represents a stable adsorption mechanism.

In order to obtain a reduced/defective system, one of the oxygen atoms of the bulk system is removed. Then, the formation energy of an oxygen vacancy, E_{V_O}, can be computed as,

$$E_{V_O} = E_{Surf+V_O} + \frac{1}{2}E_{O_2} - E_{Surf} \qquad 3.14$$

where E_{Surf+V_O} is the total energy of the reduced/defective slab, $E_{O_2}$is the total energy of free oxygen in the gas phase and E_{Surf} is the total energy of the perfect/stoichiometric slab. It is worth mentioning that both adsorption and formation energies are evaluated at the GGA+U levels.

3.5.3 Bader Charge Analysis

Calculations in this thesis implement DFT to compute charge density. The concept of an atomic charge is usually used to explain and investigate reactivity and structural differences. Bader devised one of the most rigorous strategies for

calculating charges on individual atoms [128][129]. In this strategy, the electron density, which is a function of three spatial coordinates, $\rho(x, y, z)$, of a system produced by the calculations of planewaves can be analysed. Nuclei behave as point attractors located in a cloud of electrons. For instance, a maximum of the charge density function is obtained at the position of the nuclei and decays significantly away from these points.

Henkelman *et al*. [130][131][132] developed an algorithmic technique that is a fast grid-based way for the Bader decomposition of electron density. Steepest descent trajectories are used in this technique; however, these are confined to the grid points and utilised to show the Bader region. In the near-grid method, (*i, j, k*) defines a grid point, and from this point, the trajectory of the steepest ascent is made in the direction that increases the charge density gradient, $\nabla\rho$, which can be calculated along the direction $\hat{r}$ as,

$$\nabla\rho(i,j,k).\hat{r}(di,dj,dk) = \frac{\Delta\rho}{|\Delta\vec{r}|} \qquad 3.15$$

where $\Delta\rho$ and $|\Delta\vec{r}|$ include the components of the charge density in the *x*,*y*, and *z* directions and are given as

$$\Delta\rho_x = \frac{\rho(i+1,j,k) - \rho(i-1,j,k)}{|\vec{r}(i+1,j,k) - \vec{r}(i-1,j,k)|} \qquad 3.16$$

$$\Delta\rho_y = \frac{\rho(i,j+1,k) - \rho(i,j-1,k)}{|\vec{r}(i,j+1,k) - \vec{r}(i,j-1,k)|} \quad 3.17$$

$$\Delta\rho_z = \frac{\rho(i,j,k+1) - \rho(i,j,k-1)}{|\vec{r}(i,j,k+1) - \vec{r}(,j,ki-1)|} \quad 3.18$$

Implementing the PAW pseudopotentials method in VASP calculations, the charge density information is obtained in output CHGCAR files which only include the valence charge density. In order to obtain the core charge in the PAW calculations, it is necessary to use the (LAECHG=. TRUE.) tag in a VASP calculation input file. Then, the sum of both the valence and core charge densities can be computed and analysed by implementing the Bader code devised by Henkelman *et al.* [130][131][132]. As an illustrative example, Table 3- 1 presents the Bader charge analysis for a single unit cell of bulk TiO_2 calculated using PBE.

Table 3- 1 Bader charge analysis for a single unit cell of bulk TiO_2 calculated using PBE.

Element	Bader charge (e)	Minimum distance (Å)	Atomic volume
Ti_1	9.566123	0.924626	6.843542
Ti_2	9.566123	0.924626	6.843542

O_1	7.216263	0.891349	12.647875
O_2	7.217614	0.891349	12.654570
O_3	7.217643	0.891349	12.655599
O_4	7.216234	0.891349	12.646847

3.6 **Software Packages**

The simulations presented in this thesis use the software packages given below.

VASP (https://www.vasp.at/)

VASP [93] is a plane-wave all-electron code implementing either the PAW or Vanderbilt pseudopotentials technique to describe the interaction of the electron core. VASP implements DFT as well as post-DFT corrections, e.g., hybrid functionals combining DFT with the Hartree-Fock exchange functional such as PBE0 [133], B3LYP [134], and HSE [135]. In the VASP code, fast iteration methods for the diagonalization of the DFT Hamiltonian are used, and the performance of total-energy calculations as well as structural optimisations for materials with thousands of atoms, are allowed. All DFT calculations in this thesis were carried out using VASP.

VESTA (http://jp-minerals.org/vesta/en/)

Visualisation for electronic and structural analysis (VESTA) [136] is a 3D visualisation system for crystallographic examinations and electronic structure calculations. VESTA has several features, including the construction of crystal structures, visualisation of crystal morphologies, estimations of nuclear and electron densities from structure parameters, simulations of the powder diffraction pattern, manipulation of structural models and crystal faces, visualisation of isosurfaces with several levels, etc. It can also generate a VASP input file (i.e., POSCAR) that contains all atomic coordinates. All the presented structures are constructed and visualised in this thesis work using VESTA.

MATLAB (https://ch.mathworks.com/products/matlab.html)

MATrix LABoratory (MATLAB) [137] is a multi-functional programming language and computing environment that can manipulate enormous amounts of data. These data can then be analysed through prewritten scripts or the graphical interface. All the figures shown in this thesis are plotted using MATLAB code.

4 Ag_5 Deposited on Anatase (101) and Rutile (110) TiO_2 Surfaces

This chapter summarises the study of the interaction between subnanometer metal clusters and the oxides to shed light on the enhancement of photocatalytic activity. Geometric and electronic structures of Ag_5 AQCs adsorbed on both pure and reduced anatase (101) and rutile (110) TiO_2 surfaces are investigated using DFT+U calculations. Adsorption mechanisms that characterise deposited Ag_5 AQCs on the substrates surfaces in terms of the highest stability are examined. Formation energies of a single oxygen vacancy with and without the presence of Ag_5 AQCs on the oxide surfaces are explored. Sub-bandgaps that are induced by both the oxygen vacancy and adsorbed Ag_5 AQCs are investigated in terms of their formation and positions.

4.1 Introduction

Titania is one of the most studied metal oxides due to its unique attributes particularly as a photocatalyst material. However, as mentioned in **Chapter 1**, its large band gap prevents it to absorb visible light photons. Therefore, there have

been a tremendous number of studies attempting to improve its optical response in the visible light region, one of which is the fabrication of noble metals on top of a TiO_2 surface. For example, Rusinque *et al*. [138] used a sol–gel approach to fabricate mesoporous TiO_2 decorated with Pd to study photocatalytic performance. Among the different amounts of doped Pd cocatalysts (i.e., 0.25–5 wt%), 0.25 wt% Pd@TiO_2 yielded the highest activity in the presence of ethanol as a hole scavenger under visible light. Yu *et al*. [139] synthesised Pt fabricated on TiO_2 nanosheets with exposed (001) facets using a simple hydrothermal process. Their study used an ethanol solution as a sacrificial reagent for trapping holes. It was found that loading with 2 wt% of Pt nanoparticles exhibited the highest photocatalytic performance, and this can be attributed to the efficient charge separation caused by loading Pt nanoparticles.

A more recent study was conducted by Gogoi *et al*. [140]. In their study, a simple chemical reaction technique was implemented for synthesising an Ag-modified TiO_2 photocatalyst. It was found that among different amounts of Ag deposited on TiO_2, 1.5Ag@TiO_2 yielded the highest photoactivity for hydrogen generation in the presence of sacrificial agents (i.e. a mixture of Na_2SO_3, Na_2S and ethanol). This could be explained by the presence of oxygen vacancies, efficient charge separation, and surface plasmonic resonance (SPR), resulting in the minimisation of the band gap energy. Another recent work was reported by Ren *et al*. [141]. In their work, density functional theory (DFT) was employed to systematically study the influence of deposited 4d transition metals (TM) on photocatalytic activities of an anatase TiO_2 (101) surface. It was concluded that among the different studied

4d TM atoms, the deposition of both Ag and yttrium (Y) could effectively enhance the visible-light response of the anatase TiO_2 (101) surface.

Lopez-Caballero *et al*. [142] theoretically studied the effect of the small Ag_5 atomic quantum clusters (AQCs) on perfect and reduced rutile TiO_2 (110) surfaces and the mechanism of improved photocatalytic activity via first-principles modelling. It was predicted that Ag_5 AQCs induce the formation of surface polarons by donating unpaired electrons to TiO_2, which tailor the band gap of titania and therefore, boosts its photocatalytic activity. These studies demonstrate that Ag_5 atomic clusters on both perfect and reduced rutile TiO_2 (110) surfaces improve the optical response of the substrate by enlarging its absorption range toward the visible light region. Moreover, Lopez-Caballero *et al*. [29] carried out X-ray absorption spectroscopy (XAS) and diffuse reflectance spectroscopy (DRS) measurements to investigate the properties of $Ag_5@TiO_2$. These were accompanied by DFT calculations of their electronic and optical properties. It was pointed out that large photogenerated polarons are formed at the interface of Ag_5-modified TiO_2. Their results also indicated that $Ag_5@TiO_2$ are visible-light photo-active materials and show potential for CO_2 reduction.

The aim of this chapter is to investigate the geometries and electronic structures of Ag_5 AQCs on perfect and reduced anatase (101) and rutile (110) TiO_2 surfaces using a mixture of DFT/HF. Photocatalytic activity of both titania surfaces is boosted upon adsorption of silver AQCs. This could be attributed to charge transfer

from the metal to the substrate. We also note the formation of a single polaron either on the top layer or the sub layer of the substrate. Based on density of states calculations, we observe states within the band gap, which are the result of depositing Ag_5 AQCs. The number of these gap states is further increased by releasing an oxygen atom from the metal oxide. These gap states can match the solar radiation and absorb its photons. Upon deposition of Ag_5 AQCs, the energy needed to form an oxygen vacancy on the top layer of both surfaces are higher than the pristine surfaces.

4.2 Results and Discussion

4.2.1 Geometrical and Electronic Properties of Ag_5 Cluster

The optimised structures of both bipyramidal and trapezoidal Ag_5 AQCs in the gas phase are presented in Fig. 4-1 (a) and (b). Both structures shown in Fig. 4-1 are obtained for the doublet state. These calculations reveal that in the gas phase, the trapezoidal shape (Fig. 4-1 (b)) is more stable than the bipyramidal shape (Fig. 4-1 (a)) by 0.49 eV in energy. The bipyramidal Ag_5 cluster shown in Fig. 4-1 (b) is not precisely of D3h symmetry and is composed of equatorial Ag atoms (a triangular

ring) with axial Ag atoms (top sites) above and below the ring. The three equatorial atoms are not all equivalent, since the three bonds shaping the triangle i.e., r_1 are equal to 2.67 Å, whereas the remaining bond i.e., r_4 is 3.04 Å. The bonds r_2 and r_3 formed by axial Ag with the three equatorial sites are equal to 2.69 Å and 2.75 Å respectively (see details in Table 4- 1). The single unpaired electron of the Ag_5 (doublet with S = ½) (see Fig. 4-1 (c)) is mainly situated on the two axial Ag atoms, and is similar to the charge distribution of Cu_5 [143] and Cu_7 cluster [144].

An unrestricted spin scheme utilising VASP.5.4.4 was implemented to appropriately treat the spin-polarisation of Ag_5 clusters. The bipyramidal configuration has energy gaps of 0.95 eV and 1.35 eV for spin up and spin down, respectively, which are smaller than those of the trapezoidal Ag_5 (spin up: 1.85 eV, spin down: 1.8 eV). The singly occupied molecular orbital (SOMO)-lowest unoccupied molecular orbital (LUMO) gaps of both structures were also estimated (0.95 eV for bipyramidal and 1.85 eV for trapezoidal configurations) from the DOS figures (see Fig. 4-1 (c) and (d)).

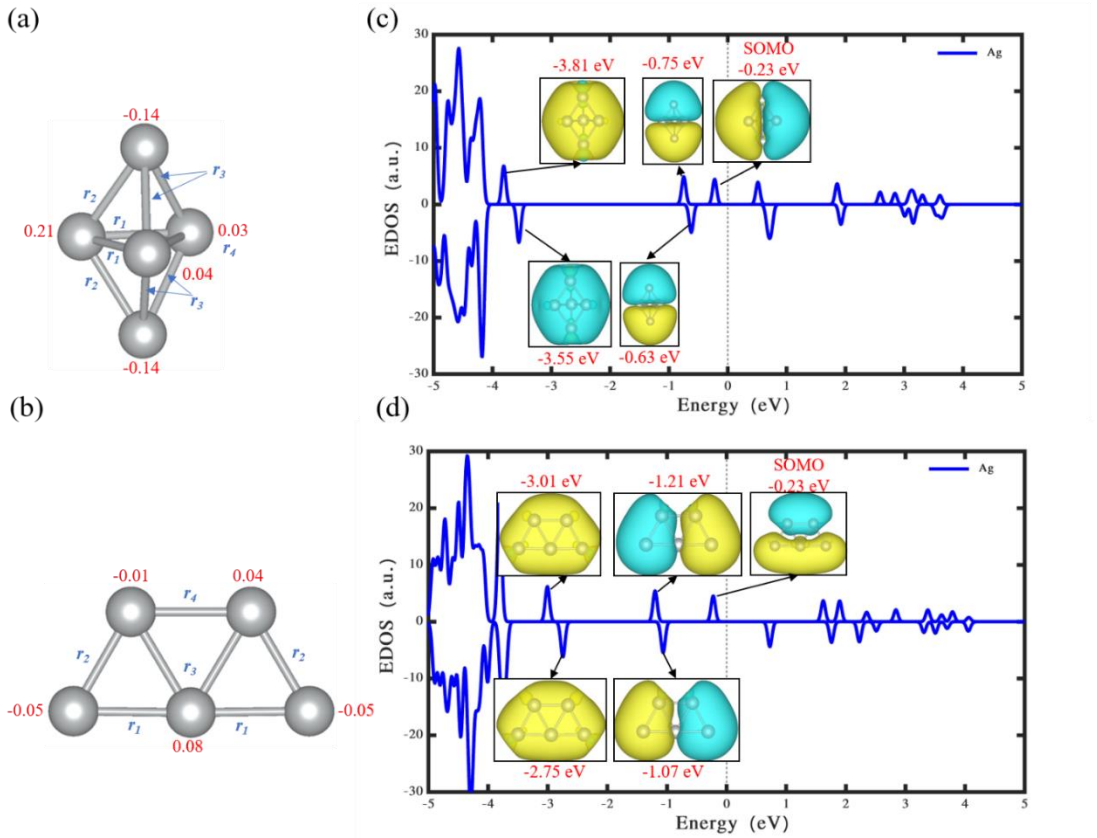

Fig. 4-1 Bipyramidal (a) and trapezoidal (b) Ag_5 isomers in the gas phase. Red numbers represent the net Bader charge distribution on each atom. r_1-r_4 show the Ag-Ag bond lengths. The corresponding values are shown in Table 1. (c) Density of states and frontier molecular orbitals of bipyramidal Ag_5. (d) Density of states and frontier molecular orbitals of trapezoidal Ag_5. SOMO: singly occupied molecular orbital. The yellow and blue reference colours of isosurfaces represent the positive and negative phases of wave functions (Note: the same reference colours are defined for all the wavefunction plots in subsequent figures.) and the isosurface value is 3.42×10^{-9} (a.u.). The vertical dashed line represents the Fermi energy level, which is set at a reference energy of 0 eV.

Table 4- 1 Bond lengths of bipyramidal and trapezoidal Ag_5 isomers obtained using the hybrid functional HSE06.

Bond length (Å)	Bipyramidal Ag_5	Trapezoidal Ag_5
r_1	2.67	2.68
r_2	2.75	2.69
r_3	2.80	2.75
r_4	3.04	2.73

After the investigation of isolated Ag_5, in order to gain further insights into the geometrical stability and electronic states when Ag_5 AQCs are deposited on TiO_2 surfaces, we first simulated the pristine TiO_2 (Fig. 4-2) as a benchmark. Specifically, a four-layer slab of rutile TiO_2 (110) and a three-layer slab of anatase TiO_2 (101) were constructed as shown in Fig. 4-2. As expected, the projected density of states presented in the right panels in Fig. 4-2 reveal that the valence band is mainly dominated by O (2*p*) orbitals, whereas the conduction band is mainly associated with Ti (3*d*) orbitals. The calculated band gap using the hybrid functional for rutile TiO_2 (110) is approximately 3.2 eV, which is in good agreement with experiment [145] and with previous DFT studies [146] and for anatase TiO_2 (101) is around 3.6 eV, which is close to measured values [147][148]. Starting from these structures, defective (Fig. 4-3, Fig. 4-4, Fig. 4-5 and Fig. 4-6)

TiO_2 surfaces are studied in **Section 4.2.2**. and simulations of AQCs on these different surfaces are presented in **Section 4.2.3** and **Section 4.2.4**.

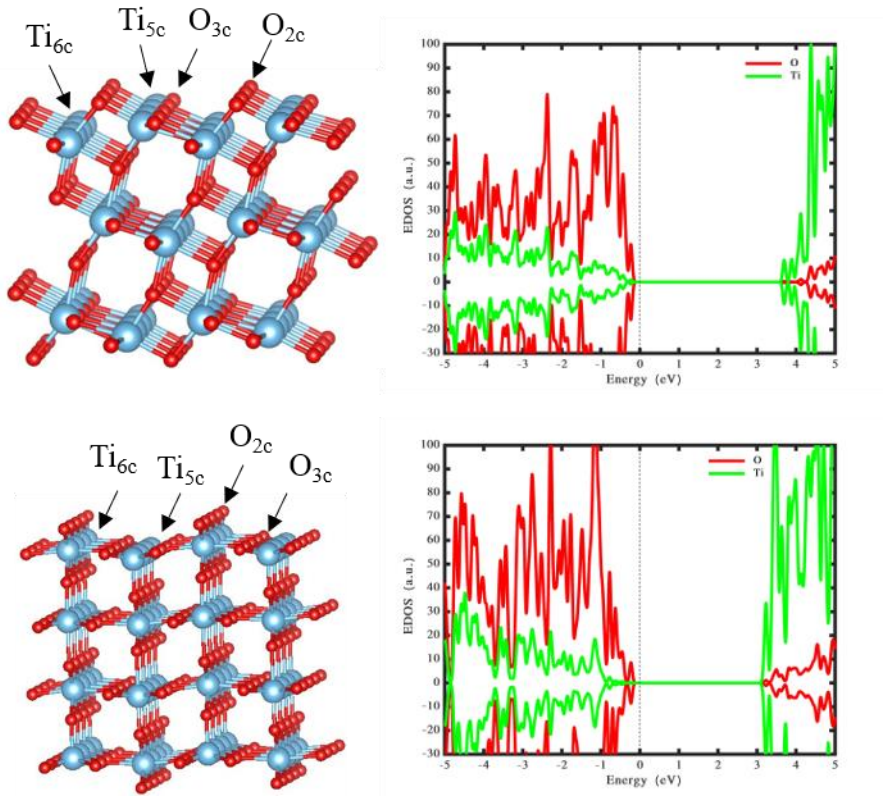

Fig. 4-2 Side view of optimised structures of pristine anatase TiO_2 (101) and pristine rutile TiO_2 (110). In the left panels, the blue spheres denote Ti atoms, and red spheres denote O atoms (the colour scheme is used in the following figures). O_{2c} denotes the two-fold coordinated oxygen atom while O_{3c} represents the three-fold coordinated oxygen atom. Ti_{5c} stands for the five-fold coordinated titanium atom while Ti_{6c} is for the six-fold coordinated titanium atom. In the right panels, green and red curves depict the projected density of states on titanium and oxygen atoms, respectively, while the black vertical dashed-line represents the Fermi energy level.

4.2.2 Oxygen Vacancies at Surface and Subsurface Sites of Anatase TiO_2 (101) and Rutile TiO_2 (110)

4.2.2.1 Reduced Anatase TiO_2 (101)

As a benchmark test, simulations of the relative energetics of surface and subsurface oxygen vacancies are carried out. According to the results obtained for the different oxygen vacancy sites i.e., surface and subsurface (see Fig. 4-3), it is found that the lowest formation energy is 4.26 eV when a two-fold coordinated oxygen atom (O_{2c}) is removed from the top layer of the slab as shown in Fig. 4-4. While the formation energy of an oxygen vacancy in the sublayer of the slab is a 0.43 eV higher in energy (see Fig. 4-3). Our findings are in good agreement with DFT+U calculations for a higher U values i.e., > 3.5 eV conducted by Cheng and Selloni [149].

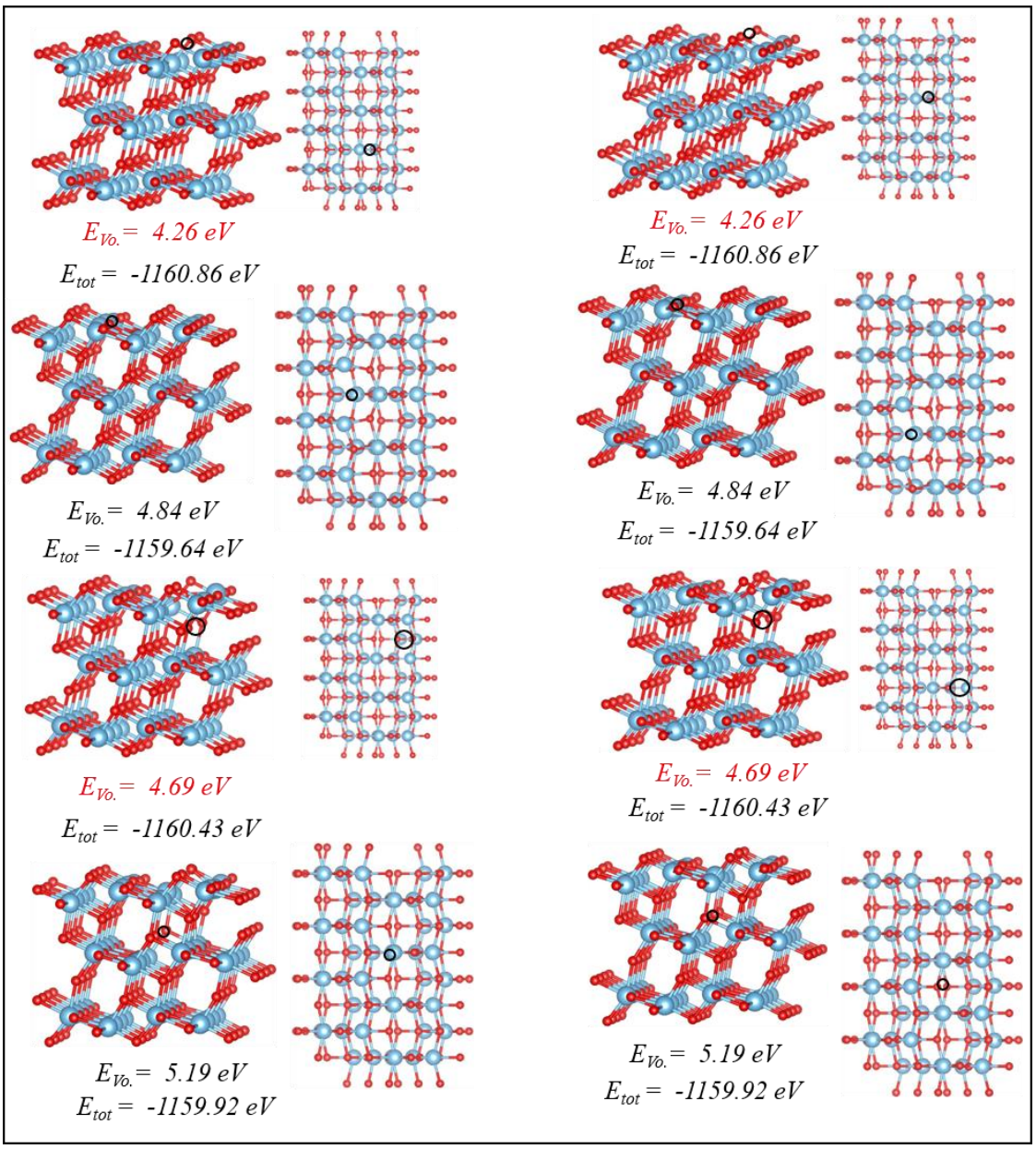

Fig. 4-3 Creation of an oxygen vacancy at surface and subsurface sites of rutile TiO_2 (110). The black circles indicate the oxygen vacancy site, the values in the first line represent the formation energy of oxygen vacancy, while the values in the second line represent the total energy of the system.

Cheng and Selloni [149] studied the formation energy of oxygen vacancy on an anatase TiO_2 (101) surface as a function of the U value and found that the

formation energy is extremely sensitive to the choice of U. In particular, the formation energy of the sublayer is higher than the top layer, when U lies between 3.5 and 4.5 eV. Whereas the formation energy of the top layer becomes lower as compared to the sublayer, when the U value ranges between 2.5 eV and 3.0 eV. To illustrate the electronic structures of the reduced anatase TiO_2 (101) surface, Fig. 4-4 shows its optimised configuration. Two excess electrons localise at a five-fold coordinated titanium atom (Ti_{5c}) and a six-fold coordinated titanium atom (Ti_{6c}) creating polaronic states (pink peak at −0.23 eV and cyan peak at −0.60 eV) which are 1.16 eV and 1.53 eV bellow the conduction band edge, respectively. These sates are also called hybrid states because the electron is located on and shared by two titanium atoms simultaneously (see the wavefunction plots in Fig. 4.4).

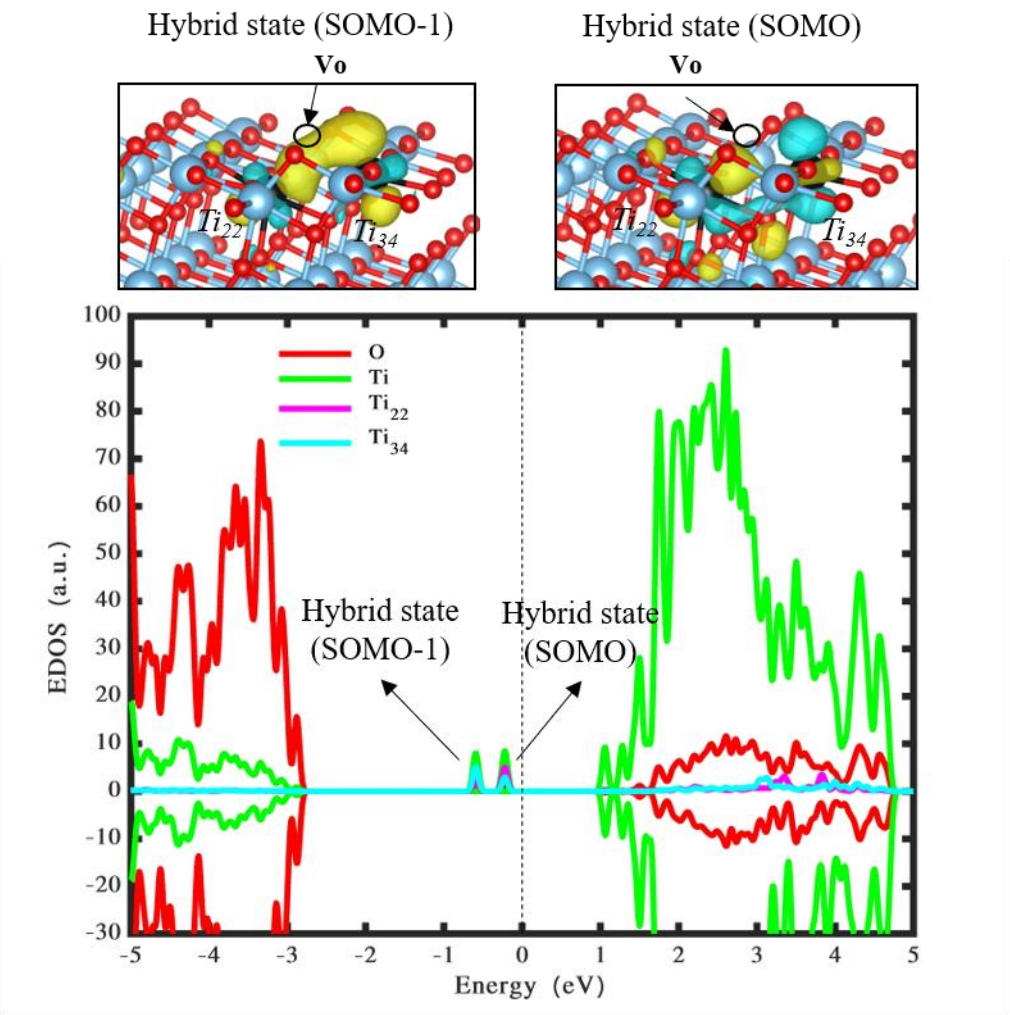

Fig. 4-4 Wavefunction and density of states of reduced anatase TiO_2 (101) surface. The green, red and blue show the states located on titanium, oxygen and silver atoms, while the pink and cyan peaks between −1- 0 eV represent the polaronic states located on titanium atoms. SOMO-1: the second singly occupied molecular orbital and the isosurface value is 9.59×10^{-9} (a.u.). The vertical dashed line represents the Fermi energy level which is set at 0 eV.

4.2.2.2 Reduced Rutile TiO_2 (110)

To compare the results with the reduced anatase TiO_2 (101) surface, we investigated the relative energetics of the top layer and sublayer oxygen vacancies of rutile TiO_2 (110) surface, which are extensively investigated both experimentally and theoretically. Our DFT+U calculations are carried out for an O_{2c} vacancy at the top layer of the slab (see Fig. 4-6) using a U value of 4.2 eV [104][105][106]. At the DFT-GGA level, the formation energies of oxygen vacancies at the top layer of the slab (see Fig. 4-6) are lower than those at the sublayer (see Fig. 4-5) approximately by 0.6 eV, which is in good agreement with previous theoretical calculations [149][150][151][152].

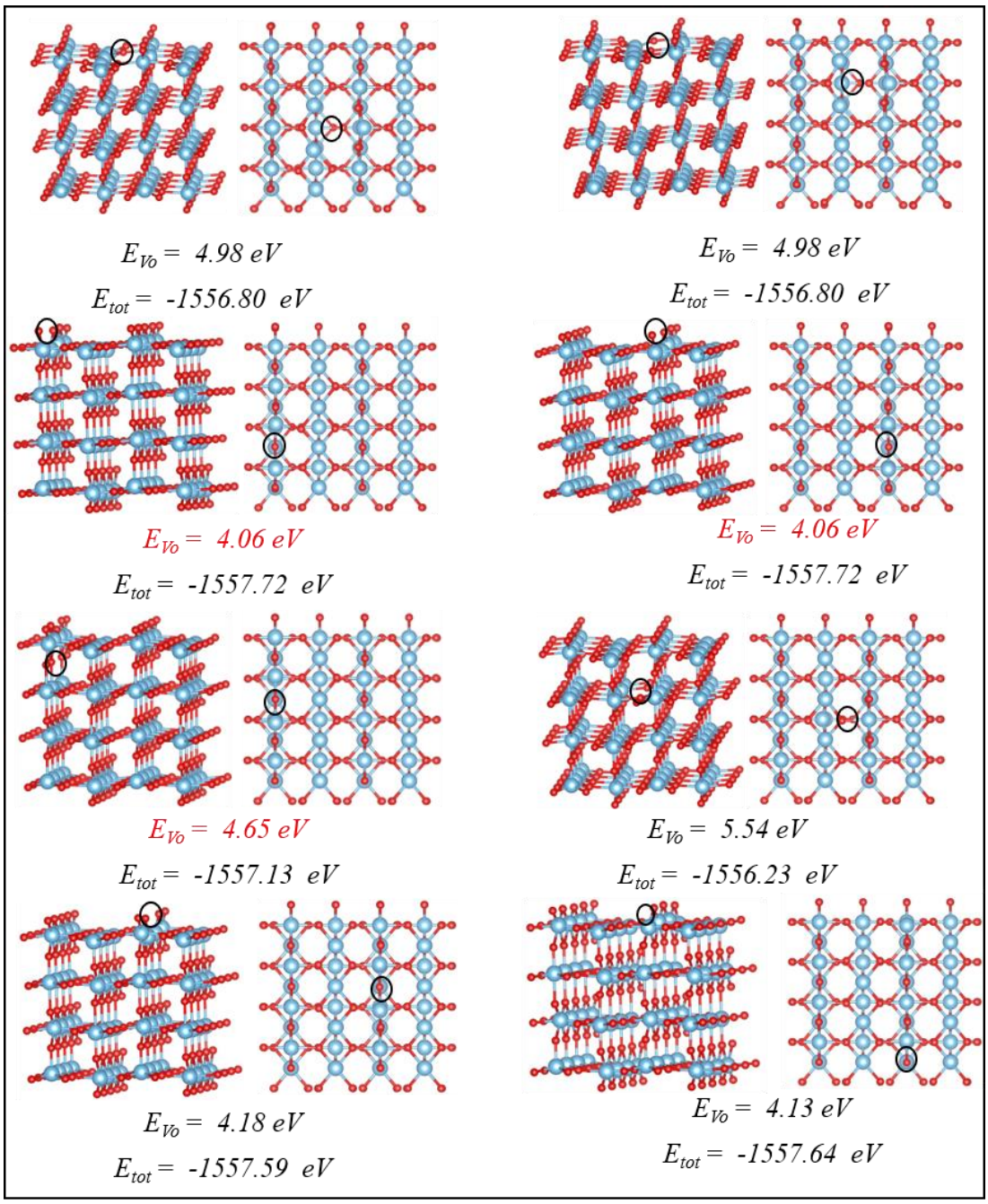

Fig. 4-5 Creation of an oxygen vacancy at surface and subsurface sites of anatase TiO_2 (101). The black circles indicate the oxygen vacancy site, the values in the first line represent the formation energy of oxygen vacancy, while the values in the second line represent the total energy of the system.

In all studied cases, the O_{2c} vacancy in the top layer creates two polaronic states localised at two Ti_{5c} in the top layer of the slab (see Fig. 4-6). As shown in the density of states in Fig. 4-6, the oxygen vacancy energy levels lie at 0.87 and 1.22 eV below the bottom of the conduction band. The energies of these gap states are in excellent agreement with electron energy loss spectroscopy (EELS) measurements [153]. To conclude, the formation of oxygen vacancy of the bridging oxygen (O_{2c}) at the top layer of the slab is favoured for rutile TiO_2 (110) surface.

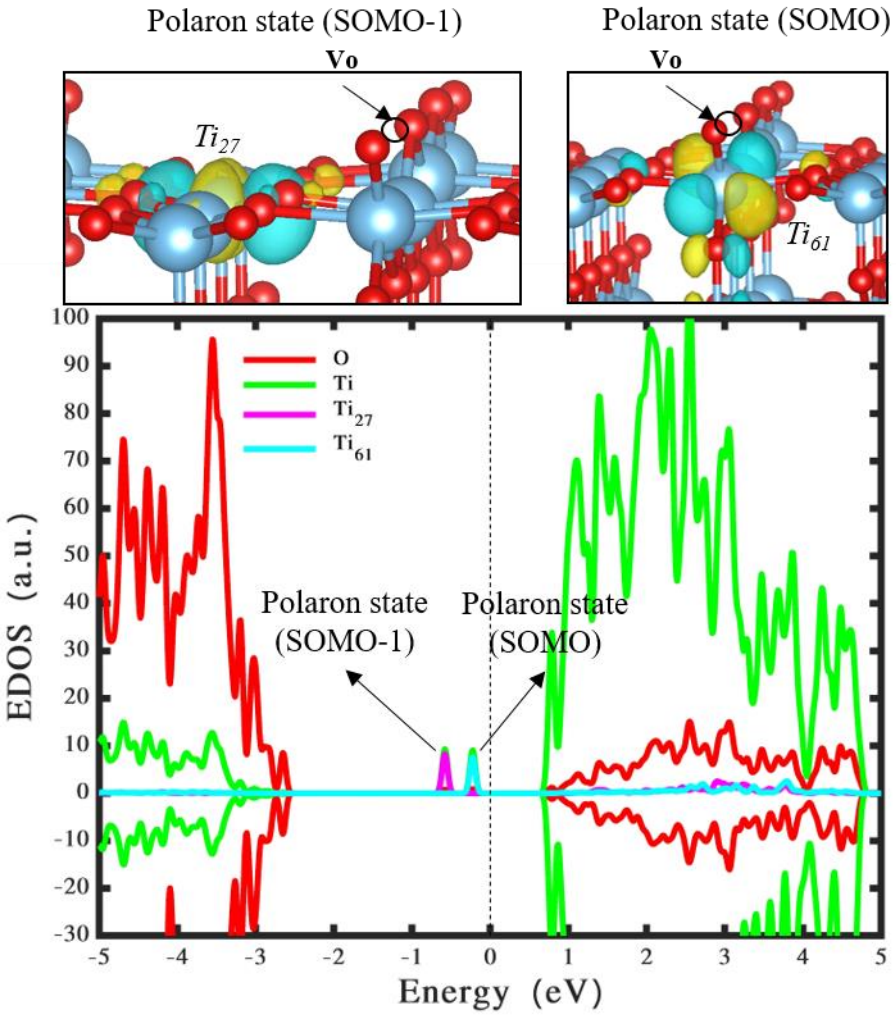

Fig. 4-6 Wavefunction and density of states of reduced rutile TiO_2 (110) surface. The green, red and blue show the states located on titanium, oxygen and silver atoms, while the pink and cyan peaks between −0.6- 0 eV

represent the polaronic states located on titanium atoms. The isosurface value is 9.83×10^{-8} (a.u.). The vertical dashed line represents the Fermi energy level which is set at 0 eV.

4.2.3 The Deposition of Trapezoidal and Bipyramidal Ag_5 on Anatase TiO_2(101)

4.2.3.1 On Pristine Anatase TiO_2(101)

Trapezoidal (see Fig. 4-7(a)) and bipyramidal (see Fig. 4-7(b)) Ag_5 clusters are deposited on anatase TiO_2 (101) surface with the corresponding wavefunctions as shown in Fig. Fig. 4-7. After geometrical optimisation, both silver clusters relax to a lying-down trapezoidal Ag_5, which is completely attached to the substrate surface. The trapezoidal Ag_5 cluster transfers 0.91 e^- to Ti atoms creating a delocalised state located just at the bottom of the conduction band edge. This higher energy level state is active and could play a key role in photocatalytical processes. In order to confirm this delocalised state, we performed a DFT + U calculation using a value of U = 2.5 eV (see Fig. 4-8). Similarly, the bipyramidal Ag_5 cluster transfers 0.89 e^- to a Ti^{3+} ($3d$) in the surface of anatase TiO_2 (101) leading to the formation of a polaron at 0.9 eV bellow the conduction band edge (see the pink peak at −0.23 eV). The polaronic state can be clearly seen by the wavefunction SOMO in Fig. 4-7, which is located just underneath the silver cluster. The

adsorption energy of Ag_5 cluster for the former is −2.88 eV and for the latter is −3.54 eV.

(a)

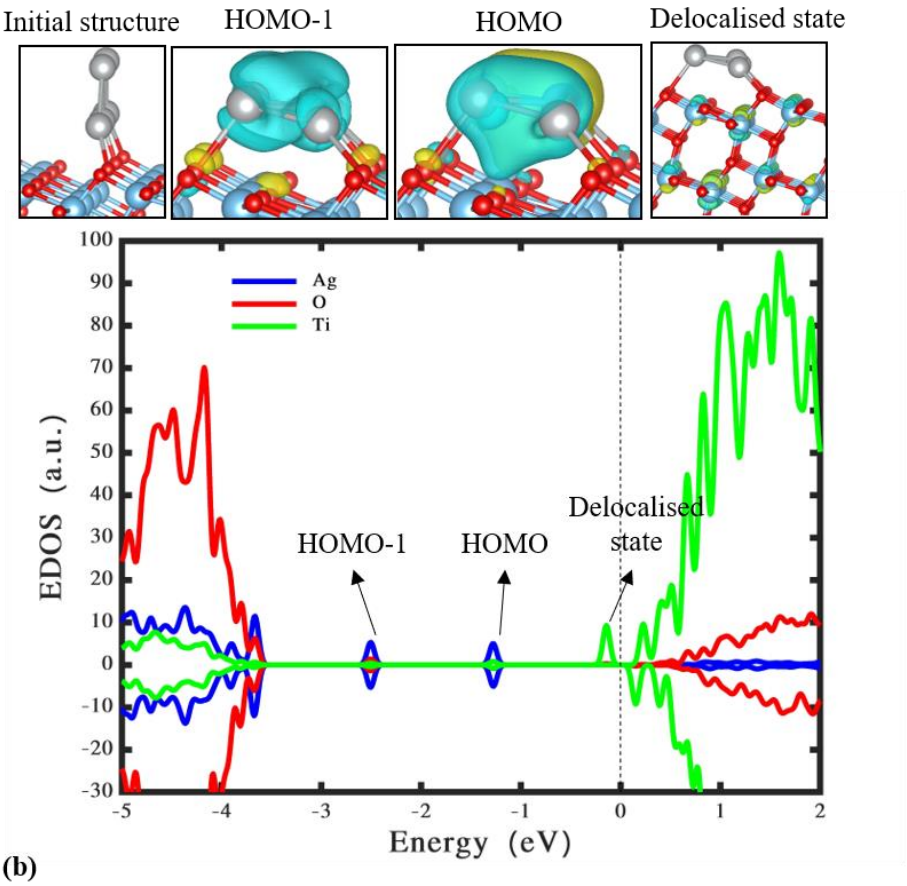
Initial structure
HOMO-1
HOMO
Delocalised state
Ag
O
Ti
EDOS (a.u.)
HOMO-1
HOMO
Delocalised state
Energy (eV)

(b)

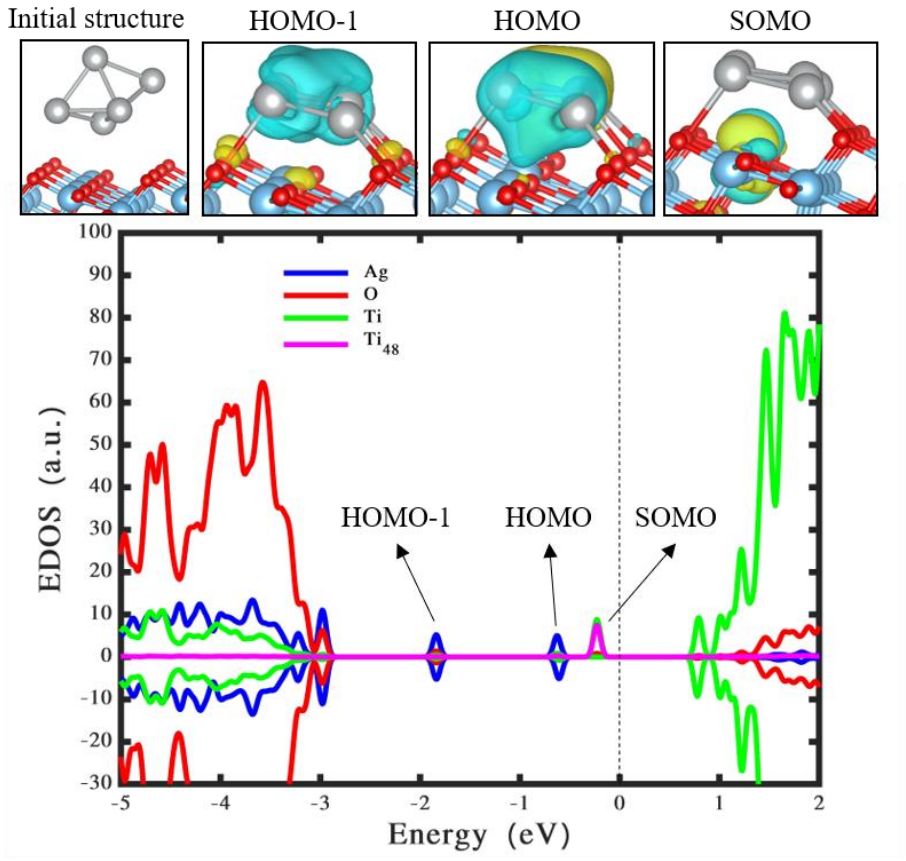
Initial structure
HOMO-1
HOMO
SOMO
Ag
O
Ti
Ti48
EDOS (a.u.)
HOMO-1
HOMO
SOMO
Energy (eV)

Fig. 4-7 Wavefunction and density of states of trapezoidal (a) and bipyramidal (b) Ag_5 clusters deposited on anatase TiO_2 (101) surface. The green, red and blue show the states located on titanium, oxygen and silver atoms, while the pink peak between −1- 0 eV represents the polaronic states located on a titanium atom. The isosurface value of (a) is 8.00×10^{-8} (a.u.), and (b) is 8.00×10^{-9} (a.u.). The vertical dashed line represents the Fermi energy level which is set at 0 eV.

The highest occupied molecular orbital (HOMO) of the Ag_5 cluster on an anatase TiO_2 (101) surface mixes stronger with Ti^{3+} (3*d*) states than the bridging oxygen atoms at −1.23 eV for the trapezoidal shape and at −0.63 eV for the bipyramidal shape. In contrast, the overlap of the second highest occupied molecular orbital (HOMO-1) of the Ag_5 cluster is stronger with O (2p) states of the bridging oxygen atoms than that the Ti^{+3} (3d) states at −2.6 eV for the trapezoidal shape and at −1.84 eV for the bipyramidal shape. Furthermore, fewer gap states are found in the mid-gap range between −3.0 eV and 0 eV unlike the gap states formed by a Cu_5 cluster reported in a previous DFT study [143]. These gap states can improve the photocatalytic efficiency of rutile and anatase TiO_2 material [154]. Based on the projected density of states, the Ag_5 cluster becomes nonmagnetic after donating an electron, while the support gains the electron and becomes paramagnetic with one unpaired electron (see Fig. 4-7(b)). This phenomenon was also observed for a Cu_5 cluster when deposited on a rutile TiO_2 (110) surface [143].

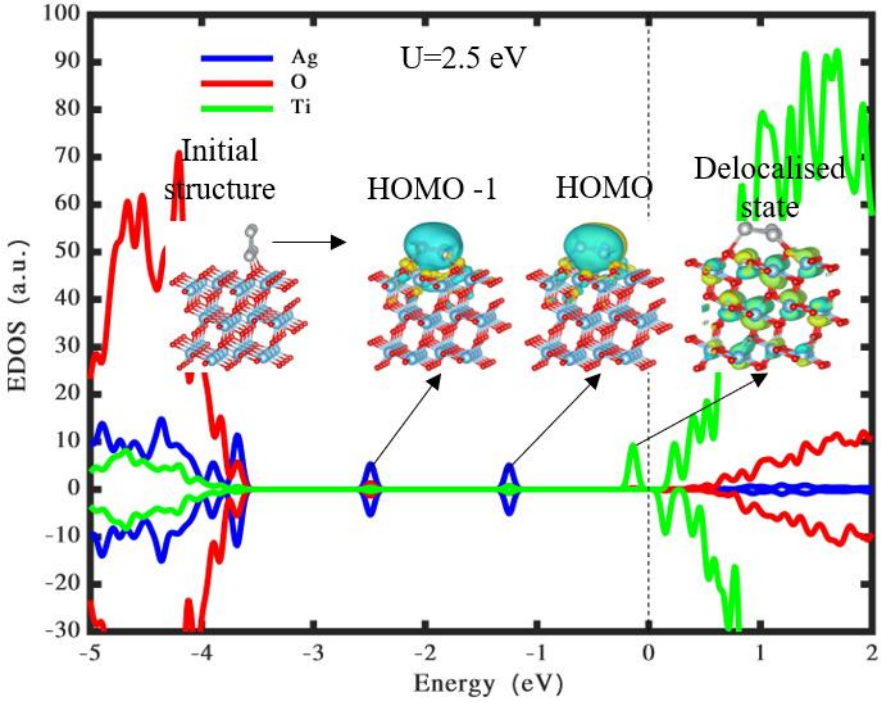

Fig. 4-8 Wavefunction and density of states of trapezoidal Ag_5 cluster deposited on anatase TiO_2 (101) surface using U = 2.5 eV. The green, red and blue show the states located on titanium, oxygen and silver atoms.

4.2.3.2 On Reduced Anatase TiO_2 (101)

Having analysed the electronic structure of Ag_5 clusters deposited on a pristine anatase TiO_2 (101) surface in the ground electronic state, we further investigated the electronic structure of Ag_5 clusters deposited on a reduced anatase TiO_2 (101) surface. Upon adsorption of an Ag_5 cluster, Ag_5 and an oxygen vacancy are able to induce three surface polarons demonstrated in Fig. 4-9. The trapezoidal Ag_5 cluster transfers 0.87 e^- to anatase TiO_2 (101) surface which is a 0.02 e^- lower charge transfer than the stoichiometric anatase TiO_2 (101) surface. The formation energy

of an oxygen vacancy in anatase $Ag_5@TiO_2$ (101) is 4.31 eV, which slightly increases by a factor of 0.05 eV as compared to the pristine anatase TiO_2 (101). Thus, it is concluded that the deposition of the Ag_5 cluster on anatase TiO_2 (101) does not affect the process in which an oxygen vacancy can occur. Further optimal configurations using different sites of oxygen vacancy can be found in Fig. 4-10.

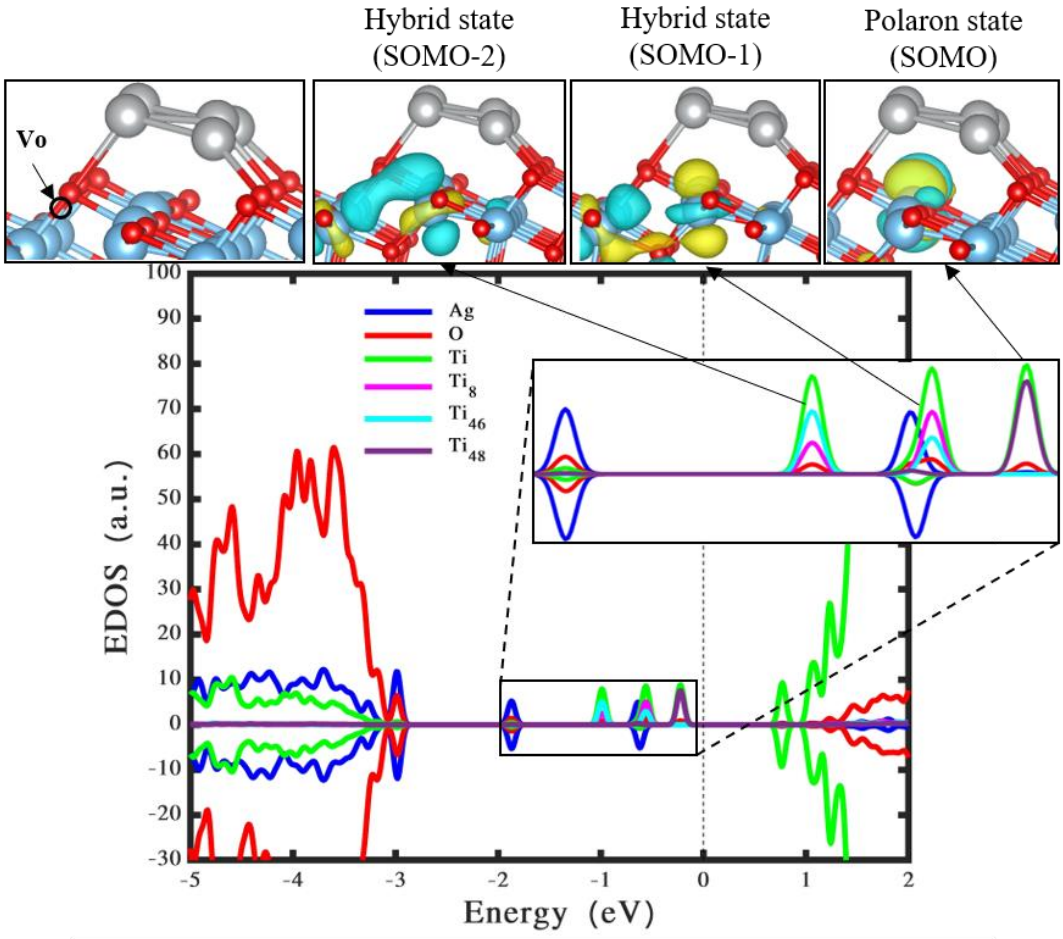

Fig. 4-9 Wavefunction and density of states of trapezoidal Ag_5 deposited on reduced anatase TiO_2 (101) surface. The green, red and blue show the states located on titanium, oxygen and silver atoms, while the pink, cyan and purple peaks between −1- 0 eV represent the polaronic states located on titanium atoms.

The isosurface value is 8.00×10^{-8} (a.u.). The vertical dashed line represents the Fermi energy level which is set at 0 eV.

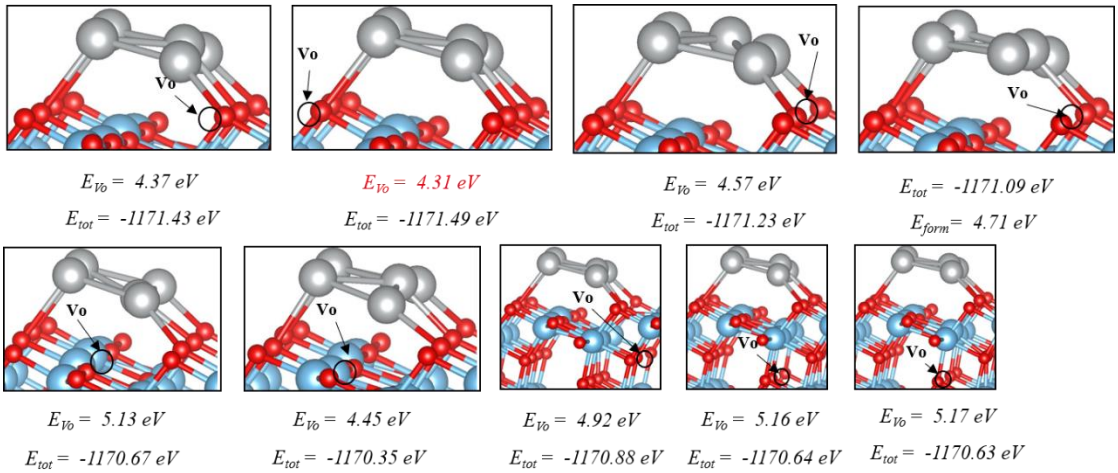

Fig. 4-10 Creation of an oxygen vacancy at surface and subsurface sites of anatase Ag_5@TiO_2 (101). The black circles indicate the oxygen vacancy site, the values in the first line represent the formation energy of oxygen vacancy, while the values in the second line represent the total energy of the complex.

4.2.4 The Deposition of Trapezoidal and Bipyramidal Ag_5 on Rutile TiO_2(110)

4.2.4.1 On Pristine Rutile TiO_2 (110)

Three adsorption configurations of Ag_5 clusters deposited on the rutile TiO_2 (110) surface are evaluated: the upstanding trapezoidal, tilted trapezoidal and bipyramidal Ag_5 clusters. The corresponding density of states and most relevant

frontier molecular are shown in Fig. 4-11. From Fig. 4-11(a), we can see that the trapezoidal shape of Ag_5 persists. However, when the trapezoidal Ag_5 cluster is tilted towards the TiO_2 surface (see Fig. 4-11(b)), it is drastically deformed to a new planar shape, which is more stable compared to the upstanding configuration by a 1.24 eV lower energy. In contrast, as clearly seen in Fig. 4-11(c), upon adsorption, the bipyramidal Ag_5 cluster is deformed to a new pyramidal configuration, which becomes the most stable structure differing by a 1.81 eV compared to the upstanding trapezoidal Ag_5 (see Fig. 4-11(a)).

As depicted in the projected density of states in Fig. 4-11, one polaron state forming the singly occupied molecular orbital (referred to as SOMO) is located on a Ti^{3+} (3*d*) in the sublayer of the substrate for the trapezoidal configurations and located on a Ti^{3+} (3*d*) in the top layer of the substrate for the bipyramidal configuration (represented by the pink peaks next to the wavefunction SOMO in Fig. 4-11). The SOMO shown in Fig. 4-11(a) has a lower energy level than the HOMO, and this has been also found in ref. [142] [29] [155] [156] [143]. Owing to the fact that the states formed by silver align mainly with the valence band, the existence of the polaronic state is crucial for absorbing photons in the visible light region [157]. Based on Bader charge analysis, the trapezoidal Ag_5 clusters shown in Fig. 4-11(a) and Fig. 4-11(b) are positively charged and transfer about 0.74 e^- and 0.94 e^- to the substrate, respectively. Additionally, the bipyramidal Ag_5 cluster presented in Fig. 4-11(c) is positively charged and donates approximately 0.89 e^- to the substrate creating the polaron at −0.3 eV, which is approximately 1.2 eV below the edge of the conduction band. The same value was obtained by Di

Valentin *et al.* for a Ti_{5c} (3*d*) state in reduced and hydroxylated rutile TiO_2 (110) [158].

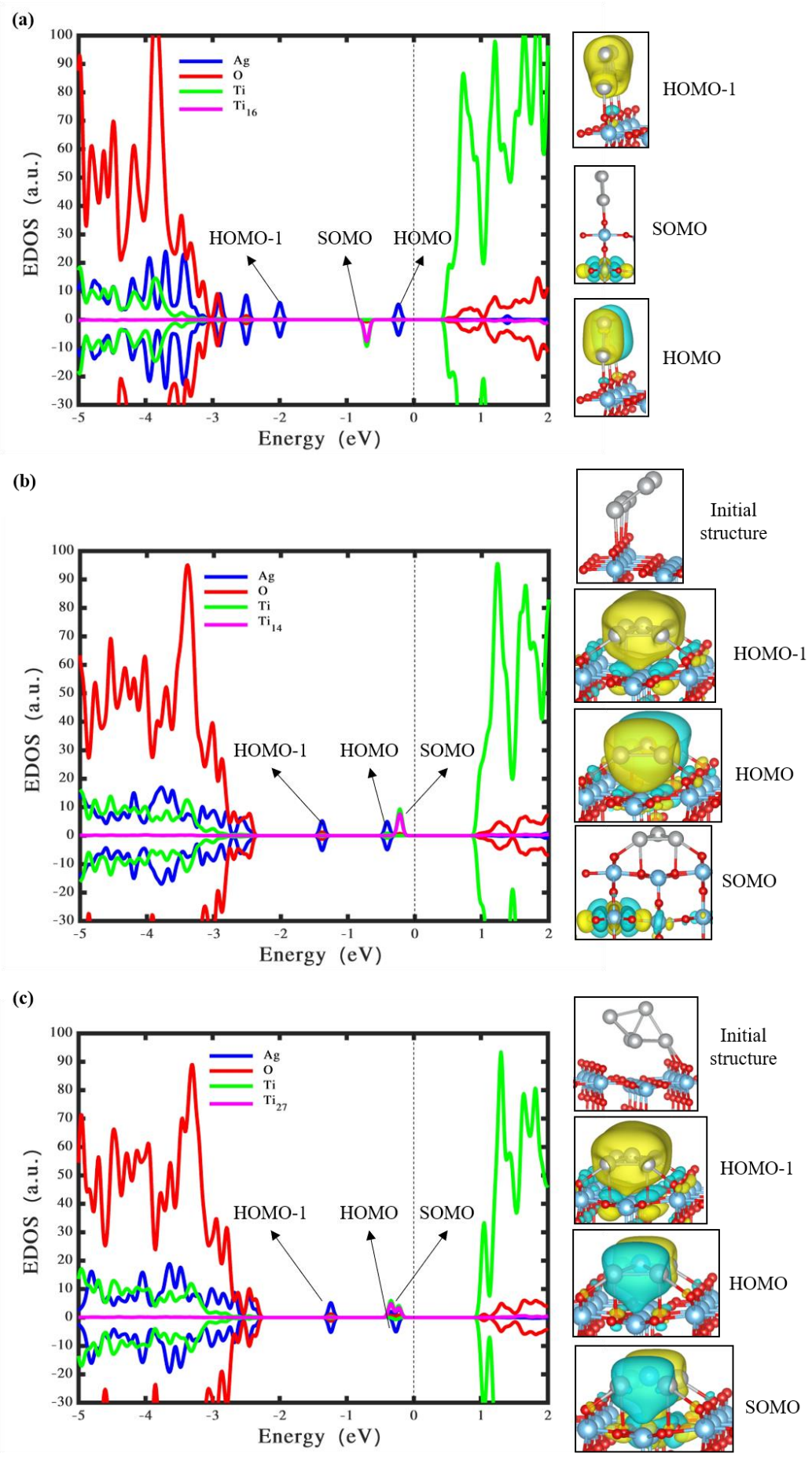
(a)
EDOS (a.u.)
Energy (eV)
Ag
O
Ti
Ti16
HOMO-1
SOMO
HOMO
HOMO-1
SOMO
HOMO
(b)
EDOS (a.u.)
Energy (eV)
Ag
O
Ti
Ti14
HOMO-1
HOMO
SOMO
Initial structure
HOMO-1
HOMO
SOMO
(c)
EDOS (a.u.)
Energy (eV)
Ag
O
Ti
Ti27
HOMO-1
HOMO
SOMO
Initial structure
HOMO-1
HOMO
SOMO

Fig. 4-11 Wavefunction and density of states of up-standing trapezoidal (a), tilted trapezoidal (b) and bipyramidal (c) Ag_5 clusters deposited on rutile TiO_2 (110) surface. The green, red and blue show the states located on titanium, oxygen and silver atoms, while the pink peaks between –1- 0 eV represent the polaronic states located on a titanium atom. The isosurface value is 4.61×10^{-8} (a.u.)._The vertical dashed line represents the Fermi energy level which is set at 0 eV.

4.2.4.2 On Reduced Rutile TiO_2 (110)

Based upon the optimised configurations illustrated in Fig. 4-11, we now study the effect of the presence of one oxygen vacancy. A similar trend to the reduced anatase TiO_2 (101) surface is observed for the reduced rutile TiO_2 (101), where both Ag_5 and an oxygen vacancy are able to induce three surface polarons as can be seen in Fig. 4-12 and Fig. 4-13. The deposition of an Ag_5 cluster and the presence of an oxygen vacancy reinforce each other and lead to the formation of three polaronic states, in which one is formed due to the charge transfer from Ag_5 cluster to the support and the other two are formed due to the presence of the oxygen vacancy for both cases. In particular, in the corresponding projected density of states, the localised Ti^{3+} ($3d$) orbitals (occupying the SOMOs) lie between 0.78 eV and 1.03 eV below the conduction band edge for the upstanding trapezoidal shape and between 0.92 eV and 1.13 eV below the conduction band edge for the new planar shape. These states will affect the dynamics of the photogenerated charges

[159] as well as decelerating the electron-hole pairs recombination resulting in improved catalytic activity.

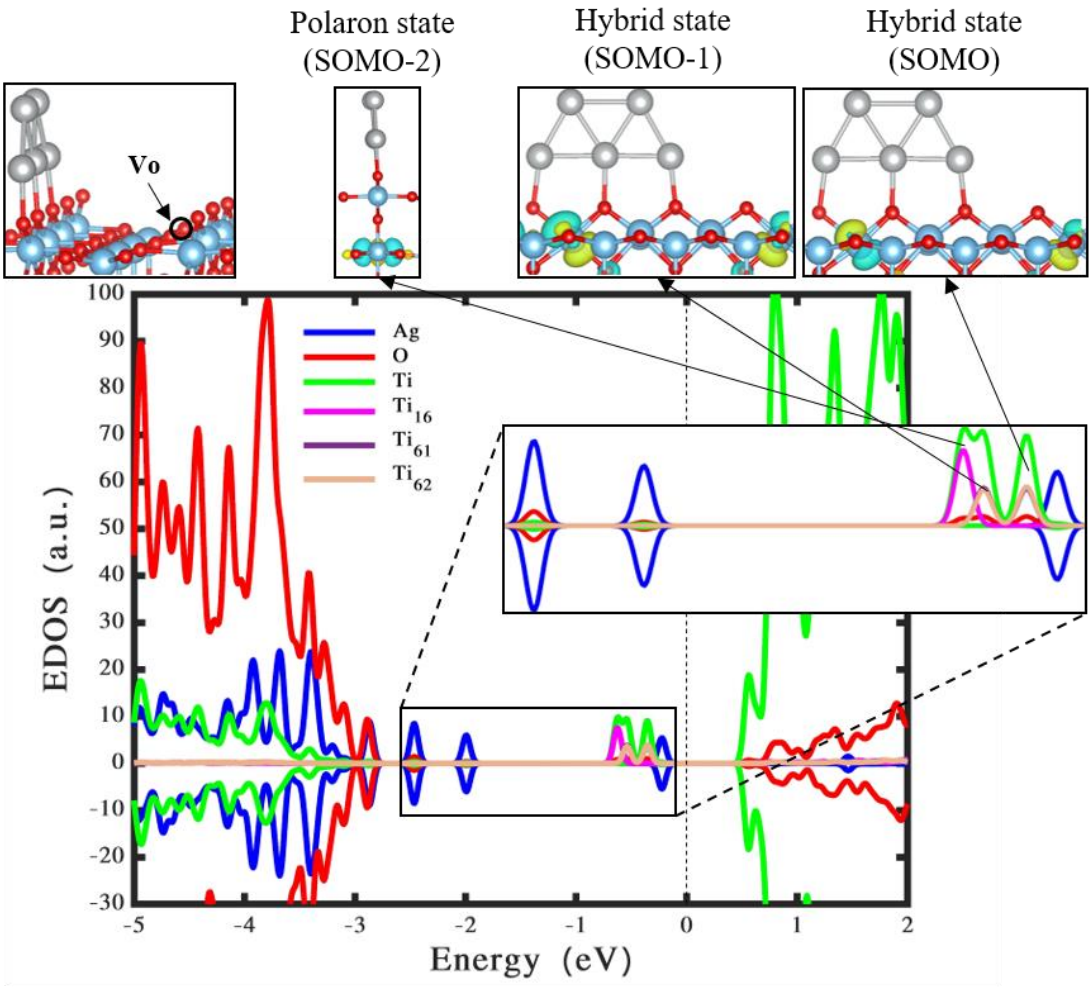

Fig. 4-12 Wavefunction and density of states of trapezoidal Ag_5 deposited on reduced rutile TiO_2 (110) surface. The green, red and blue show the states located on titanium, oxygen and silver atoms, while the pink, brown and purple peaks between −1- 0 eV represent the polaronic states located on

titanium atoms. The isosurface value is 1.00×10⁻⁷ (a.u.). The vertical dashed line represents the Fermi energy level which is set at 0 eV.

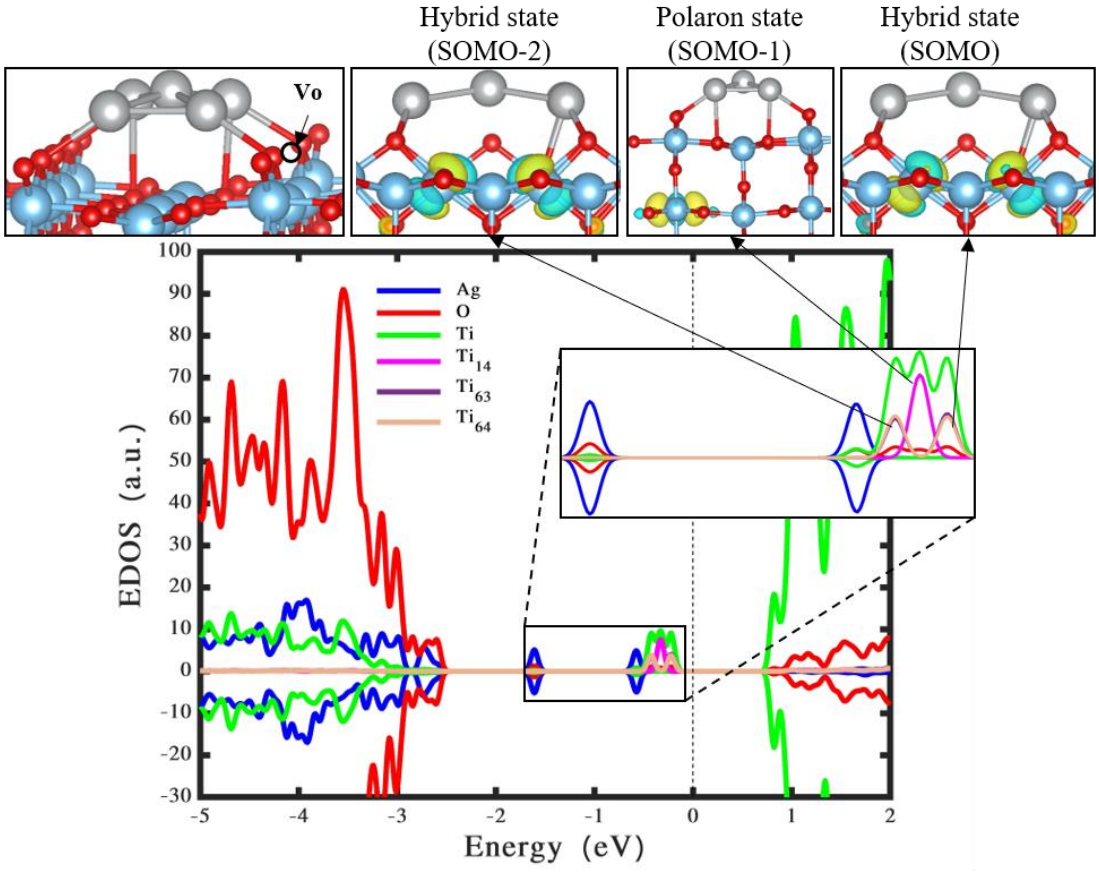

Fig. 4-13 Wavefunction and density of states of new planar Ag_5 deposited on reduced rutile TiO_2 (110) surface. The green, red and blue show the states located on titanium, oxygen and silver atoms, while the pink, brown and purple peaks between −1- 0 eV represent the polaronic states located on titanium atoms. The isosurface value is 1.00×10⁻⁷ (a.u.). The vertical dashed line represents the Fermi energy level which is set at 0 eV.

In addition, it is found that the amount of charge transfer from the Ag_5 cluster to the support is slightly less, as compared to the stoichiometric rutile TiO_2 (110)

surface. For example, the up-standing trapezoidal Ag_5 cluster donates 0.73 e^- to the reduced rutile TiO_2 (110) surface, which is a 0.01 e^- less charge transfer than the stoichiometric surface. This could be attributed to the presence of the oxygen vacancy, where the charge distributes to a lesser extent than on defective TiO_2 surfaces [142]. The formation energy of an oxygen vacancy in rutile Ag_5-TiO_2 (110) is 4.44 eV for the upstanding configuration (see Fig. 4-12) and is 4.47 eV for the new planar configuration (see Fig. 4-13). It is worth mentioning that upon the deposition of the Ag_5 cluster on rutile TiO_2 (110), the formation energy of an oxygen vacancy in the case of the upstanding configuration increases approximately 0.38 eV and in the case of the new planar configuration raises 0.41 eV as compared to pristine rutile TiO_2 (110). This indicates that depositing small silver AQCs can further stabilise the rutile TiO_2 (110) surface. Further optimal configurations using different sites of oxygen vacancy can be found in Fig. 4-14 and Fig. 4-15.

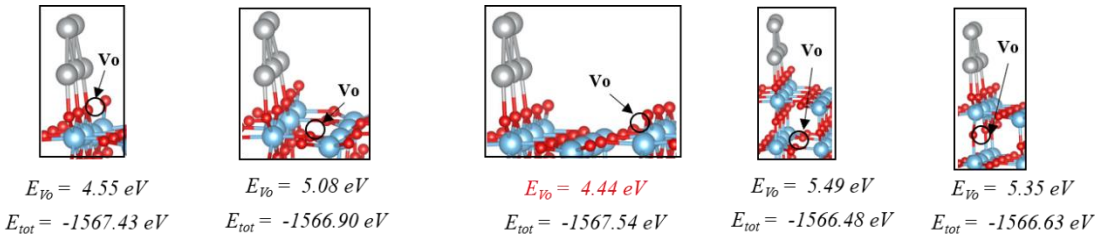

Fig. 4-14 Creation of an oxygen vacancy at surface and subsurface sites of rutile Ag_5(trapezoidal)-TiO_2 (110). The black circles indicate the oxygen vacancy site, the values in the first line represent the formation energy of

oxygen vacancy, while the values in the second line represent the total energy of the complex.

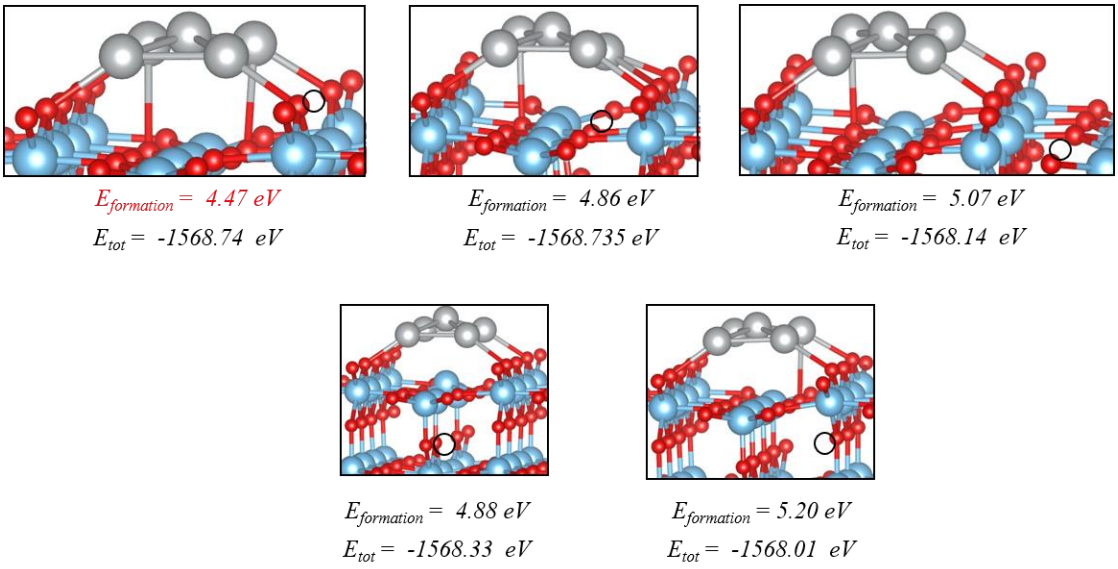

Fig. 4-15 Creation of an oxygen vacancy at surface and subsurface sites of rutile Ag_5(new planar)-TiO_2 (110). The black circles indicate the oxygen vacancy site, the values in the first line represent the formation energy of oxygen vacancy, while the values in the second line represent the total energy of the complex.

4.3 Conclusion

We have systematically studied the stability of trapezoidal and bipyramidal Ag_5 AQCs in the gas phase and demonstrated that the trapezoidal Ag_5 AQC is more stable than the bipyramidal Ag_5 AQC. We have also studied the electronic structures of Ag_5 AQCs deposited on both anatase TiO_2 (101) and rutile TiO_2 (110) surfaces with and without the presence of an oxygen vacancy and have shown that

mid-gap states are formed due to the adsorption of Ag_5 AQCs and the presence of oxygen vacancies. Both the trapezoidal and bipyramidal Ag_5 AQCs create only one polaronic state in both TiO_2 surfaces either on the top layer or on the first sublayer. Two more polaronic states are created, when introducing an oxygen vacancy into Ag_5@TiO_2 complex of both surfaces. Importantly, the polarons and other gap states persist, which reveals that Ag_5 and oxygen vacancies can reinforce each other. Moreover, the creation of an oxygen vacancy requires less energy for the Ag_5@ anatase TiO_2 (101) complex as compared to the Ag_5@ rutile TiO_2 (110) complex. Distortion of Ag_5 AQCs have been clearly demonstrated when adsorbed on both TiO_2 surfaces. Upon surface adsorption, both bipyramidal and trapezoidal Ag_5 AQCs are oxidised, donating their electrons to the substrates of all the modelled structures. The highest net charge is correlated with the highest adsorption energies obtained. It has also been demonstrated that deposited Ag_5 AQCs and the created oxygen vacancy on photocatalyst surface of both titania surfaces can efficiently separate the electron-hole pairs and therefore, could enhance their photocatalytic activity. The theoretical findings presented in this chapter shed light on new strategies for improving the photocatalytic efficiency of such systems.

5 Ag_5 Deposited on CeO_2 (111) surface

This chapter presents the investigations of Ag_5 AQCs adsorbed on a perfect and reduced CeO_2 (111) surface to gain an understanding of cluster-based photocatalysts toward water splitting. It also presents the effect of the purification process using Ag_2/SiO_3 on electronic structures of $Ag_5@CeO_2$ modelled systems using DFT+U calculations. The trapezoidal $Ag_5@CeO_2$ (111) system is found to be more stable than the bipyramidal $Ag_5@CeO_2$ (111) system. Furthermore, the formation energy of an oxygen vacancy is significantly reduced by introducing Ag_5 AQC. With respect to the purification process, it is found that the presence of silicate (SiO_3^{2-}) affected the gap states of CeO_2. However, they are physically located away from its surface.

5.1 Introduction

Ceria has been widely investigated, because of its desirable properties, especially in photocatalytic applications. Most studies have concentrated on the adsorption of a single atom and metal clusters on ceria (111) surface or on the interactions of the water molecule with the ceria (111). For instance, the interaction of single

atoms like Pt [160], Sn [161], Au [162][163], and Ag [164][165][166] on a perfect and reduced ceria (111) has been studied experimentally and theoretically. Generally, it has been found that the adsorption of these metal atoms on the ceria (111) surface leads to charge transfer from the metal atoms to the oxide surface, resulting in the reduction of Ce^{4+} ions on the surface to Ce^{3+} ions. For example, Bruix *et al*. [160] implemented DFT+U calculations using both LDA and GGA correlation functionals to study the adsorption of Pt on a perfect ceria (111) surface. It was revealed that Pt is oxidised to Pt^{+} and a Ce^{4+} ion is reduced to Ce^{3+} and becomes the most energetically favourable configuration. It was also shown that the most favourable geometry correlated to the adsorption of Pt on the bridging oxygen atoms at the oxide surface.

Furthermore, Farmer *et al*. [167] used microcalorimetry to study the adsorption of silver on ceria (111). It is found that the metal is adsorbed more strongly on the reduced ceria (111) surface due to the presence of oxygen vacancies. Saravanakumar *et al*. [168] successfully synthesised $Ag@CeO_2$ nanocomposite photocatalysts using a hydrothermal technique. It is found that the photocatalytic activity of $Ag@CeO_2$ is improved as compared to pristine CeO_2 due to lower charge carriers' recombination. This photocatalytic enhancement can be ascribed to the surface plasmon resonance effect of silver nanoparticles. Furthermore, Preda *et al.* [166] computationally studied the role of the silver cluster in modifying the properties of a pure and defective CeO_2 (111) by applying a DFT+U using both LDA and GGA correlation functionals. It is found that the silver atoms are oxidised,

donating their valence electrons to the substrate, which results in the formation of reduced Ce^{3+} ions.

This chapter aims to investigate the geometries and electronic structures of Ag_5 AQCs on a perfect and reduced CeO_2 (111) surface. In addition, the effect of Ag_2SiO_3 adsorption on the stability of the perfect and reduced $Ag_5@CeO_2$ (111) is also investigated to obtain a clear understanding of the purification process of Ag_5 AQCs. The most energetically and geometrically favourable configurations of Ag_5 AQCs and $Ag_2SiO_3@Ag_5$ on a perfect and reduced CeO_2 (111) surface are computed using the GGA+U followed by calculations of electronic structures using HSE06 exchange-correlation functionals.

5.2 Results and Discussion

5.2.1 Perfect and Reduced CeO_2 (111)

To gain insights into the electronic structure of a perfect CeO_2 (111) surface and localisation of excess electrons in a reduced CeO_2 (111), we first built a three-layer slab model as a benchmark, which can be seen in Fig. 5-1(a) and Fig. 5-1(b). As deduced from the corresponding density of states of the perfect CeO_2 (111) (see Fig. 5-1(c)), the valence band is predominantly composed of O (2*p*) orbitals, and it

is isolated by a band gap (using the hybrid functionals HSE06) of approximately 3 eV from the conduction band that arises from the Ce (4*f*) levels. This band gap value is consistent with the measured value reported by Wuilloud *et al*. [54].

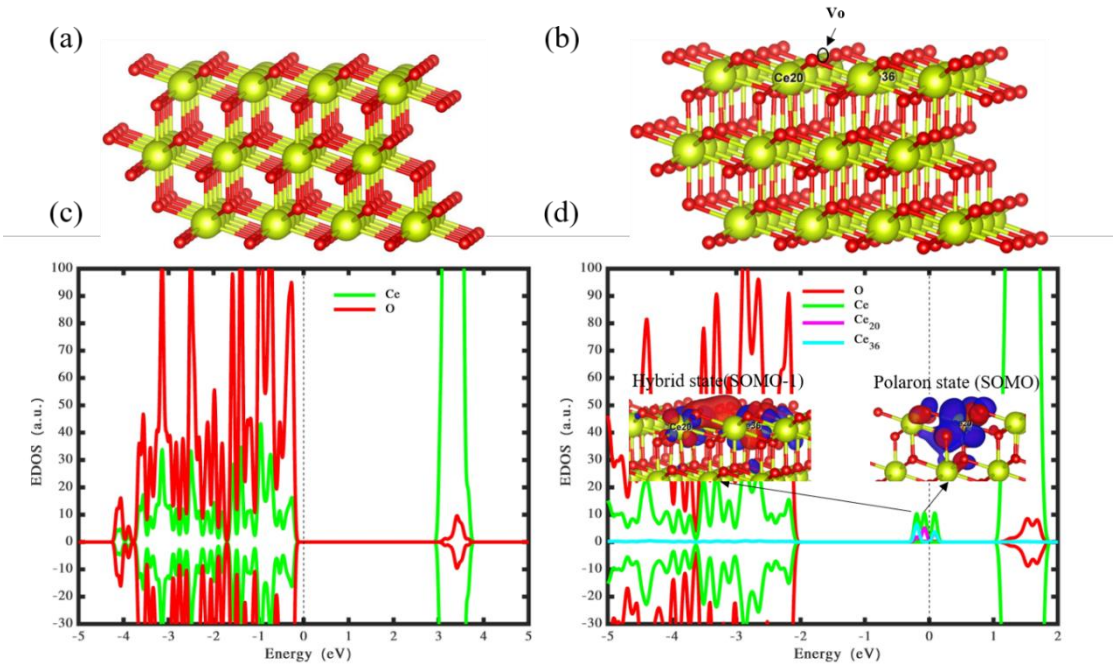

Fig. 5-1 Side view of optimised structures of perfect (a) and reduced (b) CeO_2 (111) surfaces. Green and red balls represent cerium and oxygen atoms, respectively. The density of states shown in (c) corresponds to the perfect CeO_2 (111), while the density of states and wavefunction presented in (d) correspond to the reduced CeO_2 (111). The green, red, pink, and cyan show the states located on cerium and oxygen, while the pink and cyan peaks between −0.2- 0 eV represent the polaronic states located on Ce^{3+} ions.

The formation of a single oxygen vacancy leads to a reduction in the CeO_2 system. Therefore, two excess electrons are found in localised Ce (4*f*) orbitals located on

two Ce ions, resulting in a modification in their atomic configurations from Ce^{4+} ($4f^0$) to Ce^{3+} ($4f^1$) [54]. This alteration in the atomic configurations is associated with the existence of the gap states of the reduced Ce^{3+} ions. To get further insight into the changes in the electronic structure of the reduced CeO_2 (111), its corresponding density of states and wavefunction plots are depicted in Fig. 5-1(d). It can be clearly seen that two peaks are located just below the Fermi energy level (indicated by pink and cyan colour) which are approximately 1.7 eV above the valence band. The wavefunction plot, for example, represents an unpaired electron on two certain Ce atoms, where both (Ce20) and (Ce36) are located on the top layer and are next to the oxygen vacancy. Different sites of an oxygen vacancy formed in CeO_2 (111) are presented in Fig. 5-2. The formation energy of an oxygen vacancy in the surface of CeO_2 (111) (see Fig. 5-2(a)) is slightly higher of approximately 0.09 eV in energy, than that of the subsurface (see Fig. 5-2(b)). The structure shown in Fig. 5-2(c) has high formation energy (E_{vo} = 2.71 eV) as compared to those shown in Fig. 5-2(a) and Fig. 5-2(b) when an oxygen atom is removed from the third row of oxygen atoms in CeO_2.

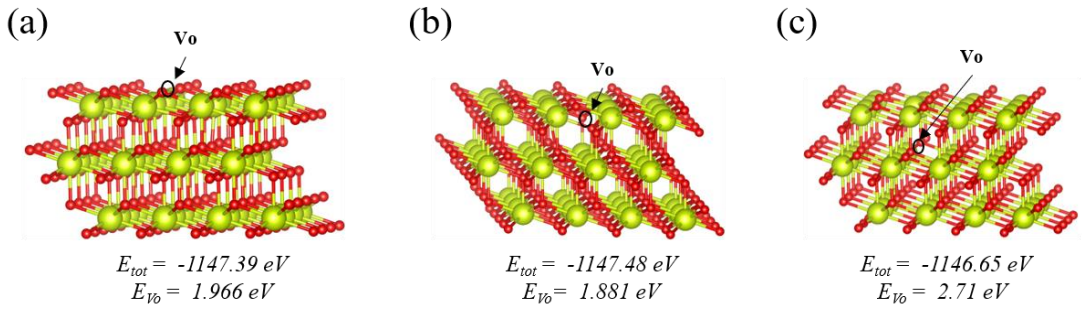

Fig. 5-2 Formation of an oxygen vacancy at surface and subsurface sites of CeO_2 (111). The green and red balls represent cerium and oxygen atoms, respectively. The black circles indicate the oxygen vacancy site, the values in the first line represent the total energy of the system, while the values in the second line represent the formation energy of oxygen vacancy.

5.2.2 The Deposition of Trapezoidal and Bipyramidal Ag_5 on CeO_2(111) Surface

5.2.2.1 On Perfect CeO_2 (111)

Two model systems are considered, i.e., trapezoidal and bipyramidal Ag_5 AQCs, to investigate their interactions with the perfect and reduced CeO_2 (111). The study of these model systems could provide information on the role of the Ag_5@CeO_2 interface in promoting photocatalytic activity for water splitting. Fig. 5-3 illustrates the most stable (Fig. 5-3(b)) and the meta-stable state (Fig. 5-3(d)) of bipyramidal Ag_5 deposited on CeO_2 (111). The deformation of the Ag_5 cluster (Fig. 5-3(b)) can be clearly observed, where one of the equatorial Ag atoms in the

cluster moves toward the oxide surface and creates a bond with an oxygen atom. This distortion leads to a reduction in the total energy as compared to the undeformed Ag_5 cluster (Fig. 5-3(d)), where it retains its initial structure (Fig. 5-3(c)) with an energy difference of approximately 0.14 eV. Table 5- 1 presents the total, adsorption energies and the total charge Ag_5 AQCs after depositing on the support surface.

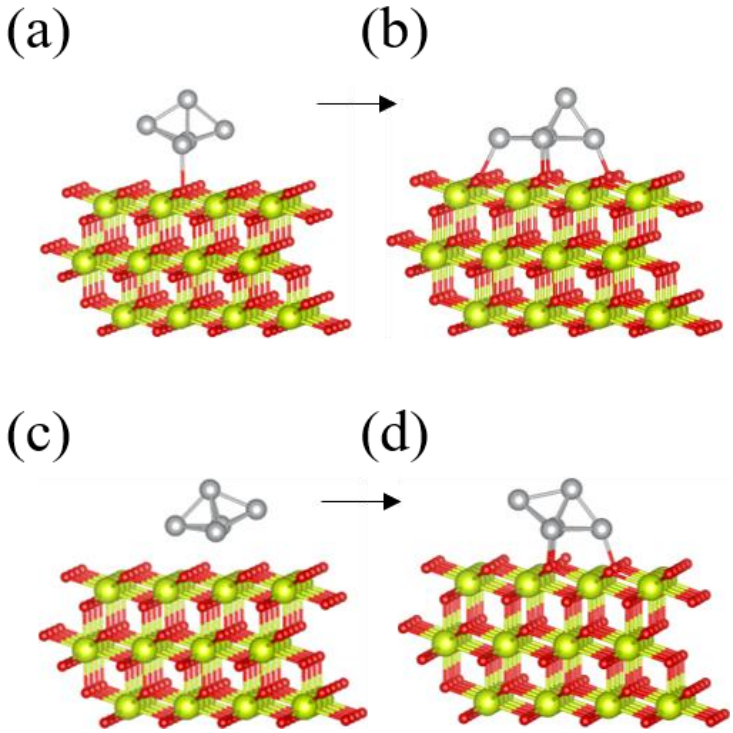

Fig. 5-3 (a) Initial and (b) optimised structures of the most stable bipyramidal Ag_5 deposited on CeO_2 (111), (c) and (d) Initial and optimised structures of the meta stable structures of bipyramidal Ag_5 deposited on CeO_2 (111). The green, red, and grey balls represent cerium, oxygen, and silver atoms, respectively.

Table 5- 1 Total, adsorption energies and cluster total charge of the most stable and metastable bipyramidal $Ag_5@CeO_2$.

Configuration	Total energy (eV)	Adsorption energy (eV)	Q_{Ag5} (e^-)
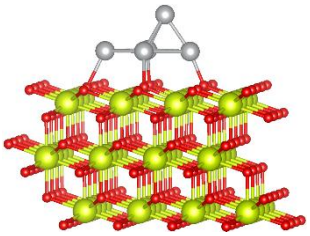	−1166.11	−4.66	0.59
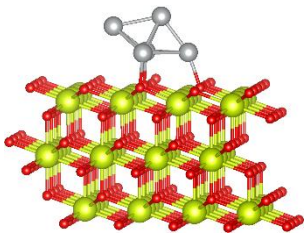	−1165.97	−4.52	0.54

Based on Bader charge distributions, both Ag_5 AQCs are oxidised and transfer approximately ~0.5 e^- to the support, thereby reducing it. This charge transfer is demonstrated by the Bader charge analysis and the wavefunction plots shown in Fig. 5-4(a) and Fig. 5-4(b), where an unpaired electron is localised on the 4*f* orbitals of a specific Ce ion. This result is in line with previous studies; for example, experiments and theories have revealed that the deposition of silver particles on the CeO_2 (111) surface reduces the oxide, and this is due to the charge transfer from the silver atoms to the support [169][170][171][165]. Similar situations have also been reported upon the adsorption of Pt, Au, and Pd particles on CeO_2 [172][173][174][175]. Fig. 5-4(a) and Fig. 5-4(b) display the wavefunctions and

density of states of the most stable (i.e., deformed cluster) and metastable (i.e., undeformed cluster) $Ag_5@CeO_2$. Comparable results are obtained for both cases, where a single surface polaron is formed due to the loss of charge of the Ag_5 cluster, which is gained by the support. In particular, the polaronic states represented by the pink peaks in Fig. 5-4(a) and Fig. 5-4(b), as well as by the wavefunctions (SOMOs) are located at ~0.8 eV below the edge of the conduction band. These peaks could contribute to the absorption of sunlight. Again the SOMOs shown in Fig. 5-4(a) and Fig. 5-4(b) have lower energy levels than the HOMOs, and this has been also found in ref. [142] [29] [155] [156] [143].

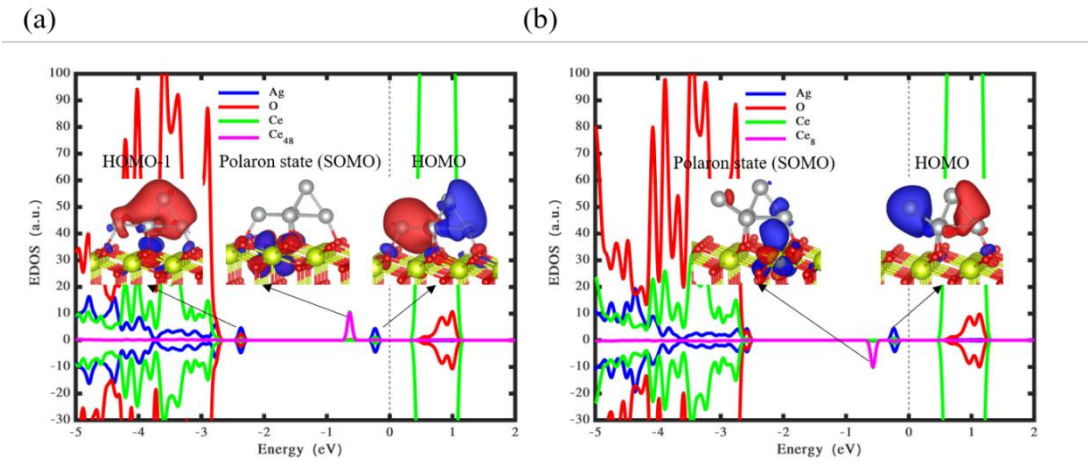

Fig. 5-4 Wavefunction and density of states of the stable (a) and meta stable (b) Ag_5 clusters deposited on CeO_2 (111) surface. The green, red and blue show the states located on cerium, oxygen and silver atoms, while the pink peak between −1- 0 eV represents the polaronic states located on a Ce ion.

After analysing the bipyramidal $Ag_5@CeO_2$, we now study the interaction of trapezoidal Ag_5 AQCs with the ceria (111) surface and how it may improve the photocatalytic process. Herein we simulate two model systems of trapezoidal Ag_5 AQCs deposited on the CeO_2 (111) surface. For example, the cluster shown in Fig. 5-5(a) is initially titled towards the oxide surface, and then after geometrical optimisation (Fig. 5-5(b)), it moves slightly backward and becomes nearly perpendicular to the oxide surface. On the contrary, the cluster presented in Fig. 5-5(c) is initially deposited parallel to the oxide surface, and then after geometrical optimisation (Fig. 5-5(d)), all cluster atoms bond to oxygen atoms on the surface, making the cluster highly adsorbed on the oxide surface with an adsorption energy of −4.68 eV., whereas the adsorption energy of the upstanding cluster is −3.29 eV. When the adsorption of both clusters takes place, no significant deformation is observed. Table 5-2 represents the total, adsorption energies and cluster total charge of configurations shown in Fig. 5-5(b) and Fig. 5-5(d).

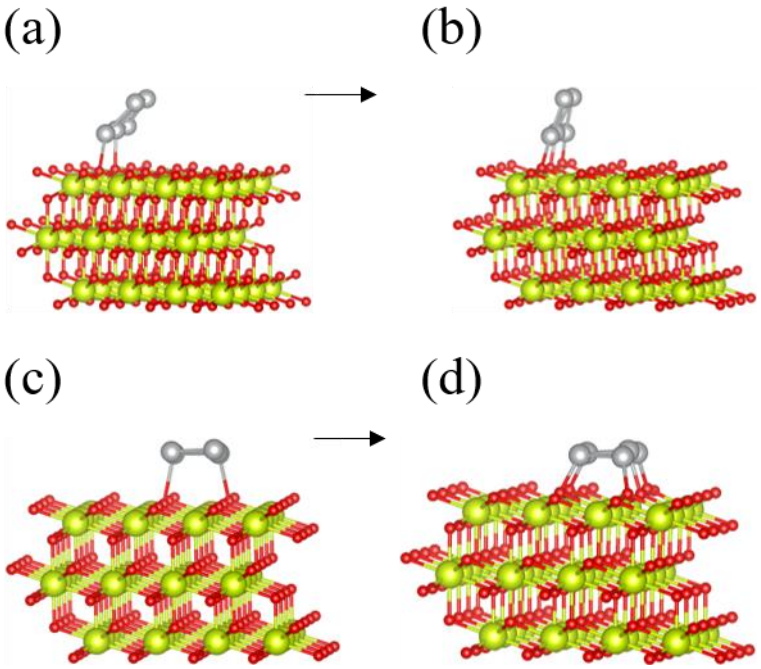

Fig. 5-5 (a) and (b) Initial and optimised structures of upstanding Ag_5 deposited on CeO_2 (111), (c) and (d) Initial and optimised structures of the most stable structures of lying-down trapezoidal Ag_5 deposited on CeO_2 (111).

Table 5-2 Total, adsorption energies and cluster total charge of the upstanding and lying-down trapezoidal Ag_5@CeO_2.

Configuration	Total energy (eV)	Adsorption energy (eV)	Q_{Ag5} (e^-)
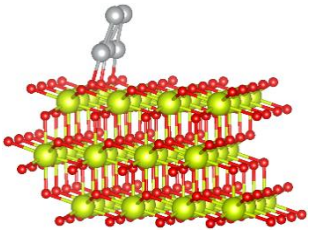	−1165.23	−3.29	0.51

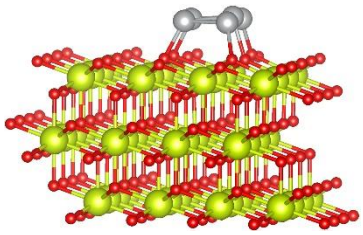	−1166.62	−4.68	1.00

Now, the electronic structures of both configurations shown in Fig. 5-5 are analysed via their density of states and wavefunctions, as depicted in Fig. 5-6. According to the analysis of the Bader charge distribution, the upstanding cluster transfers approximately 0.51 e^- to the support leading to the formation of a single polaron, which is gained by a Ce ion located at the lowest layer of the support (see the wavefunction SOMO in Fig. 5-6(a)). It is interesting to indicate that this polaron has a high energy level, which is located just 0.1 eV below the conduction band edge (indicated by the pink peak in Fig. 5-6(a)). This specific gap state is crucial in absorbing photons at low energy. On the other hand, the lying-down cluster transfers a double charge of the upstanding cluster, forming two polarons located on the top layer of the support (see SOMO and SOMO-1 in Fig. 5-6(b)). These polarons are also critical in improving the photocatalytic activity of the ceria (111) surface.

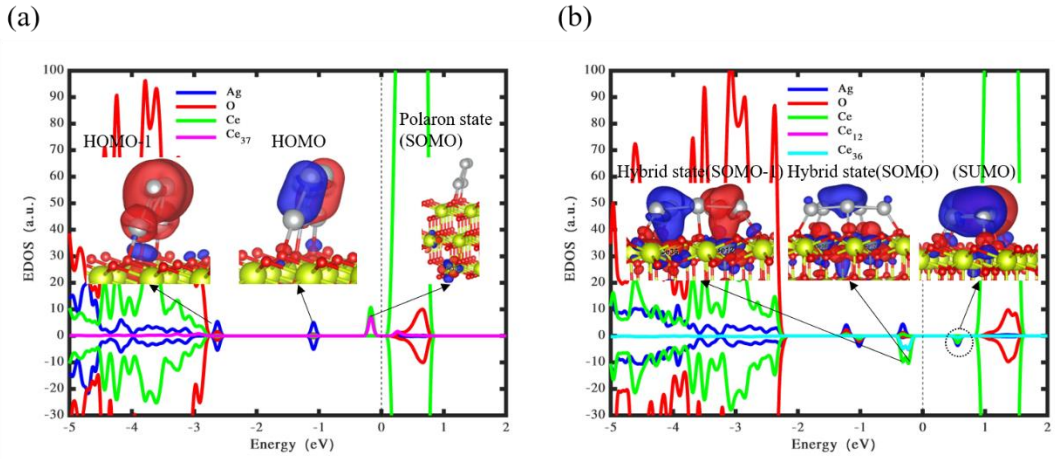

Fig. 5-6 Wavefunction and density of states of the upstanding (a) and lying-down (b) trapezoidal Ag_5 clusters deposited on CeO_2 (111) surface. The green, red, and blue show the states located on cerium, oxygen and silver atoms, while the pink and cyan peaks between −1- 0 eV represent the polaronic states located on Ce ions.

In addition to this, we also notice another interesting feature for the lying-down configuration, that is the appearance of a tiny peak (indicated by the wavefunction SUMO in Fig. 5-6(b)) at ~0.14 eV below the bottom of the conduction band, which is shared by silver and cerium atoms. Similar results were also reported when Ag_{10} clusters were deposited on a CeO_2 (111) surface [176], as well as when Cu/O_2 was deposited on a rutile TiO_2 (110) surface [143]. This small state can further improve the photocatalytic efficiency of the oxide. To conclude this section and based on our hybrid calculations, it is worth mentioning that the adsorption of the lying-down trapezoidal Ag_5 AQC on CeO_2 (111) is an energetically favourable process compared to the bipyramidal isomer. In contrast, bipyramidal clusters are more

thermodynamically stable than trapezoidal clusters when adsorbed on a rutile TiO_2 (110) surface.

5.2.2.2 On Reduced CeO_2 (111)

In the previous section, we systematically studied the adsorption mechanism of both types of Ag_5 clusters on CeO_2 (111). We now investigate the effect of the deposition of the most stable bipyramidal and trapezoidal Ag_5 AQCs (presented in **Section 5.2.2.1**) on electronic structures of defective CeO_2 (111). Fig. 5-7 shows the wavefunctions and density of states of a single surface oxygen vacancy modelled on the deformed bipyramidal Ag_5@reduced CeO_2. It is found that upon adsorption of Ag_5 cluster, the formation energy of an oxygen vacancy is significantly reduced to 1.01 eV compared with pristine CeO_2 (111). It can be clearly seen from Fig. 5-7 that there exists a total of four Ce^{3+} ions; two ions are due to charge transfer from the Ag_5 AQC, and the other two ions are correlated to the formation of an oxygen vacancy. Indeed, this is confirmed by the Bader charge distribution of the Ag_5 AQC (1.02 e^-). This is indeed a double charge transfer as compared to the bipyramidal Ag_5 AQC when deposited on the perfect CeO_2 (111). It can also be observed that a small state appears below the conduction band edge. This state, besides the polarons, could support the material to absorb photons in the visible light region. Other optimal structures using different sites of oxygen vacancy are presented in Fig. 5-8.

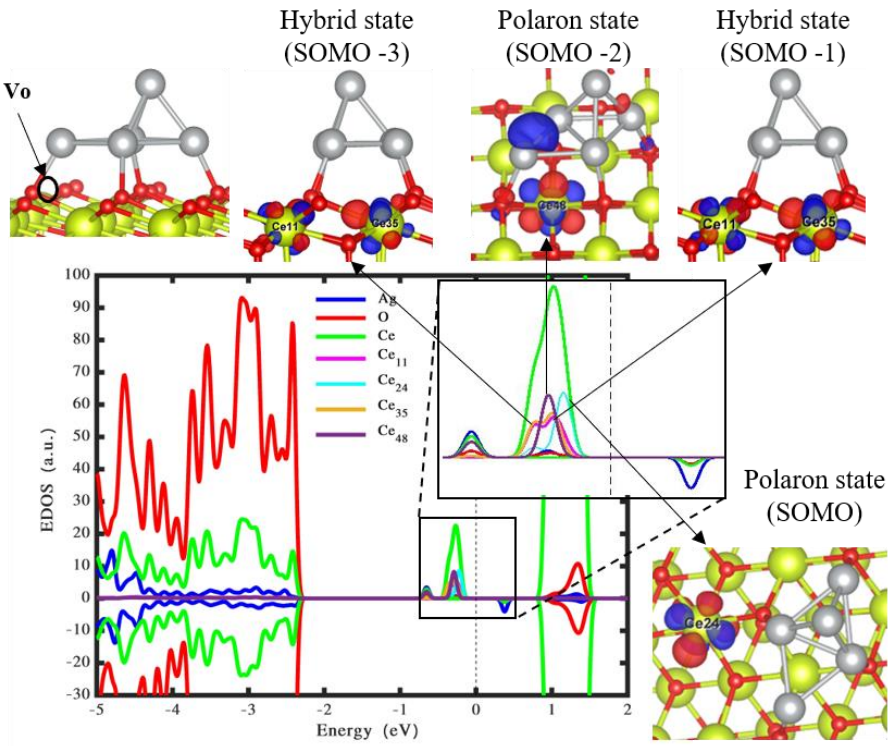

Fig. 5-7 Wavefunction and density of states of the most stable bipyramidal Ag_5 cluster deposited on the reduced CeO_2 (111) surface. The green, red, and blue show the states located on the cerium, oxygen, and silver atoms, while the pink, cyan, brown, and purple peaks between −1- 0 eV represent the polaronic states located on the cerium ions.

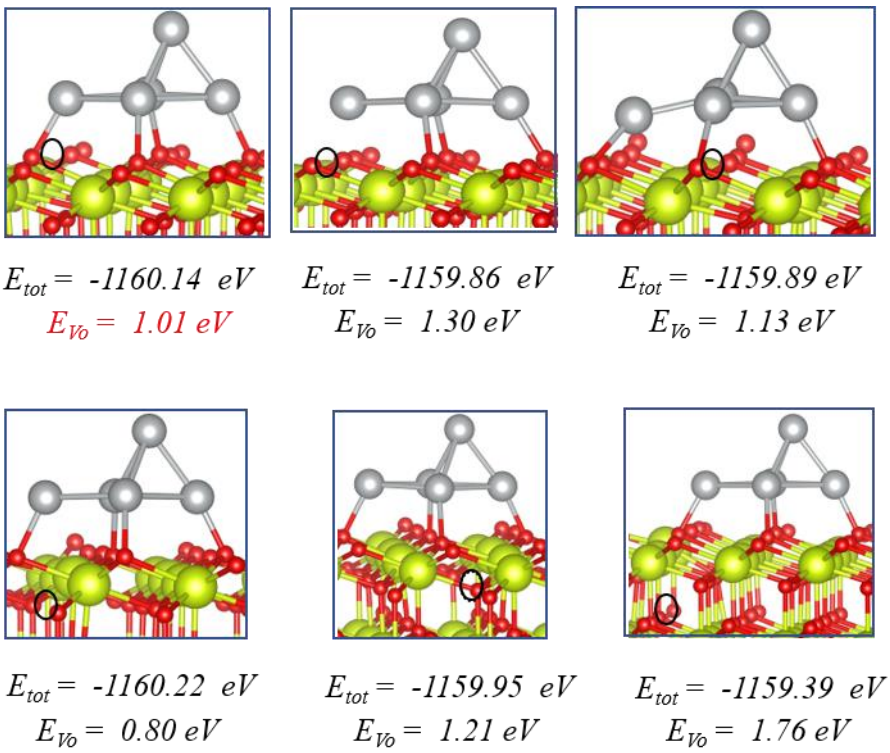

Fig. 5-8 Creation of an oxygen vacancy at surface and subsurface sites of deformed bipyramidal $Ag_5@CeO_2$ (111). The black circles indicate the oxygen vacancy site, the values in the first line represent the total energy of the complex, while the values in the second line represent the energy of oxygen vacancy.

After investigating the defective ceria (111) when the bipyramidal Ag_5 cluster is deposited on its surface, we now analyse the adsorption of trapezoidal Ag_5 AQC on the defective ceria (111). An oxygen atom is removed from the top layer of the oxide which is located just beside the adsorbed cluster as can be seen in Fig. 5-9. Based on the density of states results, further gap states are produced within the band gap of the bulk compared with the perfect $Ag_5@CeO_2$ (111). For example, there exists a total of five Ce^{3+} ions (see the wavefunctions SOMOs in Fig. 5-9); three are caused by charge transfer from the Ag_5 AQC, which are confirmed by the

Bader charge analysis on the Ag_5 AQC (1.3 e^-). The other two ions are due to the presence of oxygen vacancy. The oxygen vacancy formation energy is 1.01 eV, which is dramatically lower than the bare oxide. Table 5- 3 summarises the total, formation energies and total cluster charge of configurations shown in Fig. 5-7 and Fig. 5-9. In summary and based on our hybrid calculations, it is found that both types of Ag_5 AQCs deposited on defective ceria are further oxidised and donate more charge to the support compared with stoichiometric ceria. Therefore, they indeed reduce the oxygen formation energy. Other optimal structures using different sites of oxygen vacancy are presented in Fig. 5-10.

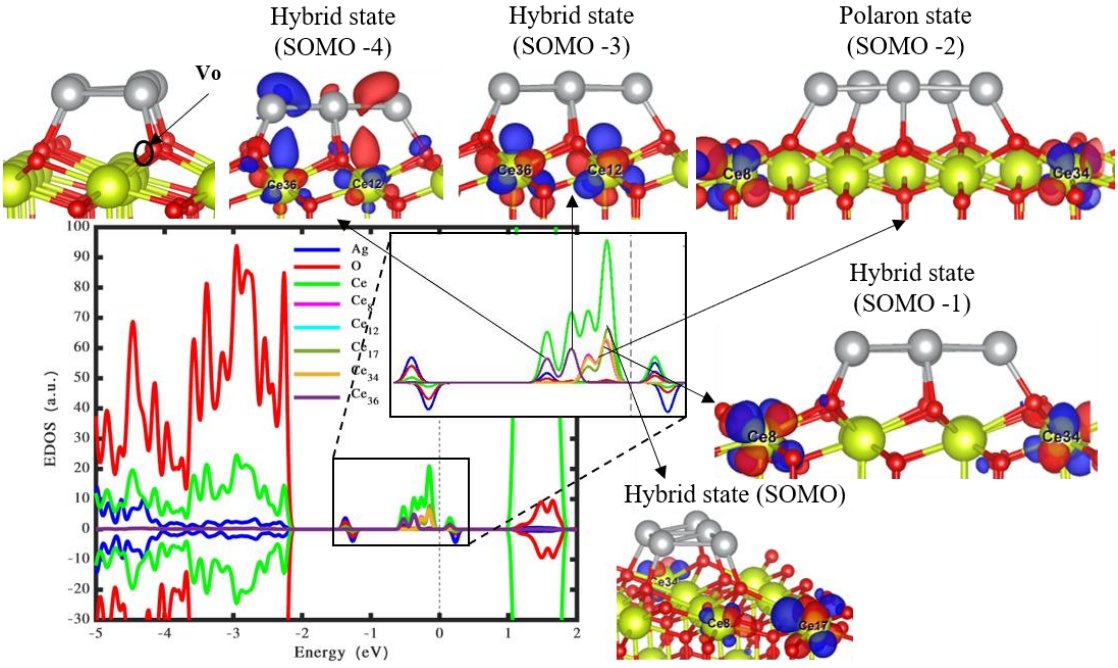

Fig. 5-9 Wavefunction and density of states of the most stable trapezoidal Ag_5 cluster deposited on a reduced CeO_2 (111) surface. The green, red, and blue

show the states located on the cerium, oxygen, and silver atoms, while the pink, cyan, dark green, brown, and purple peaks between −1- 0 eV represent the polaronic states located on the cerium ions.

Table 5- 3 Total, formation energies and total charge of the most stable (deformed) bipyramidal and lying-down trapezoidal Ag_5 clusters on reduced CeO_2 (111).

Configuration	Total energy (eV)	Formation energy (eV)	Q_{Ag5} (e^-)
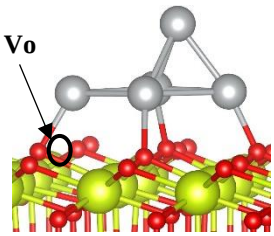	−1160.14	1.01	1.02
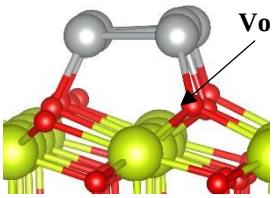	−1160.65	1.02	1.31

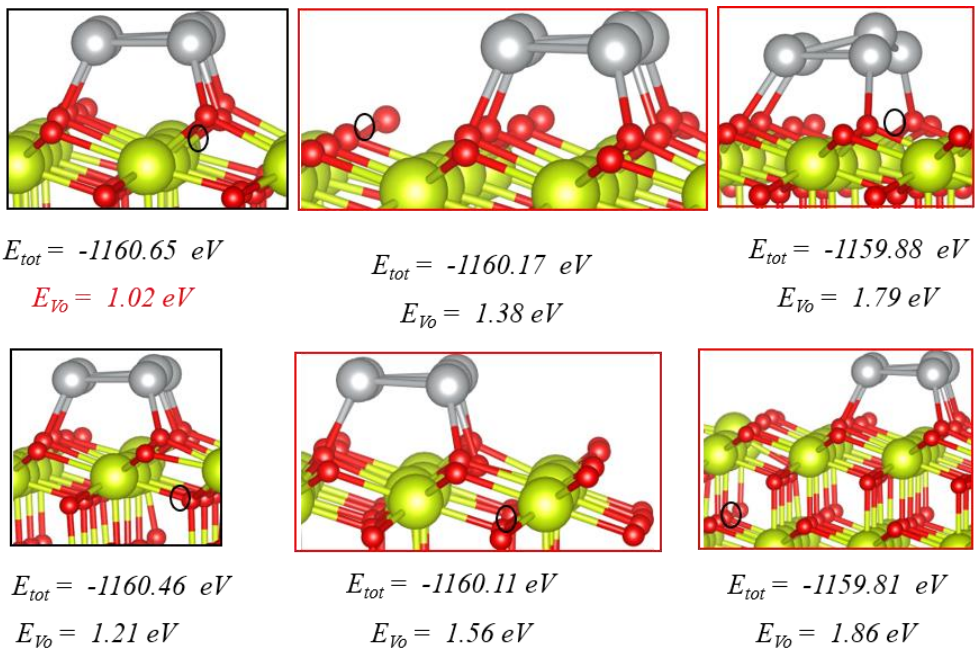

Fig. 5-10 Creation of an oxygen vacancy at the surface and subsurface sites of the trapezoidal Ag_5@CeO_2 (111). The black circles indicate the oxygen vacancy site, the values in the first line represent the total energy of the complex, while the values in the second line represent the energy of oxygen vacancy.

5.2.3 Gas Phase Calculations of Ag_2SiO_3 Adsorbed on Bipyramidal and Trapezoidal Ag_5 Clusters

In order to understand the effect of the purification process with silicate (SiO_3^{2-}) [177] to extract Ag_5 AQCs from water solutions in the experiment, the adsorption of Ag_2SiO_3 on isolated bipyramidal and trapezoidal Ag_5 AQCs is investigated. Two

Ag ions are taken into consideration in the simulation, because of two factors. On the one hand, when the Ag_5 cluster is synthesised in water solutions, there exist Ag^+ ions, which might affect the photocatalytic properties. On the other hand, Ag^+ acts as counterions to neutralise silicate (SiO_3^{2-}). After testing different adsorption positions of Ag_2SiO_3 on both Ag_5 AQCs, it is found that structures shown in Fig. 5-11(a) and Fig. 5-11(b) are the most thermodynamically stable with an adsorption energy of −2.2 eV for both configurations. It is worth mentioning that the Ag_5 clusters are kept isolated from the two Ag^+ ions in which there is no interaction between them, so that the systems are still considered to be Ag_2SiO_3@Ag_5 rather than being SiO_3^{2-}@Ag_7. Information on the Ag-O and Si-O bond lengths is presented in Table 5- 4.

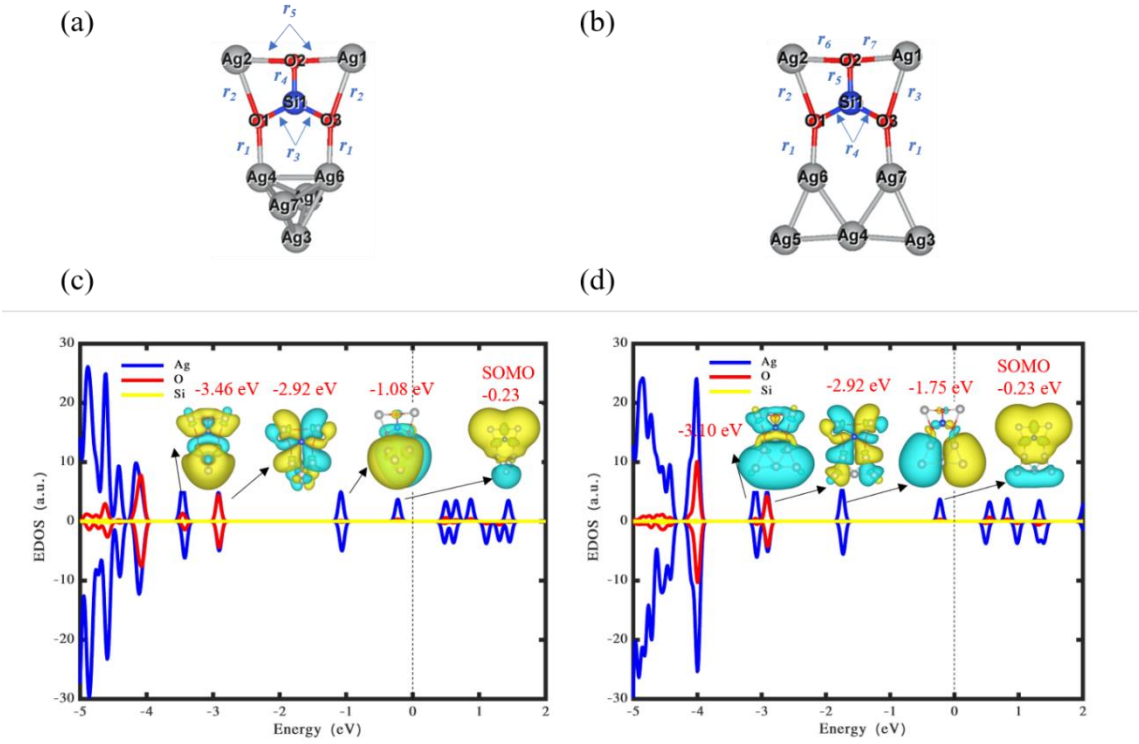

Fig. 5-11 Optimised Ag_2/SiO_3 adsorbed on bipyramidal (a) and trapezoidal (b) Ag_5 isomers in the gas phase. r_1-r_7 show the Ag-O and Si-O bond lengths.

The corresponding values are shown in Table 5-4. Blue, red, and grey balls represent silicon, oxygen, and silver atoms. (c) The density of states and frontier molecular orbitals of bipyramidal configuration. (d) The density of states and frontier molecular orbitals of trapezoidal configuration. SOMO: singly occupied molecular orbital. The blue, red, and yellow represent the states located on silver, oxygen, and silicon atoms.

Table 5- 4 Bond lengths of configurations shown in Fig. 5-11 obtained using the hybrid functional HSE06.

Bond length	r_1(Å)	r_2(Å)	r_3(Å)	r_4(Å)	r_5(Å)	r_6(Å)	r_7(Å)
Structure (a)	2.20	2.60	1.60	1.61	2.30	-	-
Structure (b)	2.15	2.56	2.65	1.60	1.61	2.31	2.28

To compare the electronic structures of these modelled systems, with the bare clusters shown in Fig. 4-1, there exists a further gap state at −2.92 eV for both structures (see the density of states and wavefunctions in Fig. 5-11(c) and Fig. 5-11(d)). This gap state appears due to charge transfer from the Ag_5 clusters, the adsorbed Ag^+ ions, and the silicon atom to oxygen atoms being negatively charged. This is also confirmed by the Bader charge distribution as can be illustrated in Table 5- 5. Furthermore, based on Bader's charge information, it can be clearly

observed that atoms labelled Ag5 and Ag7 in structure (a) are negatively charged because they are not bonded to the adsorbed silicate. The same is found for atoms labelled Ag3 and Ag5 in structure (b). As expected, there is an effect of the adsorption of silicate on the band gap of both Ag_5 AQCs, as clearly seen in the density of states (see peaks at −2.2 eV in Fig. 5-11(c) and Fig. 5-11(d)).

Table 5- 5 Bader charges of configurations shown in Fig. 5-11 obtained using the hybrid functional HSE06. Red colour labelling the Ag atoms represents the atoms of the clusters.

Atom label	**Structure (a)**	**Structure (b)**
Ag1 (e^-)	0.34	0.38
Ag2 (e^-)	0.37	0.38
Ag3 (e^-)	0.10	−0.04
Ag4 (e^-)	0.31	0.10
Ag5 (e^-)	−0.14	−0.05
Ag6 (e^-)	0.37	0.29
Ag7 (e^-)	−0.12	0.27
O1 (e^-)	−1.28	−1.39

O2 (e^-)	−1.32	−1.34
O3 (e^-)	−1.5	−1.38
Si (e^-)	2.91	2.85

5.2.4 The Adsorption of Ag_2SiO_3 on Bipyramidal and Trapezoidal $Ag_5@CeO_2$ (111)

5.2.4.1 On Perfect CeO_2 (111)

In **Section 5.2.2.1**, we studied the effect of both the bipyramidal and trapezoidal Ag_5 AQCs on electronic structures of CeO_2 (111) surface. We now investigate the effect of deposition of $Ag_2SiO_3@Ag_5$, that are shown in Fig. 5-11(a) and Fig. 5-11(b) on the substrate. This study is conducted to evaluate the effect of the purification process that takes place in water solution and to report its impact on the photocatalytic activity of a perfect ceria. Therefore, we deposit both bipyramidal and trapezoidal $Ag_2SiO_3@Ag_5$ AQCs on the ceria surface as can be seen in Fig. 5-12. For example, for the optimised bipyramidal configuration (see Fig. 5-12(b)), it is clearly observed that the Ag_5 cluster deforms significantly upon adsorption of the perfect ceria surface, losing approximately 1.13 e^-, which is a double charge transfer as compared to the structure without the deposition of Ag_2SiO_3 (i.e., see structure shown in Fig. 5-3(b)). A portion of this transferred charge is localised on

a Ce^{3+} ion, creating a polaron located on the substrate's surface. Furthermore, the optimised trapezoidal configuration is shown in Fig. 5-12(d). The cluster transfers approximately 1.18 e^-, which is ~0.18 e^- more charge transfer than the trapezoidal $Ag_5@CeO_2$ without the adsorption of Ag_2SiO_3 (i.e., see structure shown in Fig. 5-5(d)). To compare both structures shown in Fig. 5-12 in terms of their stability, the configuration presented in Fig. 5-12(d) shows higher stability than that of the configuration presented in Fig. 5-12(b) of ~3.2 eV in energy.

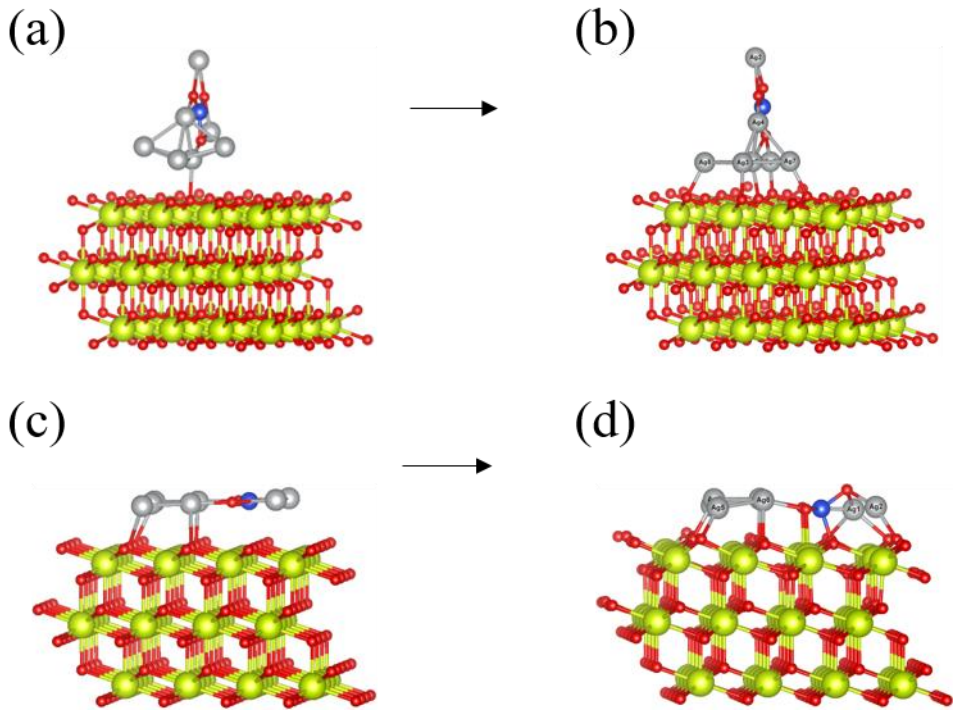

Fig. 5-12 (a) and (b) Initial and optimised structures of Ag_2/SiO_3 deposited on bipyramidal $Ag_5@CeO_2$ (111), (c) and (d) Initial and optimised structures of Ag_2/SiO_3 deposited on trapezoidal $Ag_5@CeO_2$ (111). The green, red, blue, and grey balls represent cerium, oxygen, silicon, and silver atoms.

Moving to the analysis of electronic structures of both configurations, the density of states and wavefunctions are provided in Fig. 5-13. To make a comparison between the density of states for both configurations with the density of states of the same configurations, but without the deposition of Ag_2SiO_3 (see Fig. 5-6(a) and Fig. 5-6(b)), it is clearly seen that the number of polaronic states is the same. For instance, the bipyramidal structure retains its single polaronic state, and the trapezoidal structure also keeps its double polaronic states (see Fig. 5-13(a) and Fig. 5-13(b)). However, the number of gap states increases in both structures. This means that the adsorption of Ag_2SiO_3 on both $Ag_5@CeO_2$ systems contributes to a further charge transfer, which therefore creates additional gap states. These gap states have low energy and are located away from the surface of ceria. Experimentally, it has been observed that the photocatalytic activity of a TiO_2 surface was decreased upon the adsorption of SiO_3^{2-} [177]. This decrease in the photocatalytic activity of TiO_2 could be recovered by flushing the experimental tools with distilled water. To conclude this section, silicate deposition purifies the Ag_5 AQCs in a water solution. One should mention that the doping of Ag_2SiO_3 does not reduce the band gap of CeO_2 (111) of both structures. Table 5- 6 illustrates the charges distribution of the adsorbed Ag_2/SiO_3 and Ag_5 clusters of both configurations based on Bader charge analysis to get deeper information on the charge transfer.

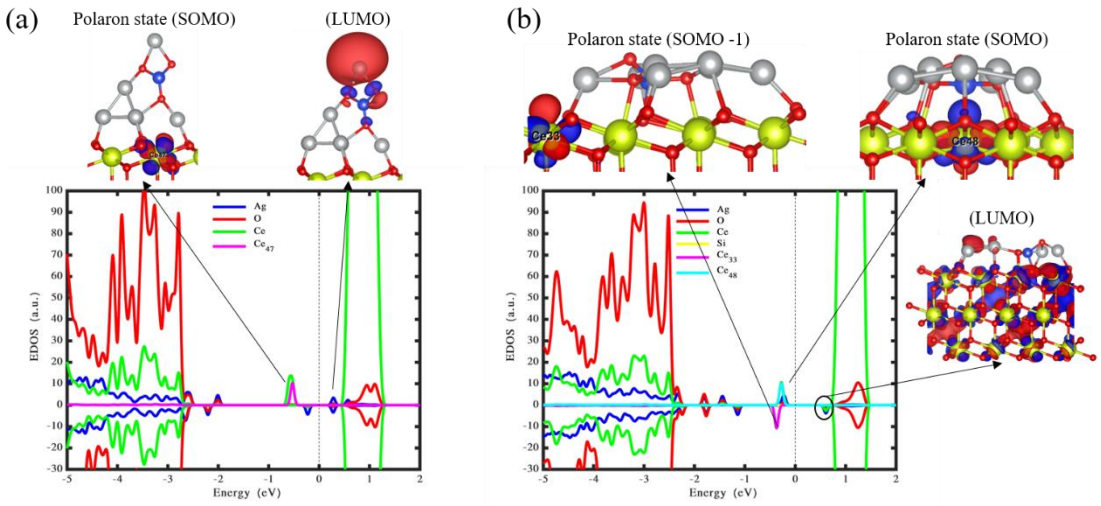

Fig. 5-13 Wavefunction and density of states of (a) Ag_2SiO_3 deposited on bipyramidal $Ag_5@CeO_2$ (111), (b) Ag_2SiO_3 deposited on trapezoidal $Ag_5@CeO_2$ (111). The green, red, and blue show the states located on cerium, oxygen, and silver atoms, while the pink and cyan peaks between −1- 0 eV represent the polaronic states located on Ce ions.

Table 5- 6 Bader charges of configurations shown in Fig. 5-12 obtained using the hybrid functional HSE06. Red colour labelling the Ag atoms represents the atoms of the clusters.

Atom label	Structure (a)	Structure (b)
Ag1 (e^-)	0.56	0.62
Ag2 (e^-)	0.68	0.55
Ag3 (e^-)	0.20	0.22

Ag4 (e^-)	0.21	0.07
Ag5 (e^-)	0.17	0.22
Ag6 (e^-)	0.34	0.35
Ag7 (e^-)	0.21	0.33
O1 (e^-)	−0.47	−0.47
O2 (e^-)	−0.44	−0.40
O3 (e^-)	−0.43	−0.46
Si (e^-)	3.01	3.15

5.2.4.2 On Reduced CeO_2 (111)

In the previous section, we investigated the effect of Ag_2SiO_3 on Ag_5 deposited on a perfect CeO_2 (111). We now present the calculations for Ag_5@reduced CeO_2 (111) doped with Ag_2SiO_3. For example, Fig. 5-14 shows the density of states and wavefunctions of the deformed bipyramidal configuration. An oxygen atom is eliminated from the top layer of CeO_2, which is close to the deposited cluster. A significant charge transfer is found of approximately 1.60 e^- from the cluster to the support, resulting in the formation of three polarons, which are all located on the top layer of the support, while two polarons are formed due to the existence of an

oxygen vacancy (see wavefunctions SOMO, SOMO-1, SOMO-2, SOMO-3, and SOMO-4 in Fig. 5-14). The deposition of Ag_2SiO_3 reduces the formation energy of the oxygen vacancy by approximately 0.18 eV compared to the formation energy of the oxygen vacancy without depositing Ag_2SiO_3 (see Fig. 5-7).

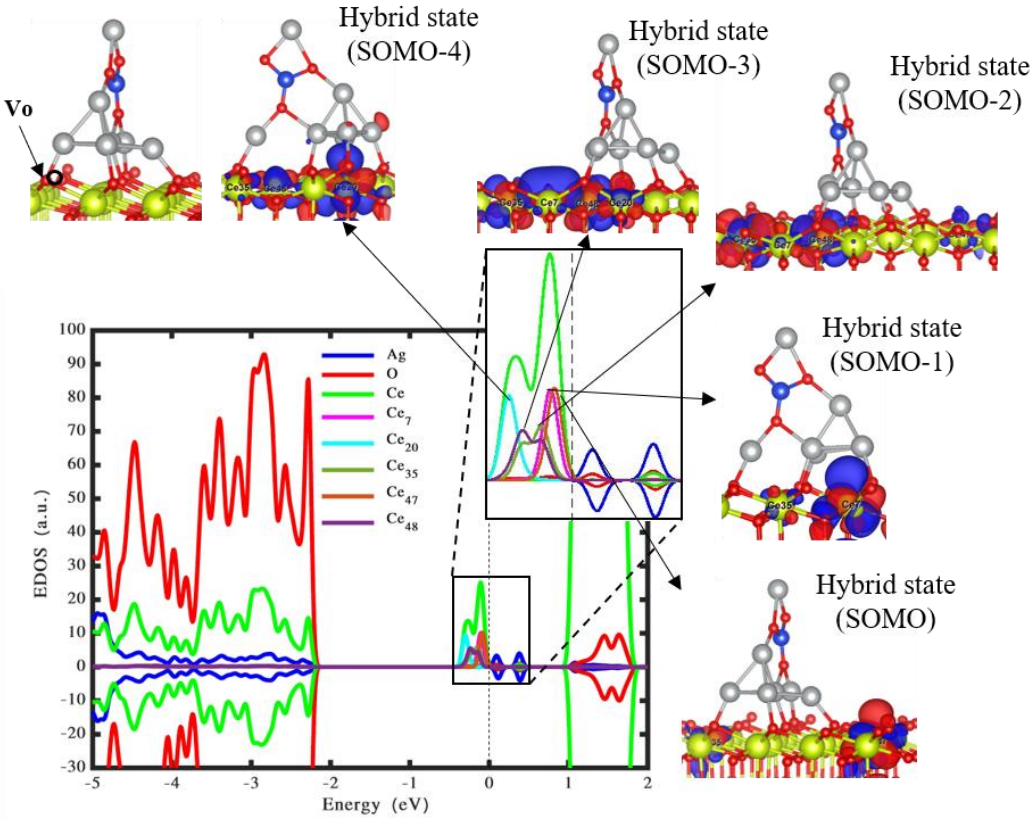

Fig. 5-14 Wavefunction and density of states of Ag_2/SiO_3 deposited on (deformed) bipyramidal $Ag_5@CeO_2$ (111). The green, red, and blue show the states located on cerium, oxygen, and silver atoms, while the pink, cyan, purple, brown, and dark green peaks between −0.5- 0 eV represent the polaronic states located on Ce ions.

After studying the Ag_2SiO_3 deposited on the bipyramidal Ag_5@reduced CeO_2 (111) system, we now investigate the trapezoidal configuration as depicted in Fig. 5-15, and its density of states coupled with its wavefunctions are also shown. As can be clearly seen that there are five polarons located on the top layer of the supports, which are formed due to the deposition of the cluster and the presence of an oxygen vacancy. A slight reduction in the formation energy of an oxygen vacancy is obtained of approximately 0.1 eV compared with the structure without the deposition of Ag_2SiO_3 (see Fig. 5-9). To make a comparison in terms of charge transfer with the system shown in Fig. 5-13(b), a significant charge transfer from the cluster to the support, which is around 1.6 e^- higher in charge transfer, resulting in further gap states. This significant charge transfer can be attributed to the formation of an oxygen vacancy. The gap states shown by the density of states in Fig. 5-15 play a crucial role in boosting the photocatalytic activity of the oxide. To sum up, doping Ag_5@defective CeO_2 (111) with Ag_2SiO_3 suggests that the energy required to release an oxygen atom from the oxide surface is further lowered and accompanied by improvement in its photocatalytic activity. To get further information on the charge transfer of the structures shown in Fig. 5-14 and Fig. 5-15, Table 5- 7 illustrates the charges distribution of the adsorbed Ag_2SiO_3 and Ag_5 clusters of both configurations based on Bader charge analysis.

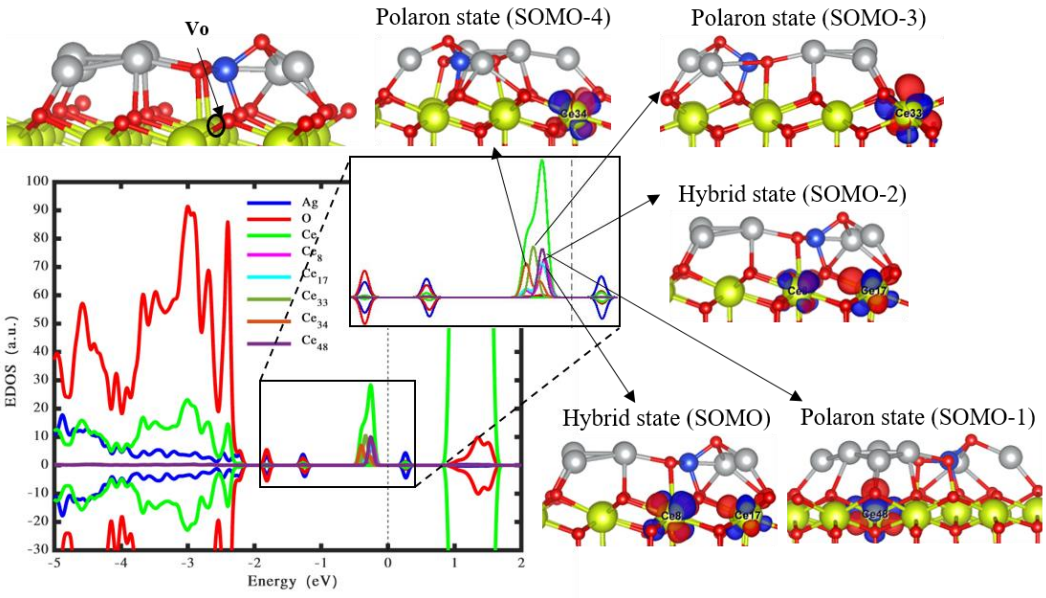

Fig. 5-15 Wavefunction and density of states of Ag_2SiO_3 deposited on trapezoidal $Ag_5@CeO_2$ (111). The green, red, and blue show the states located on cerium, oxygen, and silver atoms, while the pink, cyan, purple, brown, and dark green peaks between −1- 0 eV represent the polaronic states located on Ce ions.

Table 5- 7 Bader charges of configurations shown in Fig. 5-14 and Fig. 5-15 obtained using the hybrid functional HSE06. Red colour labelling the Ag atoms represents the atoms of the clusters

Atom label	**Structure (a)**	**Structure (b)**
Ag1 (e^-)	0.53	0.62
Ag2 (e^-)	0.67	0.55

Ag3 (e^-)	0.26	0.37
Ag4 (e^-)	0.21	0.08
Ag5 (e^-)	0.31	0.38
Ag6 (e^-)	0.38	0.40
Ag7 (e^-)	0.41	0.40
O1 (e^-)	−0.47	−0.47
O2 (e^-)	−0.44	−0.40
O3 (e^-)	−0.44	−0.46
Si (e^-)	3.01	3.14

5.3 **Conclusion**

In this chapter, we aimed to obtain a deep insight into the reactivity of Ag_5 AQCs adsorbed on a perfect and reduced CeO_2 (111) towards water splitting by investigating the modifications in electronic structures occurring on the oxide surface. Trapezoidal and bipyramidal Ag_5 AQCs deposited on perfect and reduced CeO_2 (111) with and without the adsorption of Ag_2SiO_3 have been computationally studied using periodic spin-polarised hybrid DFT calculations. The adsorption energy of Ag_5 AQC and the formation energy of an oxygen vacancy have been

considered. It has been found that depositing Ag_5 can extend the absorption range to the visible light region. As expected, the adsorbed Ag_5 AQCs inject charges to the oxide, leading to the reduction of Ce^{4+} ions to Ce^{3+} ions. The concentration of these Ce^{3+} ions can be enhanced by forming an oxygen vacancy on the oxide. Our calculations also show that the formation energy of this oxygen vacancy on the support is reduced dramatically by simple contact with Ag_5 AQCs.

Furthermore, with respect to the purification process, when $Ag_5@CeO_2$ (111) systems are doped with Ag_2SiO_3, the photocatalytic activity of CeO_2 (111) is not affected. However, there is a further charge transfer from Ag_5 AQC as well as from the silicate to the support. It is also observed that the adsorption of Ag_2SiO_3 leads to a further reduction in the formation energy of an oxygen vacancy of all modelled systems. The results presented in this chapter pave a new technique to design plasmonic photocatalysts for enhancing the photocatalytic activity of CeO_2 (111) surface using abundant solar radiation.

6 Summary and Future Work

This thesis aims to improve the photocatalytic activity of different metal oxides using Ag_5 AQCs towards hydrogen production. This thesis used DFT mixed with HF techniques implemented in VASP software. These theoretical techniques provided a new way to investigate interactions that takes place at the interface of the Ag_5 AQCs and photocatalysts. In **Chapter 4**, we investigated the effect of trapezoidal and bipyramidal Ag_5 AQCs on both anatase (101) and rutile (110) TiO_2 surfaces. We noted that small gaps are created in the mid-gap due to the injection of electrons from these AQCs into the photocatalysts. These gap states could absorb photons at lower energy.

Further gap states are observed due to the formation of an oxygen vacancy on the oxides. This means that the photocatalytic efficiency of the materials is further boosted. In **Chapter 5**, we systematically studied the adsorption of Ag_5 AQCs on a CeO_2 (111) surface. We also observed a few gap states appear in the band gap. The number of these gap states was also increased by forming an oxygen vacancy. While doping the surface of ceria with Ag_5 AQCs, the formation energy of this oxygen vacancy is significantly reduced. Furthermore, the presence of silicate shows a good impact on improving the photocatalytic activity of ceria in terms of photo absorption.

A few research directions should be considered based on the developments and findings shown in **Chapter 4** and **Chapter 5**, which this thesis has not explored. First, further investigations can be carried out on bimetallic AQCs such as Ag_5 and Cu_5 in order to improve the photocatalytic activity of the modelled oxides. Second, combining titania with ceria considering Ag_5 AQCs can also be investigated to further push the absorption range into the visible light region. Third, carbon nitride (C_3N_4) has shown improved photocatalytic activity in the visible light range when its surface has been modified. Therefore, Ag_5 AQCs could be used to decorate a C_3N_4 surface, which may boost its ability to use the solar spectrum at even lower energy. Fourth, there is also an opportunity to study the adsorption of other metal clusters, such as Pt, molybdenum (Mo), ruthenium (Ru), etc., relevant to photocatalytic processes. Finally, since basic models have been investigated, the energetics and kinetics of water splitting process on surfaces such as Ag_5@tiania and Ag_5@ceria could be performed. Simultaneously, a more realistic analysis of Ag_5 on titania and ceria surfaces could be performed using *ab initio* molecular dynamics (AIMD) to explore the effect of thermodynamics of water splitting on the surface of photocatalysts.

7 Bibliography

[1] C. Kim, M. Choi, and J. Jang, “Nitrogen-doped SiO2/TiO2 core/shell nanoparticles as highly efficient visible light photocatalyst,” *Catal. Commun.*, vol. 11, no. 5, pp. 378–382, 2010, doi: 10.1016/j.catcom.2009.11.005.

[2] A. B. Murphy *et al.*, “Efficiency of solar water splitting using semiconductor electrodes,” *Int. J. Hydrogen Energy*, vol. 31, no. 14, pp. 1999–2017, 2006, doi: 10.1016/j.ijhydene.2006.01.014.

[3] F. Akira, T. N. Rao, and Donald A. Tryk, “Titanium dioxide photocatalysis,” *J. Photochem. Photobiol. C*, vol. 1, no. 1, pp. 1–21, 2000.

[4] X. He, Y. Guo, J. Liu, X. Li, and J. Qi, “Fabrication of peanut-like TiO2 microarchitecture with enhanced surface light trapping and high specific surface area for high-efficiency dye sensitized solar cells,” *J. Power Sources*, vol. 423, no. January, pp. 236–245, 2019, doi: 10.1016/j.jpowsour.2019.03.090.

[5] Y. Maeda, Y. Iizuka, and M. Kohyama, “Generation of oxygen vacancies at a Au/TiO2 perimeter interface during co oxidation detected by in situ electrical conductance measurement,” *J. Am. Chem. Soc.*, vol. 135, no. 2, pp. 906–909, 2013, doi: 10.1021/ja310999c.

[6] M. S. Hamdy, W. H. Saputera, E. J. Groenen, and G. Mul, “A novel TiO2 composite for photocatalytic wastewater treatment,” *J. Catal.*, vol. 310, pp.

75–83, 2014, doi: 10.1016/j.jcat.2013.07.017.

[7] J. Wu, S. Lu, D. Ge, L. Zhang, W. Chen, and H. Gu, “Photocatalytic properties of Pd/TiO2 nanosheets for hydrogen evolution from water splitting,” *RSC Adv.*, vol. 6, no. 72, pp. 67502–67508, 2016, doi: 10.1039/c6ra10408h.

[8] S. Kment *et al.*, “Photoanodes based on TiO2 and α-Fe2O3 for solar water splitting-superior role of 1D nanoarchitectures and of combined heterostructures,” *Chem. Soc. Rev.*, vol. 46, no. 12, pp. 3716–3769, 2017, doi: 10.1039/c6cs00015k.

[9] X. Chen and S. S. Mao, “Titanium dioxide nanomaterials: Synthesis, properties, modifications and applications,” *Chem. Rev.*, vol. 107, no. 7, pp. 2891–2959, 2007, doi: 10.1021/cr0500535.

[10] F. De Angelis, C. Di Valentin, S. Fantacci, A. Vittadini, and A. Selloni, “Theoretical studies on anatase and less common TiO2phases: Bulk, surfaces, and nanomaterials,” *Chem. Rev.*, vol. 114, no. 19, pp. 9708–9753, 2014, doi: 10.1021/cr500055q.

[11] Z. Fei Yin, L. Wu, H. Gui Yang, and Y. Hua Su, “Recent progress in biomedical applications of titanium dioxide,” *Phys. Chem. Chem. Phys.*, vol. 15, no. 14, pp. 4844–4858, 2013, doi: 10.1039/c3cp43938k.

[12] M. Kralova, P. Dzik, M. Vesely, and J. Cihlar, “Preparation and characterization of doped titanium dioxide printed layers,” *Catal. Today*, vol. 230, pp. 188–196, 2014, doi: 10.1016/j.cattod.2013.09.018.

[13] L. Wei, C. Yu, Q. Zhang, H. Liu, and Y. Wang, “TiO2-based heterojunction

photocatalysts for photocatalytic reduction of CO2 into solar fuels," *J. Mater. Chem. A*, vol. 6, no. 45, pp. 22411–22436, 2018, doi: 10.1039/c8ta08879a.

[14] G. N. Zhu, Y. G. Wang, and Y. Y. Xia, "Ti-based compounds as anode materials for Li-ion batteries," *Energy Environ. Sci.*, vol. 5, no. 5, pp. 6652–6667, 2012, doi: 10.1039/c2ee03410g.

[15] T. Zhu and S. P. Gao, "The stability, electronic structure, and optical property of tio 2 polymorphs," *J. Phys. Chem. C*, vol. 118, no. 21, pp. 11385–11396, 2014, doi: 10.1021/jp412462m.

[16] D. A. Panayotov and J. R. Morris, "Surface chemistry of Au/TiO2: Thermally and photolytically activated reactions," *Surf. Sci. Rep.*, vol. 71, no. 1, pp. 77–271, 2016, doi: 10.1016/j.surfrep.2016.01.002.

[17] „tefan Neatu, J. A. Maciá-Agullò, P. Concepciòn, and H. Garcia, "Gold-copper nanoalloys supported on TiO2 as photocatalysts for CO2 reduction by water," *J. Am. Chem. Soc.*, vol. 136, no. 45, pp. 15969–15976, 2014, doi: 10.1021/ja506433k.

[18] S. Chainarong, L. Sikong, S. Pavasupree, and S. Niyomwas, "Synthesis and characterization of nitrogen-doped TiO2 nanomaterials for photocatalytic activities under visible light," *Energy Procedia*, vol. 9, pp. 418–427, 2011, doi: 10.1016/j.egypro.2011.09.046.

[19] H. Fujii, K. Inata, M. Ohtaki, K. Eguchi, and H. Arai, "Synthesis of TiO2/CdS nanocomposite via TiO2 coating on CdS nanoparticles by compartmentalized hydrolysis of Ti alkoxide," *J. Mater. Sci.*, vol. 36, no. 2, pp.

527–532, 2001, doi: 10.1023/A:1004857419242.

[20] M. Mba *et al.*, "Sensitization of nanocrystalline TiO2 with multibranched organic dyes and co(III)/(II) Mediators: Strategies to improve charge collection efficiency," *J. Phys. Chem. C*, vol. 117, no. 39, pp. 19885–19896, 2013, doi: 10.1021/jp4067586.

[21] M. Klein *et al.*, "The effect of metal cluster deposition route on structure and photocatalytic activity of mono- and bimetallic nanoparticles supported on TiO 2 by radiolytic method," *Appl. Surf. Sci.*, vol. 378, pp. 37–48, 2016, doi: 10.1016/j.apsusc.2016.03.191.

[22] H. Zhang *et al.*, "Fe2O3/carbon quantum dots complex photocatalysts and their enhanced photocatalytic activity under visible light," *Dalt. Trans.*, vol. 40, no. 41, pp. 10822–10825, 2011, doi: 10.1039/c1dt11147g.

[23] C. H. Liang *et al.*, "The effect of erbium on the adsorption and photodegradation of orange I in aqueous Er3+-TiO2 suspension," *J. Hazard. Mater.*, vol. 138, no. 3, pp. 471–478, 2006, doi: 10.1016/j.jhazmat.2006.05.066.

[24] C. Su, C. H. Liao, J. Di Wang, C. M. Chiu, and B. J. Chen, "The adsorption and reactions of methyl iodide on powdered Ag/TiO 2," *Catal. Today*, vol. 97, no. 1 SPEC. ISS., pp. 71–79, 2004, doi: 10.1016/j.cattod.2004.04.053.

[25] W. Grünert, A. Brückner, H. Hofmeister, and P. Claus, "Structural properties of Ag/TiO2 catalysts for acrolein hydrogenation," *J. Phys. Chem. B*, vol. 108, no. 18, pp. 5709–5717, 2004, doi: 10.1021/jp049855e.

[26] H. Tran, J. Scott, K. Chiang, and R. Amal, "Clarifying the role of silver deposits on titania for the photocatalytic mineralisation of organic compounds," *J. Photochem. Photobiol. A Chem.*, vol. 183, no. 1–2, pp. 41–52, 2006, doi: 10.1016/j.jphotochem.2006.02.018.

[27] M. Haruta and M. Daté, "Advances in the catalysis of Au nanoparticles," *Appl. Catal. A Gen.*, vol. 222, no. 1–2, pp. 427–437, 2001, doi: 10.1016/S0926-860X(01)00847-X.

[28] A. Sclafani and J. M. Herrmann, "Influence of metallic silver and of platinum-silver bimetallic deposits on the photocatalytic activity of titania (anatase and rutile) in organic and aqueous media," *J. Photochem. Photobiol. A Chem.*, vol. 113, no. 2, pp. 181–188, 1998, doi: 10.1016/S1010-6030(97)00319-5.

[29] P. López-Caballero *et al.*, "Exploring the properties of Ag5-TiO2 interfaces: Stable surface polaron formation, UV-Vis optical response, and CO2 photoactivation," *J. Mater. Chem. A*, vol. 8, no. 14, pp. 6842–6853, 2020, doi: 10.1039/d0ta00062k.

[30] M. P. De Lara-Castells, C. Cabrillo, D. A. Micha, A. O. Mitrushchenkov, and T. Vazhappilly, "Ab initio design of light absorption through silver atomic cluster decoration of TiO2," *Phys. Chem. Chem. Phys.*, vol. 20, no. 28, pp. 19110–19119, 2018, doi: 10.1039/c8cp02853b.

[31] A. S. Mazheika, V. E. Matulis, and O. A. Ivashkevich, "Quantum chemical study of adsorption of Ag2, Ag4 and Ag8 on stoichiometric TiO2 (1 1 0) surface," *J. Mol. Struct. THEOCHEM*, vol. 942, no. 1–3, pp. 47–54, 2010, doi: 10.1016/j.theochem.2009.11.032.

[32] H. Perron, C. Domain, J. Roques, R. Drot, E. Simoni, and H. Catalette, "Optimisation of accurate rutile TiO2 (110), (100), (101) and (001) surface models from periodic DFT calculations," *Theor. Chem. Acc.*, vol. 117, no. 4, pp. 565–574, 2007, doi: 10.1007/s00214-006-0189-y.

[33] M. Ramamoorthy, D. Vanderbilt, and R. D. King-Smith, "First-principles calculations of the energetics of stoichiometric TiO2 surfaces," *Phys. Rev. B*, vol. 49, no. 23, pp. 16721–16727, 1994, [Online]. Available: http://link.aps.org/doi/10.1103/PhysRevB.49.16721.

[34] H. Zhang and J. F. Banfield, "Thermodynamic analysis of phase stability of nanocrystalline titania," *J. Mater. Chem.*, vol. 8, no. 9, pp. 2073–2076, 1998, doi: 10.1039/a802619j.

[35] M. R. Ranade *et al.*, "Energetics of nanocrystalline TiO2," *Proc. Natl. Acad. Sci. U. S. A.*, vol. 99, pp. 6476–6481, 2002, doi: 10.1073/pnas.251534898.

[36] M. Grätzel, "Photoelectrochemical cells," *Nature*, vol. 414, no. November, pp. 338–344, 2001.

[37] M. Lazzeri, A. Vittadini, and A. Selloni, "Structure and energetics of stoichiometric TiO2 anatase surfaces," *Phys. Rev. B - Condens. Matter Mater. Phys.*, vol. 63, no. 15, pp. 1554091–1554099, 2001, doi: 10.1103/PhysRevB.63.155409.

[38] X. D. Feng *et al.*, "Converting Ceria Polyhedral Nanoparticles into Single-Crystal Nanospheres," *Science (80-.).*, vol. 312, pp. 1504–1509, 2006.

[39] S. Armini, J. De Messemaeker, C. M. Whelan, M. Moinpour, and K. Maex,

"Composite Polymer Core–Ceria Shell Abrasive Particles during Oxide CMP: A Defectivity Study," *J. Electrochem. Soc.*, vol. 155, no. 9, p. H653, 2008, doi: 10.1149/1.2949085.

[40] H. W. Jen *et al.*, "Characterization of model automotive exhaust catalysts: Pd on ceria and ceria-zirconia supports," *Catal. Today*, vol. 50, no. 2, pp. 309–328, 1999, doi: 10.1016/S0920-5861(98)00512-4.

[41] S. H. Oh and G. B. Hoflund, "Chemical state study of palladium powder and ceria-supported palladium during low-temperature CO oxidation," *J. Phys. Chem. A*, vol. 110, no. 24, pp. 7609–7613, 2006, doi: 10.1021/jp060435u.

[42] R. Di Monte and J. Kašpar, "On the role of oxygen storage in three-way catalysis," *Top. Catal.*, vol. 28, no. 1–4, pp. 47–58, 2004, doi: 10.1023/b:toca.0000024333.08447.f7.

[43] Q. Fu, H. Saltsburg, and M. Flytzani-Stephanopoulos, "Active nonmetallic Au and Pt species on ceria-based water-gas shift catalysts," *Science (80-.).*, vol. 301, no. 5635, pp. 935–938, 2003, doi: 10.1126/science.1085721.

[44] N. Izu, W. Shin, N. Murayama, and S. Kanzaki, "Resistive oxygen gas sensors based on CeO2 fine powder prepared using mist pyrolysis," *Sensors Actuators, B Chem.*, vol. 87, no. 1, pp. 95–98, 2002, doi: 10.1016/S0925-4005(02)00224-1.

[45] X. Liu, K. Zhou, L. Wang, B. Wang, and Y. Li, "Oxygen vacancy clusters promoting reducibility and activity of ceria nanorods," *J. Am. Chem. Soc.*, vol. 131, no. 9, pp. 3140–3141, 2009, doi: 10.1021/ja808433d.

[46] Y. L. Song, L. L. Yin, J. Zhang, P. Hu, X. Q. Gong, and G. Lu, "A DFT + U study of CO oxidation at CeO2(110) and (111) surfaces with oxygen vacancies," *Surf. Sci.*, vol. 618, pp. 140–147, 2013, doi: 10.1016/j.susc.2013.09.001.

[47] K. Otsuka, M. Hatano, and A. Morikawa, "Hydrogen from water by reduced cerium oxide," *J. Catal.*, vol. 79, no. 2, pp. 493–496, 1983, doi: 10.1016/0021-9517(83)90346-9.

[48] S. Abanades, A. Legal, A. Cordier, G. Peraudeau, G. Flamant, and A. Julbe, "Investigation of reactive cerium-based oxides for H2 production by thermochemical two-step water-splitting," *J. Mater. Sci.*, vol. 45, no. 15, pp. 4163–4173, 2010, doi: 10.1007/s10853-010-4506-4.

[49] Z. A. Feng, F. El Gabaly, X. Ye, Z. X. Shen, and W. C. Chueh, "Fast vacancy-mediated oxygen ion incorporation across the ceria-gas electrochemical interface," *Nat. Commun.*, vol. 5, pp. 1–9, 2014, doi: 10.1038/ncomms5374.

[50] H. A. Hansen and C. Wolverton, "Kinetics and Thermodynamics of H2O Dissociation on Reduced CeO2(111)," *J. Chem. Phys.*, vol. 118, pp. 27402–27414, 2014, doi: 10.1063/1.5085696.

[51] J. Paier, C. Penschke, and J. Sauer, "Oxygen defects and surface chemistry of ceria: Quantum chemical studies compared to experiment," *Chem. Rev.*, vol. 113, no. 6, pp. 3949–3985, 2013, doi: 10.1021/cr3004949.

[52] C. U. De Cantoblanco, "Computer modeling of surfaces and defects on cerium dioxide," *Surf. Sci.*, vol. 339, pp. 337–352, 1995.

[53] M. Nolan, S. C. Parker, and G. W. Watson, "The electronic structure of oxygen

vacancy defects at the low index surfaces of ceria," *Surf. Sci.*, vol. 595, no. 1–3, pp. 223–232, 2005, doi: 10.1016/j.susc.2005.08.015.

[54] E. Wuilloud, B. Delley, W. D. Schneider, and Y. Baer, "Spectroscopic evidence for localized and extended f-symmetry states in CeO2," *Phys. Rev. Lett.*, vol. 53, no. 2, pp. 202–205, 1984, doi: 10.1103/PhysRevLett.53.202.

[55] D. R. Mullins, S. H. Overbury, and D. R. Huntley, "Electron spectroscopy of single crystal and polycrystalline cerium oxide surfaces," *Surf. Sci.*, vol. 409, no. 2, pp. 307–319, 1998, doi: 10.1016/S0039-6028(98)00257-X.

[56] V. Seminko *et al.*, "Defect and intrinsic luminescence of CeO2 nanocrystals," *Phys. Status Solidi Basic Res.*, vol. 254, no. 4, pp. 1–6, 2017, doi: 10.1002/pssb.201600488.

[57] S. N. Habisreutinger, L. Schmidt-Mende, and J. K. Stolarczyk, "Photocatalytic reduction of CO2 on TiO2 and other semiconductors," *Angew. Chemie - Int. Ed.*, vol. 52, no. 29, pp. 7372–7408, 2013, doi: 10.1002/anie.201207199.

[58] M. Ismael, "A review and recent advances in solar-to-hydrogen energy conversion based on photocatalytic water splitting over doped-TiO2 nanoparticles," *Sol. Energy*, vol. 211, no. October, pp. 522–546, 2020, doi: 10.1016/j.solener.2020.09.073.

[59] S. Yamazoe and T. Tsukuda, *Metal clusters in catalysis*, vol. 2014-Janua, no. 7. 2014.

[60] B. Santiago González and M. A. López-Quintela, "New strategies and synthetic routes to synthesize fluorescent atomic quantum clusters," *RSC*

Smart Mater., vol. 2014-Janua, no. 7, pp. 25–50, 2014.

[61] L. Gerward, J. Staun Olsen, L. Petit, G. Vaitheeswaran, V. Kanchana, and A. Svane, "Bulk modulus of CeO2 and PrO2 - An experimental and theoretical study," *J. Alloys Compd.*, vol. 400, no. 1–2, pp. 56–61, 2005, doi: 10.1016/j.jallcom.2005.04.008.

[62] G. S. Herman, "Surface structure determination of (formula presented) by angle-resolved mass spectroscopy of recoiled ions," *Phys. Rev. B - Condens. Matter Mater. Phys.*, vol. 59, no. 23, pp. 14899–14902, 1999, doi: 10.1103/PhysRevB.59.14899.

[63] T. Kropp, J. Paier, and J. Sauer, "Interactions of water with the (111) and (100) surfaces of ceria," *J. Phys. Chem. C*, vol. 121, no. 39, pp. 21571–21578, 2017, doi: 10.1021/acs.jpcc.7b08150.

[64] A. Beste and S. H. Overbury, "Pathways for ethanol dehydrogenation and dehydration catalyzed by ceria (111) and (100) surfaces," *J. Phys. Chem. C*, vol. 119, no. 5, pp. 2447–2455, 2015, doi: 10.1021/jp509686f.

[65] G. R. Fowles, "Solution of the Schrödinger Equation for the Hydrogen Atom in Rectangular Coordinates," *Am. J. Phys.*, vol. 30, no. 4, pp. 308–309, 1962, doi: 10.1119/1.1941997.

[66] M. Born and R. Oppenheimer, "Zur Quantentheorie der Molekeln," *Ann. Phys.*, vol. 389, no. 20, pp. 457–484, 1927.

[67] D. R. Hartree, "The Wave Mechanics of an Atom with a Non-Coulomb Central Field Part I Theory and Methods," *Math. Proc. Cambridge Philos. Soc.*, pp.

111–132, 1928, doi: 10.1017/S0305004100011919.

[68] G. Lewars, *Introduction to the Theory and Applications of Molecular and Quantum Mechanics*. 2016.

[69] J. C. Slater, "The theory of complex spectra," *Phys. Rev.*, vol. 34, no. 10, pp. 1293–1322, 1929, doi: 10.1103/PhysRev.34.1293.

[70] L. Pauling, "The application of the quantum mechanics to the structure of the hydrogen molecule and hydrogen molecule-ion and to related problems," *Chem. Rev.*, vol. 5, no. 2, pp. 173–213, 1928.

[71] V. Fock, "Näherungsmethode zur Lösung des quantenmechanischen Mehrkörperproblems," *Zeitschrift für Phys.*, vol. 61, no. 1–2, pp. 126–148, 1930, doi: 10.1007/BF01340294.

[72] F. Jensen, "Introduction to computational chemistry," *New York*, 2001.

[73] L. H. Thomas, "The calculation of atomic fields," *Math. Proc. Cambridge Philos. Soc.*, vol. 23, no. 5, pp. 542–548, 1927, doi: 10.1017/S0305004100011683.

[74] E. Fermi, "Eine statistische Methode zur Bestimmung einiger Eigenschaften des Atoms und ihre Anwendung auf die Theorie des periodischen Systems der Elemente," *Zeitschrift für Phys.*, vol. 48, no. 1–2, pp. 73–79, 1928, doi: 10.1007/BF01351576.

[75] K. Burke and L. O. Wagner, "DFT in a nutshell," *Int. J. Quantum Chem.*, vol. 113, no. 2, pp. 96–101, 2013, doi: 10.1002/qua.24259.

[76] E. Teller, “On the stability of molecules in the Thomas-Fermi theory,” *Rev. Mod. Phys.*, vol. 34, no. 4, pp. 627–631, 1962, doi: 10.1103/RevModPhys.34.627.

[77] Hohenberg. P. and Kohn. W., “Inhomogeneous electron gas,” *Phys. Chem. Chem. Phys.*, vol. 155, no. 136, pp. 964–871, 2001, doi: 10.1007/BF01198136.

[78] W. Kohn, and L. Sham, “Self-consistent equations including exchange and correlation effects,” *Phys. Rev.*, vol. 140, pp. 1133–1138, 1965.

[79] P. A. M. Dirac, “Note on Exchange Phenomena in the Thomas Atom,” *Math. Proc. Cambridge Philos. Soc.*, vol. 26, no. 3, pp. 376–385, 1930, doi: 10.1017/S0305004100016108.

[80] J. P. Perdew and Y. Wang, “Accurate and simple analytic representation of the electron-gas correlation energy (Physical Review B (1992) 45 (13244) DOI: 10.1103/PhysRevB.45.13244),” *Phys. Rev. B*, vol. 45, no. 23, pp. 13244–13249, 1992, doi: 10.1103/PhysRevB.98.079904.

[81] J. P. Perdew, K. Burke, and M. Ernzerhof, “Generalized gradient approximation made simple,” *Phys. Rev. Lett.*, vol. 77, no. 18, pp. 3865–3868, 1996, doi: 10.1103/PhysRevLett.77.3865.

[82] J. P. Perdew *et al.*, “Atoms, molecules, solids, and surfaces: Applications of the generalized gradient approximation for exchange and correlation (Physical Review B (1993) 48, 7, (4978)),” *Phys. Rev. B*, vol. 48, no. 7, p. 4978, 1993, doi: 10.1103/PhysRevB.48.4978.2.

[83] M. J. Gillan, D. Alfè, and A. Michaelides, “Perspective: How good is DFT for water?,” *J. Chem. Phys.*, vol. 144, no. 13, pp. 1–33, 2016, doi: 10.1063/1.4944633.

[84] J. Harris, “Adiabatic-connection approach to Kohn-Sham theory,” *Phys. Rev. A*, vol. 29, no. 4, pp. 1648–1659, 1984, doi: 10.1103/PhysRevA.29.1648.

[85] C. Adamo and V. Barone, “Toward reliable density functional methods without adjustable parameters: The PBE0 model,” *J. Chem. Phys.*, vol. 110, no. 13, pp. 6158–6170, 1999, doi: 10.1063/1.478522.

[86] J. Heyd and G. E. Scuseria, “Influence of the exchange screening parameter on the performance of screened hybrid functionals,” *J. Chem. Phys.*, vol. 125, no. 22, p. 224106, 2006, doi: 10.1063/1.2404663.

[87] V. I. Anisimov, J. Zaanen, and O. K. Andersen, “Band theory and Mott insulators: Hubbard U instead of Stoner I,” *Phys. Rev. B*, vol. 44, no. 3, pp. 943–954, 1991, doi: 10.1103/PhysRevB.44.943.

[88] S. Dudarev and G. Botton, “Electron-energy-loss spectra and the structural stability of nickel oxide: An LSDA+U study,” *Phys. Rev. B - Condens. Matter Mater. Phys.*, vol. 57, no. 3, pp. 1505–1509, 1998, doi: 10.1103/PhysRevB.57.1505.

[89] O. Gunnarsson, O. K. Andersen, O. Jepsen, and J. Zaanen, “Density-functional calculation of the parameters in the Anderson model: Application to Mn in CdTe,” *Phys. Rev. B*, vol. 39, no. 3, pp. 1708–1722, 1989, doi: 10.1103/PhysRevB.39.1708.

[90] S. Grimme, “Density functional theory with London dispersion corrections,” *Wiley Interdiscip. Rev. Comput. Mol. Sci.*, vol. 1, no. 2, pp. 211–228, 2011, doi: 10.1002/wcms.30.

[91] S. Grimme, “Semiempirical GGA-Type Density Functional Constructedwith a Long-Range Dispersion Correction,” *J. Comput. Chem.*, vol. 27, pp. 1187–1799, 2006, doi: 10.1002/jcc.

[92] S. Grimme, J. Antony, S. Ehrlich, and H. Krieg, “A consistent and accurate ab initio parametrization of density functional dispersion correction (DFT-D) for the 94 elements H-Pu,” *J. Chem. Phys.*, vol. 132, no. 15, p. 154104, 2010, doi: 10.1063/1.3382344.

[93] G. Kresse and J. Hafner, “Ab initio molecular-dynamics simulation of the liquid-metalamorphous- semiconductor transition in germanium,” *Phys. Rev. B*, vol. 49, no. 20, pp. 14251–14269, 1994, doi: 10.1103/PhysRevB.49.14251.

[94] G. Kresse and J. Hafner, “Ab initio molecular dynamics for liquid metals,” *Phys. Rev. B*, vol. 47, no. 1, pp. 558–561, 1993, doi: 10.1103/PhysRevB.47.558.

[95] G. Kresse and J. Furthmüller, “Efficiency of ab-initio total energy calculations for metals and semiconductors using a plane-wave basis set,” *Comput. Mater. Sci.*, vol. 6, no. 1, pp. 15–50, 1996, doi: 10.1016/0927-0256(96)00008-0.

[96] G. Kresse and J. Furthmüller, “Efficient iterative schemes for ab initio total-

energy calculations using a plane-wave basis set," *Phys. Rev. B*, vol. 54, pp. 11169–11186, 1996, doi: 10.1021/acs.jpca.0c01375.

[97] D. Kresse and D. Joubert, "From ultrasoft pseudopotentials to the projector augmented-wave method," *Phys. Rev. B*, vol. 59, no. 3, pp. 1758–1775, 1999, doi: 10.1103/PhysRevB.59.1758.

[98] P. E. Blöchl, "Projector augmented-wave method," *Physical Review B*, vol. 50, no. 24. pp. 17953–17979, 1994.

[99] D. D. Johnson, "Modified Broyden's method for accelerating convergence in self-consistent calculations," *Phys. Rev. B*, vol. 38, pp. 12807–12813, 1988.

[100] M. P. Teter, M. C. Payne, and D. C. Allan, "Solution of Schrödingers equation for large systems," *Phys. Rev. B*, vol. 40, no. 18, pp. 12255–12263, 1989, doi: 10.1103/PhysRevB.40.12255.

[101] D. M. Bylander, L. Kleinman, and S. Lee, "Self-consistent calculations of the energy bands and bonding properties of B12C3," *Phys. Rev. B*, vol. 42, no. 2, pp. 1394–1403, 1990, doi: 10.1103/PhysRevB.42.1394.

[102] Hendrik J. Monkhorst and J. D. Pack, "Special points for Brillonin-zone integrations," *Phys. Rev. B*, vol. 13, pp. 5188–5192, 1976, doi: 10.1039/c8ta11250a.

[103] J. D. Pack and H. J. Monkhorst, "Special points for Brillonln-zone integrations"—a reply," *Phys. Rev.*, vol. 16, no. 4, pp. 1748–1749, 1977.

[104] B. J. Morgan and G. W. Watson, "A DFT + U description of oxygen vacancies

at the TiO2 rutile (1 1 0) surface," *Surf. Sci.*, vol. 601, no. 21, pp. 5034–5041, 2007, doi: 10.1016/j.susc.2007.08.025.

[105] B. J. Morgan and G. W. Watson, "A density functional theory + u study of Oxygen vacancy formation at the (110), (100), (101), and (001) surfaces of rutile TiO2," *J. Phys. Chem. C*, vol. 113, no. 17, pp. 7322–7328, 2009, doi: 10.1021/jp811288n.

[106] B. J. Morgan and G. W. Watson, "Intrinsic n-type defect formation in TiO 2: A comparison of rutile and anatase from GGA+ U calculations," *J. Phys. Chem. C*, vol. 114, pp. 2321–2328, 2010, doi: 10.1021/jp301913c.

[107] D. C. Cronemeyer, "Electrical and optical properties of rutile single crystals," *Phys. Rev.*, vol. 87, no. 5, pp. 876–886, 1952, doi: 10.1103/PhysRev.87.876.

[108] R. K. Singha, Y. Tsuji, M. H. Mahyuddin, and K. Yoshizawa, "Methane Activation at the Metal-Support Interface of Ni4-CeO2(111) Catalyst: A Theoretical Study," *J. Phys. Chem. C*, vol. 123, no. 15, pp. 9788–9798, 2019, doi: 10.1021/acs.jpcc.8b11973.

[109] Y. Jiang, J. B. Adams, and M. Van Schilfgaarde, "Density-functional calculation of CeO 2 surfaces and prediction of effects of oxygen partial pressure and temperature on stabilities," *J. Chem. Phys.*, vol. 123, no. 6, p. 064701, 2005, doi: 10.1063/1.1949189.

[110] C. E. Calderon *et al.*, "The AFLOW standard for high-throughput materials science calculations," *Comput. Mater. Sci.*, vol. 108, pp. 233–238, 2015, doi: 10.1016/j.commatsci.2015.07.019.

[111] D. Channei *et al.*, "Photocatalytic degradation of methyl orange by CeO2 and Fe-doped CeO2 films under visible light irradiation," *Sci. Rep.*, vol. 4, pp. 1–7, 2014, doi: 10.1038/srep05757.

[112] Y. Ma *et al.*, "Interface engineering in CeO2 (1 1 1) facets decorated with CdSe quantum dots for photocatalytic hydrogen evolution," *J. Colloid Interface Sci.*, vol. 579, pp. 707–713, 2020, doi: 10.1016/j.jcis.2020.06.100.

[113] J. C. Phillips, "Energy-band interpolation scheme based on a pseudopotential," *Phys. Rev.*, vol. 112, no. 3, pp. 685–695, 1958, doi: 10.1103/PhysRev.112.685.

[114] M. T. Yin and M. L. Cohen, "Theory of ab initio pseudopotential calculations," *Phys. Rev. B*, vol. 25, no. 12, pp. 7403–7412, 1982, doi: 10.1103/PhysRevB.25.7403.

[115] D. M. Bylander and L. Kleinman, "Efficacious Form for Model Pseudopotentials," *Phys. Rev. Lett.*, vol. 48, no. 20, pp. 1425–1428, 1982, [Online]. Available: http://journals.aps.org/prl/abstract/10.1103/PhysRevLett.48.1425.

[116] D. Vanderbilt, "Soft self-consistent pseudopotentials in a generalized eigenvalue formalism," *Phys. Reivew B*, vol. 41, no. 11, p. 7892, 1990, doi: 10.1016/S0016-5085(77)80340-5.

[117] R. D. King-Smith and D. Vanderbilt, "Theory of polarization of crystalline solids," *Phys. Rev. B*, vol. 47, no. 3, pp. 1651–1654, 1993, doi: 10.1103/PhysRevB.47.1651.

[118] M. C. Payne, M. P. Teter, D. C. Allan, T. A. Arias, and J. D. Joannopoulos, "Iterative minimization techniques for ab initio total-energy calculations: Molecular dynamics and conjugate gradients," *Rev. Mod. Phys.*, vol. 64, no. 4, pp. 1045–1097, 1992, doi: 10.1103/RevModPhys.64.1045.

[119] E. Wimmer, A. J. Freeman, and M. Weinert, "Cesiation of W(001): Work Function Lowering by Multiple Dipole Formation," *Phys. Rev. Lett.*, vol. 48, no. 16, pp. 1128–1131, 1982.

[120] J. H. Scofield, "Theoretical Photoionization Cross Sections From 1 To 1500 keV," *Lawrence Livermore Lab.*, pp. 5–6, 1973.

[121] J. Yeh and I. Lindau, "Atomic subshell photoionization cross sections and asymmetry parameters: $1 \leqslant Z \leqslant 103$," *At. Data Nucl. Data Tables*, vol. 32, no. 1, pp. 1–155, 1985.

[122] C. N. Savory, A. M. Ganose, W. Travis, R. S. Atri, R. G. Palgrave, and D. O. Scanlon, "An assessment of silver copper sulfides for photovoltaic applications: Theoretical and experimental insights," *J. Mater. Chem. A*, vol. 4, no. 32, pp. 12648–12657, 2016, doi: 10.1039/c6ta03376h.

[123] C. Körber *et al.*, "Electronic structure of In2 O3 and Sn-doped In 2 O3 by hard x-ray photoemission spectroscopy," *Phys. Rev. B*, vol. 81, no. 16, pp. 1–9, 2010, doi: 10.1103/PhysRevB.81.165207.

[124] B. A. D. Williamson, J. Buckeridge, J. Brown, S. Ansbro, R. G. Palgrave, and D. O. Scanlon, "Engineering Valence Band Dispersion for High Mobility p-Type Semiconductors," *Chem. Mater.*, vol. 29, no. 6, pp. 2402–2413, 2017, doi:

10.1021/acs.chemmater.6b03306.

[125] D. S. Bhachu *et al.*, "Bismuth oxyhalides: Synthesis, structure and photoelectrochemical activity," *Chem. Sci.*, vol. 7, no. 8, pp. 4832–4841, 2016, doi: 10.1039/c6sc00389c.

[126] S. Sathasivam *et al.*, "Computational and experimental study of Ta2O5 thin films," *J. Phys. Chem. C*, vol. 121, no. 1, pp. 202–210, 2017, doi: 10.1021/acs.jpcc.6b11073.

[127] S. Sathasivam *et al.*, "Single Step Solution Processed GaAs Thin Films from GaMe3 and tBuAsH2 under Ambient Pressure," *J. Phys. Chem. C*, vol. 120, no. 13, pp. 7013–7019, 2016, doi: 10.1021/acs.jpcc.6b00850.

[128] R. F. W. Bader, "A Quantum Theory of Molecular Structure and Its Applications," *Chem. Rev.*, vol. 91, no. 5, pp. 893–928, 1991, doi: 10.1021/cr00005a013.

[129] R. F. W. Bader, "Atoms in Molecules," *Acc. Chem. Res.*, vol. 18, no. 1, pp. 9–15, 1985, doi: 10.1021/ar00109a003.

[130] G. Henkelman, A. Arnaldsson, and H. Jónsson, "A fast and robust algorithm for Bader decomposition of charge density," *Comput. Mater. Sci.*, vol. 36, no. 3, pp. 354–360, 2006, doi: 10.1016/j.commatsci.2005.04.010.

[131] E. Sanville, S. D. Kenny, R. Smith, and G. Henkelman, "Improved Grid-Based Algorithm forBader Charge Allocation," *J. Comput. Chem.*, vol. 28, pp. 899–908, 2007, doi: 10.1002/jcc.

[132] W. Tang, E. Sanville, and G. Henkelman, "A grid-based Bader analysis algorithm without lattice bias," *J. Phys. Condens. Matter*, vol. 21, no. 8, pp. 1–7, 2009, doi: 10.1088/0953-8984/21/8/084204.

[133] J. P. Perdew, M. Ernzerhof, and K. Burke, "Rationale for mixing exact exchange with density functional approximations," *J. Chem. Phys.*, vol. 105, no. 22, pp. 9982–9985, 1996, doi: 10.1063/1.472933.

[134] K. Kim and K. D. Jordan, "Comparison of density functional and MP2 calculations on the water monomer and dimer," *J. Phys. Chem.*, vol. 98, no. 40, pp. 10089–10094, 1994, doi: 10.1021/j100091a024.

[135] J. Heyd, G. E. Scuseria, and M. Ernzerhof, "Hybrid functionals based on a screened Coulomb potential," *J. Chem. Phys.*, vol. 118, no. 18, pp. 8207–8215, 2003, doi: 10.1063/1.1564060.

[136] K. Momma and F. Izumi, "VESTA 3 for three-dimensional visualization of crystal, volumetric and morphology data," *J. Appl. Crystallogr.*, vol. 44, no. 6, pp. 1272–1276, 2011, doi: 10.1107/S0021889811038970.

[137] M. H. Beale, M. T. Hagan, and H. B. Demuth, *Neural Network Toolbox ™ 7 User ' s Guide*. 2010.

[138] B. Rusinque, S. Escobedo Salas, and H. de Lasa, "Photoreduction of a Pd-doped mesoporous TiO2 photocatalyst for hydrogen production under visible light," *Catalysts*, vol. 10, no. 1, 2020, doi: 10.3390/catal10010074.

[139] J. Yu, L. Qi, and M. Jaroniec, "Hydrogen production by photocatalytic water splitting over Pt/TiO 2 nanosheets with exposed (001) facets," *J. Phys. Chem.*

C, vol. 114, no. 30, pp. 13118–13125, 2010, doi: 10.1021/jp104488b.

[140] D. Gogoi, A. Namdeo, A. K. Golder, and N. R. Peela, "Ag-doped TiO2 photocatalysts with effective charge transfer for highly efficient hydrogen production through water splitting," *Int. J. Hydrogen Energy*, vol. 45, no. 4, pp. 2729–2744, 2020, doi: 10.1016/j.ijhydene.2019.11.127.

[141] Y. Ren *et al.*, "Effects of 4d transition metals doping on the photocatalytic activities of anatase TiO2 (101) surface," *Int. J. Quantum Chem.*, vol. 121, no. 16, pp. 1–10, 2021, doi: 10.1002/qua.26683.

[142] P. López-Caballero, S. Miret-Artés, A. O. Mitrushchenkov, and M. P. De Lara-Castells, "Ag5-induced stabilization of multiple surface polarons on perfect and reduced TiO2rutile (110)," *J. Chem. Phys.*, vol. 153, no. 16, 2020, doi: 10.1063/5.0029099.

[143] Q. Wu, S. Hou, D. Buceta, H. J. L. Ordoñez, M. Arturo López-Quintela, and C. J. Lambert, "Tuning the surface states of TiO2 using Cu5 atomic clusters," *Appl. Surf. Sci.*, vol. 594, p. 153455, 2022, doi: 10.1016/j.apsusc.2022.153455.

[144] J. H. Stenlid, A. J. Johansson, and T. Brinck, "Searching for the thermodynamic limit-a DFT study of the step-wise water oxidation of the bipyramidal Cu7 cluster," *Phys. Chem. Chem. Phys.*, vol. 16, no. 6, pp. 2452–2464, 2014, doi: 10.1039/c3cp53865f.

[145] Y. Tezuka, S. Shin, T. Ishii, T. Ejima, S. Suzuki, and S. Sato, "Photoemission and Bremsstrahlung Isochromat Spectroscopy Studies of Ti02 (Rutile) and SrTi03," *Journal of the Physical Society of Japan*, vol. 63, no. 1. pp. 347–357,

1994, doi: 10.1143/JPSJ.63.347.

[146] A. Janotti, J. B. Varley, P. Rinke, N. Umezawa, G. Kresse, and C. G. Van De Walle, “Hybrid functional studies of the oxygen vacancy in TiO2,” *Phys. Rev. B - Condens. Matter Mater. Phys.*, vol. 81, no. 8, p. 085212, 2010, doi: 10.1103/PhysRevB.81.085212.

[147] L. Kavan, M. Grätzel, S. E. Gilbert, C. Klemenz, and H. J. Scheel, “Electrochemical and photoelectrochemical investigation of single-crystal anatase,” *J. Am. Chem. Soc.*, vol. 118, no. 28, pp. 6716–6723, 1996, doi: 10.1021/ja954172l.

[148] H. Tang, F. Lévy, H. Berger, and P. E. Schmid, “Urbach tail of anatase TiO2,” *Phys. Rev. B*, vol. 52, no. 11, pp. 7771–7774, 1995, doi: 10.1103/PhysRevB.52.7771.

[149] H. Cheng and A. Selloni, “Energetics and diffusion of intrinsic surface and subsurface defects on anatase TiO2 (101),” *J. Chem. Phys.*, vol. 131, no. 5, p. 054703, 2009, doi: 10.1063/1.3194301.

[150] Y. He, O. Dulub, H. Cheng, A. Selloni, and U. Diebold, “Evidence for the predominance of subsurface defects on reduced anatase TiO2(101),” *Phys. Rev. Lett.*, vol. 102, no. 10, p. 106105, 2009, doi: 10.1103/PhysRevLett.102.106105.

[151] J. Oviedo, M. A. S. Miguel, and J. F. Sanz, “Oxygen vacancies on TiO2 (110) from first principles calculations,” *J. Chem. Phys.*, vol. 121, no. 15, pp. 7427–7433, 2004, doi: 10.1063/1.1796253.

[152] T. Pabisiak and A. Kiejna, “Energetics of oxygen vacancies at rutile TiO2(110) surface,” *Solid State Commun.*, vol. 144, no. 7–8, pp. 324–328, 2007, doi: 10.1016/j.ssc.2007.08.043.

[153] M. A. Henderson, W. S. Epling, C. H. F. Peden, and C. L. Perkins, “Insights into photoexcited electron scavenging processes on TiO2 obtained from studies of the reaction of O2 with OH groups adsorbed at electronic defects on TiO2(110),” *J. Phys. Chem. B*, vol. 107, no. 2, pp. 534–545, 2003, doi: 10.1021/jp0262113.

[154] A. B. Schvval, A. Juan, and G. F. Cabeza, “Theoretical study of the role of the interface of Ag4 nanoclusters deposited on TiO2(110) and TiO2(101),” *Appl. Surf. Sci.*, vol. 490, no. February, pp. 343–351, 2019, doi: 10.1016/j.apsusc.2019.05.291.

[155] M. P. de Lara-Castells, “First-principles modelling of the new generation of subnanometric metal clusters: Recent case studies,” *J. Colloid Interface Sci.*, vol. 612, pp. 737–759, 2022, doi: 10.1016/j.jcis.2021.12.186.

[156] M. Pilar de Lara-Castells *et al.*, “Increasing the optical response of TiO2 and extending it into the visible region through surface activation with highly stable Cu5 clusters,” *J. Mater. Chem. A*, vol. 7, no. 13, pp. 7489–7500, 2019, doi: 10.1039/c9ta00994a.

[157] E. C. Tyo and S. Vajda, “Catalysis by clusters with precise numbers of atoms,” *Nat. Nanotechnol.*, vol. 10, no. 7, pp. 577–588, 2015, doi: 10.1038/NNANO.2015.140.

[158] C. Di Valentin, G. Pacchioni, and A. Selloni, “Electronic structure of defect states in hydroxylated and reduced rutile TiO2(110) surfaces,” *Phys. Rev. Lett.*, vol. 97, no. 16, p. 166803, 2006, doi: 10.1103/PhysRevLett.97.166803.

[159] L. Liu and Y. Li, “Understanding the reaction mechanism of photocatalytic reduction of CO2 with H2O on TiO2-based photocatalysts: A review,” *Aerosol Air Qual. Res.*, vol. 14, no. 2, pp. 453–469, 2014, doi: 10.4209/aaqr.2013.06.0186.

[160] A. Bruix, K. M. Neyman, and F. Illas, “Adsorption, oxidation state, and diffusion of Pt atoms on the CeO 2(111) surface,” *J. Phys. Chem. C*, vol. 114, no. 33, pp. 14202–14207, 2010, doi: 10.1021/jp104490k.

[161] Z. Y, T. B, Y. Z, Z. Y, and L. M, “ARTICLE pubs.acs.org/JPCC Density Functional Theory Study of Sn Adsorption on the CeO2 Surface,” *Phys. Chem.*, vol. 115, no. 33, pp. 16461–16466, 2011, doi: 10.1016/j.cplett.2004.10.079.

[162] M. Baron, O. Bondarehuk, D. Stacchiola, S. Shaikhutdinov, and H. J. Freund, “Interaction of gold with cerium oxide supports: CeO2(111) thin films vs CeOx nanoparticles,” *J. Phys. Chem. C*, vol. 113, no. 15, pp. 6042–6049, 2009, doi: 10.1021/jp9001753.

[163] N. J. Castellani, M. M. Branda, K. M. Neyman, and F. Illas, “Density functional theory study of the adsorption of au atom on cerium oxide: Effect of low-coordinated surface sites,” *J. Phys. Chem. C*, vol. 113, no. 12, pp. 4948–4954, 2009, doi: 10.1021/jp8094352.

[164] M. M. Branda, N. C. Hernández, J. F. Sanz, and F. Illas, “Density functional

theory study of the interaction of Cu, Ag, and Au atoms with the regular CeO2 (111) surface," *J. Phys. Chem. C*, vol. 114, no. 4, pp. 1934–1941, 2010, doi: 10.1021/jp910782r.

[165] P. Luches, F. Pagliuca, S. Valeri, F. Illas, G. Preda, and G. Pacchioni, "Nature of Ag islands and nanoparticles on the CeO 2(111) surface," *J. Phys. Chem. C*, vol. 116, no. 1, pp. 1122–1132, 2012, doi: 10.1021/jp210241c.

[166] G. Preda and G. Pacchioni, "Formation of oxygen active species in Ag-modified CeO2 catalyst for soot oxidation: A DFT study," *Catal. Today*, vol. 177, no. 1, pp. 31–38, 2011, doi: 10.1016/j.cattod.2011.04.036.

[167] J. A. Farmer, J. H. Baricuatro, and C. T. Campbell, "Ag adsorption on reduced CeO2(111) thin films," *J. Phys. Chem. C*, vol. 114, no. 40, pp. 17166–17172, 2010, doi: 10.1021/jp104593y.

[168] K. Saravanakumar, M. M. Ramjan, P. Suresh, and V. Muthuraj, "Fabrication of highly efficient visible light driven Ag/CeO2 photocatalyst for degradation of organic pollutants," *J. Alloys Compd.*, vol. 664, pp. 149–160, 2016, doi: 10.1016/j.jallcom.2015.12.245.

[169] D. Kong *et al.*, "Growth, structure, and stability of Ag on CeO2(111): Synchrotron radiation photoemission studies," *J. Phys. Chem. C*, vol. 115, no. 14, pp. 6715–6725, 2011, doi: 10.1021/jp112392y.

[170] P. Tereshchuk, R. L. H. Freire, C. G. Ungureanu, Y. Seminovski, A. Kiejna, and J. L. F. Da Silva, "The role of charge transfer in the oxidation state change of Ce atoms in the TM13-CeO2(111) systems (TM = Pd, Ag, Pt, Au): A DFT + U

investigation," *Phys. Chem. Chem. Phys.*, vol. 17, no. 20, pp. 13520–13530, 2015, doi: 10.1039/c4cp06016d.

[171] M. J. Piotrowski, P. Tereshchuk, and J. L. F. Da Silva, "Theoretical investigation of small transition-metal clusters supported on the CeO2(111) surface," *J. Phys. Chem. C*, vol. 118, no. 37, pp. 21438–21446, 2014, doi: 10.1021/jp505216y.

[172] D. R. Mullins and K. Z. Zhang, "Metal-support interactions between Pt and thin film cerium oxide," *Surf. Sci.*, vol. 513, no. 1, pp. 163–173, 2002, doi: 10.1016/S0039-6028(02)01704-1.

[173] V. Matolín *et al.*, "Methanol adsorption and decomposition on Pt/CeO2(111)/Cu(111) thin film model catalyst," *Langmuir*, vol. 26, no. 16, pp. 13333–13341, 2010, doi: 10.1021/la101936b.

[174] M. Škoda *et al.*, "Interaction of Au with CeO2(111): A photoemission study," *J. Chem. Phys.*, vol. 130, no. 3, p. 034703, 2009, doi: 10.1063/1.3046684.

[175] G. Thornton, "CO adsorption on the model catalyst Pd/CeO2-x(111)," *ACS Natl. Meet. B. Abstr.*, vol. 2, no. 111, pp. 14215–14222, 2007.

[176] L. Brugnoli, A. Pedone, M. C. Menziani, C. Adamo, and F. Labat, "O2Activation over Ag-Decorated CeO2(111) and TiO2(110) Surfaces: A Theoretical Comparative Investigation," *J. Phys. Chem. C*, vol. 124, no. 47, pp. 25917–25930, 2020, doi: 10.1021/acs.jpcc.0c09080.

[177] N. Negishi, M. Sugasawa, Y. Miyazaki, Y. Hirami, and S. Koura, "Effect of dissolved silica on photocatalytic water purification with a TiO2 ceramic

catalyst," *Water Res.*, vol. 150, pp. 40–46, 2019, doi: 10.1016/j.watres.2018.11.047.